Bunch Length Measurements Using a Martin-Puplett Interferometer at the VUV-FEL

Diploma Thesis
of
Lars Fröhlich

submitted to the
Department of Physics of the University of Hamburg

prepared at
Deutsches Elektronen-Synchrotron (DESY), Hamburg

DESY-THESIS 2005-011
TESLA-FEL 2005-02

June 2005

Abstract

The linac-driven Vacuum-Ultraviolet Free Electron Laser (VUV-FEL) at DESY, Hamburg produces short pulses of intense soft X-ray radiation. As the high gain FEL process depends strongly on a high peak current of the electron bunches, it is necessary to measure and control the bunch length. For this purpose, coherent synchrotron radiation (CSR) from a bending magnet of the bunch compressor BC2 is analyzed with a Martin-Puplett interferometer.

The measurement process and the reconstruction of the longitudinal charge profile are discussed in detail, including the recovery of phase information by Kramers-Kronig analysis of the form factor. The measured spectra show no significant intensity contribution above a frequency of 2 THz, and the reconstructed bunch shape is found to be independent of the acceleration phase in the accessible range, with a full width at half maximum of about 1 ps. No evidence for the formation of a narrow charge spike with an extent below 400 fs can be established. However, critical factors of the measurement like diffraction losses need further investigation.

Zusammenfassung

Der auf einem Linearbeschleuniger beruhende Vakuum-Ultraviolett-Freie-Elektronen-Laser (VUV-FEL) des DESY, Hamburg, erzeugt kurze Pulse intensiver weicher Röntgenstrahlung. Da der hochverstärkende FEL-Prozess einen großen Spitzenstrom der Elektronenpakete voraussetzt, ist die Messung und Regelung der Elektronenpaketlänge notwendig. Zu diesem Zweck wird die kohärente Synchrotronstrahlung (CSR), die in einem Ablenkmagneten der magnetischen Schikane BC2 entsteht, mit einem Martin-Puplett-Interferometer untersucht.

Der Messprozess und die Rekonstruktion des longitudinalen Ladungsprofils werden detailliert erörtert, einschließlich der Rückgewinnung von Phaseninformationen durch eine Kramers-Kronig-Analyse des Formfaktors. Die gemessenen Spektren weisen keinen signifikanten Intensitätsbeitrag über einer Frequenz von 2 THz auf, und im der Messung zugänglichen Bereich ist die rekonstruierte Form des Elektronenpakets unabhängig von der Beschleunigungsphase, mit einer Halbwertsbreite von etwa 1 ps. Die Bildung einer schmalen Ladungsspitze mit einer Ausdehnung von unter 400 fs kann nicht nachgewiesen werden. Jedoch bedürfen kritische Einflussgrößen der Messung wie etwa Beugungsverluste weiterer Untersuchung.

Lars Fröhlich
Deutsches Elektronen-Synchrotron
Notkestraße 85
22607 Hamburg, Germany
lars.froehlich@desy.de

German title:
Messung der Elektronenpaketlänge am VUV-FEL mit einem Martin-Puplett-Interferometer

Published under DESY report numbers:
DESY-THESIS 2005-011
TESLA-FEL 2005-02

Printed by the DESY copy center.
This document was typeset using LaTeX and KOMA-Script.

Contents

List of Tables

List of Figures

1 Introduction

In this thesis, the results of longitudinal bunch shape and bunch length measurements at the DESY VUV-FEL are discussed. As short electron bunches are required for a high-gain free electron laser, the coherent synchrotron radiation (CSR) they produce in a magnetic chicane can be used for diagnostics. The employment of a Martin-Puplett interferometer for measuring the CSR spectrum and the principle of reconstructing the charge distribution from it are presented.

1.1 From synchrotron radiation to the free electron laser

Synchrotron light from particle accelerators has proven to be a powerful tool in solid state physics and material science due to its high intensity and broad spectrum, ranging from the infrared to hard X-rays. At first merely a by-product of electron accelerators used for elementary particle research, the unique properties of this radiation have attracted a huge community of users and given rise to an ever-growing demand for higher brilliance of the synchrotron light.

In the last decades, more and more accelerator facilities have either been converted to dedicated synchrotron light sources (e.g. the DORIS storage ring at HASYLAB[1]) or have been constructed solely for that purpose (e.g. SLS[2], Diamond[3]). These installations of the so-called second and third generation are storage rings using wigglers and undulators – periodic arrangements of permanent magnets generating an alternating transverse magnetic field – to improve the quality of the generated radiation. However, the electrons in these setups do not radiate in phase, and their energy is limited by the size of the storage ring. An agreement has been reached over the past ten years that the next step towards higher brilliance would be taken with linear accelerators driving *Free Electron Lasers* (FELs), promising to increase radiation power, coherence level, and to yield several orders of magnitude in brilliance as depicted in Fig. 1.1.

Already in 1971, J. M. J. Madey had suggested the "stimulated emission of bremsstrahlung in a periodic magnetic field" [Mad71] as a mechanism to generate high-power coherent radiation in an undulator structure. In 1976, the applicability of his theory was demonstrated at Stanford University when the first FEL amplified light of 10.6 µm wavelength [Eli76]. The setup of a "classical" low-gain FEL resembles that of a conventional laser in using an optical cavity to amplify the light over many reflection cycles. This principle works well in the infrared, visible or "soft" ultraviolet range, but fails for shorter wavelengths, as there are no good mirrors for the "hard" ultraviolet (sometimes called vacuum-ultraviolet) and X-ray radiation needed for diffraction experiments.

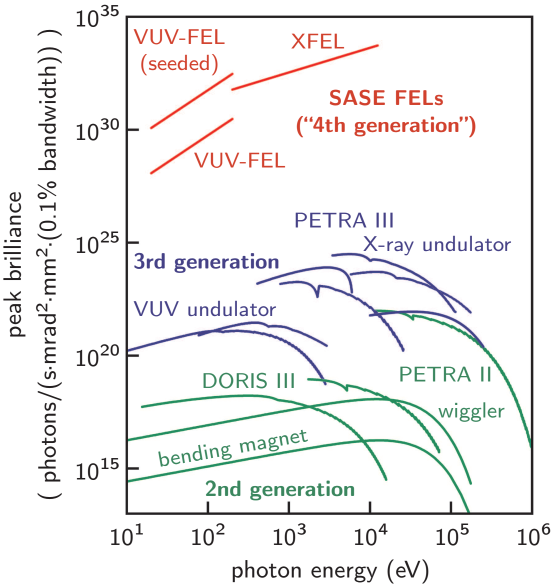

Figure 1.1: Peak brilliance of various X-ray sources. SASE FELs will produce radiation with a brilliance several orders of magnitude higher than that of conventional synchrotron light sources.

The key to free electron lasers in this spectral range is the effect of *Self-Amplified Spontaneous Emission* or SASE. The basic idea is that the random density fluctuations present in any electron beam contain some frequency component that fulfils the resonance condition imposed by an undulator, leading to the development of a longitudinal charge density modulation. If the undulator is long enough, this "microbunching" increases the fraction of electrons radiating in phase, and thus enables a high-gain FEL process. First discussed by A. M. Kondratenko and E. L. Saldin in 1981 [Kon81] and independently derived by R. Bonifacio et al. in 1984 [Bon84], the SASE principle was shown to work in some prototype machines.

In 2000, the Low Energy Undulator Test Line LEUTL at Argonne National Laboratory[4] showed SASE lasing at 530 nm wavelength [Mil00], which could later be improved to 385 nm. It was followed by the *TESLA Test Facility* TTF at DESY in the same year, when the first hard ultraviolet radiation with a peak intensity at 109 nm was produced [And00]. Tunability down to 80 nm was demonstrated few weeks later.

1.2 The VUV-FEL

Conceived not only as a free electron laser, but mainly as a testbed for the proposed superconducting linear collider TESLA (TeV Energy Superconducting Linear Accelerator), the TESLA Test Facility was to produce an electron beam of considerably higher quality in terms of emittance and bunch length than attainable in a storage ring. While work on the superconducting 1.8 K niobium cavities for the accelerator modules started in 1992, construction of the 100 m long linac was to commence about two years later. It comprised a radio frequency (RF) photocathode

---

[1] Hamburger Synchrotronstrahlungslabor, DESY, Hamburg, Germany

[2] Swiss Light Source, Villigen, Switzerland

[3] Diamond Synchrotron Light Source, Rutherford Appleton Laboratory, Didcot, UK

[4] Argonne National Laboratory, Argonne, Illinois, USA

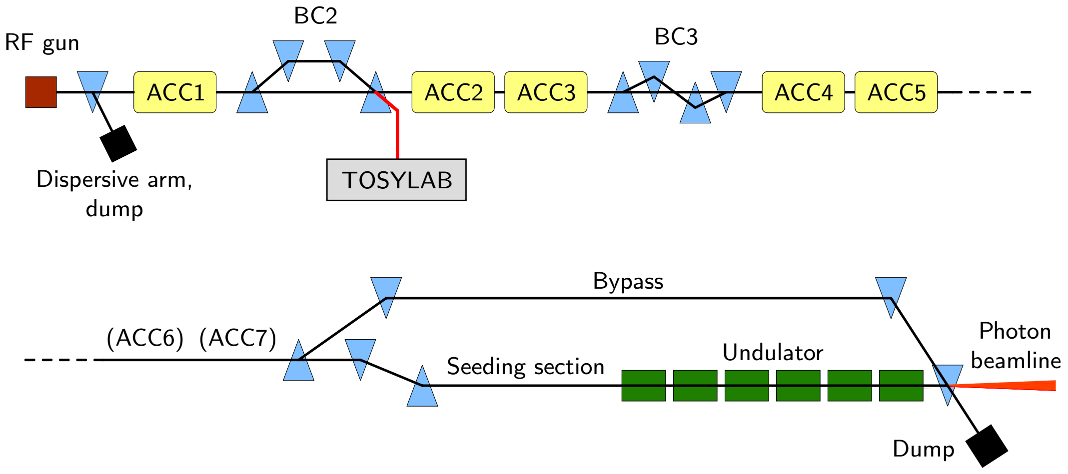

Figure 1.2: Sketch of the VUV-FEL. The electrons are produced in the photocathode RF gun and accelerated in the modules ACC1 to ACC5. Two bunch compressors serve to reduce the bunch length and increase the peak current in order to enable the SASE process in the undulator. At the last dipole of BC2, synchrotron light is extracted and led through a transfer line to the Terahertz and Optical Synchrotron Radiation Laboratory, TOSYLAB.

electron gun, one accelerator module with eight nine-cell cavities fed with an RF frequency of 1.3 GHz, a bunch compressor to reduce the bunch length and a 15 m long undulator. TTF was operated until 2003, when the accelerator was extended to 260 m in order to drive an FEL at much shorter wavelengths.

Commissioning of the second phase of the test facility, named Vacuum-Ultraviolet Free Electron Laser for the expected spectral range it would cover, began in early 2004. As sketched in Fig. 1.2, the VUV-FEL consists of an RF photocathode gun, five accelerator modules similar to the type used in TTF, two bunch compressors – named BC2 and BC3 for historical reasons –, and an undulator composed of six 5 m long segments. Some free space behind the modules ACC4 and ACC5 is reserved for two additional acceleration stages in order to facilitate a later increase in energy.

The RF gun can produce bunches of up to 4 nC charge at a rate of 1 MHz, grouped in bunch trains as required (Fig. 1.3). The electrons are accelerated to an energy of 127 MeV in ACC1 and pass the first bunch compressor, BC2, where the bunch may be shortened by about a factor of eight [Stu04]. This is necessary because the peak current of the beam in the undulator is a decisive factor for the SASE process. ACC2 and ACC3 increase the energy to 380 MeV before another compression step by a factor of up to five can be taken in BC3. In the current state, the last modules are used to push the beam energy to 440 MeV. It is planned to cross the threshold of 1 GeV by using the option for two more acceleration structures, ACC6 and ACC7. In front of the main undulator, space is reserved for additional undulators to "seed" the FEL process. A bypass line allows to send the beam to the dump without traversing the sensitive undulator structures at all.

It was in January 2005, few weeks after the first beam had passed the undulator, when the VUV-FEL produced the world's first soft X-ray SASE laserlight at wavelengths of about 30 nm. In mid-2005, the VUV-FEL is scheduled to become a user facility delivering its laser pulses to five experimental stations. Planned experiments include cluster, surface and solid state physics as well as molecular biology and plasma research. The experimentators are not only going to take advantage of the high intensity of the generated radiation, but especially of its time structure, as the single light pulses are far shorter than a picosecond. This allows novel investigations of the course of chemical processes or of the interaction of matter with X-ray light.

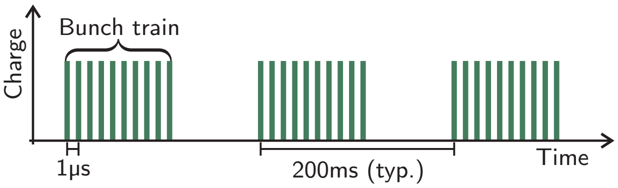

Figure 1.3: Timing of macropulses at the VUV-FEL. The beam is divided into bunch trains of typically 10 single bunches, the latter repeating at 1 MHz. The macropulse repetition rate is usually 5 Hz or 2 Hz. For user operation, up to 7200 bunches/train at 10 Hz are planned, with a bunch repetition rate of 9 MHz.

With these unique features, the VUV-FEL also serves as a pilot machine for the *European X-ray FEL* (XFEL), a 20 GeV linac-driven free electron laser planned to be built in 2006, extending from the DESY site over a length of more than 3 km to the north-west [Wei04].

1.3 Bunch length

As mentioned before, the peak current I_0 of the electron bunches is an important factor for a high-gain FEL. This can be seen directly from the simplified equations for the case of a monoenergetic electron beam with an energy matching the resonance condition imposed by the undulator [Wie03]. In this case, the gain G of the seeding electromagnetic wave grows exponentially with the longitudinal position z in the undulator,

$$G(z) \propto \exp\left(\frac{z}{L_\mathrm{G}}\right) \quad ,$$

with the gain length given by

$$L_\mathrm{G} = C\gamma \left(\frac{\sigma_\mathrm{t}^2}{I_0}\right)^{1/3} \quad .$$

C is merely a constant defined by the parameters of the undulator, γ denotes the relativistic gamma factor and σ_t the transverse RMS size of the beam. It can be seen that it is imperative to have an electron beam with high peak current to render the generation of laser pulses feasible within an undulator of limited length.

To reach a radiation wavelength of 6 nm in the ultimate extension stage of the VUV-FEL, a peak current of 2500 A will be needed (cf. [Edw95], [TTF02]). This emphasizes the need for longitudinal bunch compression, which is realized by magnetic chicanes that are discussed in more detail in section 5.1. It also leads to the requirement for new techniques of longitudinal bunch shape measurement, as conventional methods (like streak cameras) reach their resolution limit for the generated sub-picosecond long bunches. At present, several diagnostic techniques for ultrashort bunches are under investigation; a comprehensive overview can be found in [Kra97]. They may be grouped in two main categories, time-domain and frequency-domain techniques.

The two best-known time domain methods involve the use of special cavities. In the *zero-phasing* technique, the cavity is fed with the usual longitudinally accelerating RF wave after a phase shift of 90°, which means that an energy slope is impressed on the bunch so that its head can be separated from its tail in a dispersive section. Very similar is the employment of a *transverse deflecting cavity*, which uses a transverse mode to make head and tail of a bunch separable on a screen. Both of these methods suffer from the disadvantage of relatively high space requirements and of their invasiveness, which means that some bunches have to be consumed for the measurement. A promising noninvasive time-domain technique is the *Electro-Optical Sampling* (EOS), which uses the dependence of the birefringence of a ZnTe or similar crystal on the strength of an external electric field by putting the crystal near the beam and probing its optical properties with ultrashort laser pulses that are triggered relative to the arrival time of the single bunches. EOS is mainly limited by the timing jitter of the electronics involved; a relative jitter of 40 fs has already been demonstrated [Ste04a].

All frequency domain approaches involve the analysis of the radiation spectrum generated by the electron bunch. In this context, the most important types of radiation are coherent synchrotron radiation (CSR), coherent transition radiation (CTR) and coherent diffraction radiation (CDR). Although more subtle spectrometers have been proposed (see e.g. [Lud03]), the widely used work horse for spectroscopy in all ranges of application is the Michelson interferometer.

The focus of this thesis is on the examination of synchrotron light that is extracted from the last dipole of BC2 and led through a transfer line to the Terahertz and Optical Synchrotron Radiation Laboratory, TOSYLAB (Fig. 1.2). There, the intensity spectrum is measured with a Martin-Puplett interferometer, a variant of the Michelson type especially suited for polarized radiation.

Measurements with a similar instrument have been done at the Tesla Test Facility by Boris Leißner, Marc Geitz and Jan Menzel and can be found in [Lei98], [Gei99a] and [Men05]. Earlier investigations are found in [Han97].

2 Beam diagnostics with coherent radiation

The radiation emitted by a relativistic bunch of electrons is usually incoherent because the particles radiate under random phases. In this case, the intensity perceived by an observer is the sum of the single-particle intensities, regardless of the nature of the radiation process. However, this simple relation is only valid as long as the radiation wavelength is small compared to the bunch length.

If we consider a one-dimensional distribution of electrons that is confined to a length l, we find the phases of emission to be distributed between 0 and 2π for a wavelength $\lambda = l$. For longer wavelengths, the phase range becomes even smaller, and hence the emitted radiation becomes partially coherent. If the wavelength is big compared to the bunch length, $\lambda \gg l$, the phase difference between the electric fields generated by the electrons is negligible, and the total field may be found by adding these single-particle contributions.

As intensity scales with the square of the electric field, we may thus distinguish two extreme cases. For totally incoherent radiation, the intensity scales with the number N of emitting particles, whereas in the totally coherent case it scales with N^2.

2.1 The radiation spectrum of a bunch of charged particles

As the goal is to use the radiation spectrum $I(\omega)$ produced by a bunch of relativistic charged particles to determine its density distribution $\rho(\boldsymbol{x})$, an expression has to be found relating them. The brief mathematical derivation given here is similar to the one found in [Lai96], and its validity is restricted to the far-field or Fraunhofer limit.

Considering a bunch of N particles with the individual coordinates $\boldsymbol{x}_j$, we first postulate that they are all subject to the same radiation process, each emitting an intensity distribution described by the single-particle spectrum $I_1(\omega)$. In the far-field, the difference in field amplitude from the single particles can be neglected. However, their phase contribution has to be considered. Hence, if a detector is put in a direction described by the unit vector $\boldsymbol{n}$ from the charge distribution, it will observe the intensity sum

$$\begin{aligned} I(\omega) &= I_1(\omega) \left| \sum_{j=1}^{N} \exp\left(\mathrm{i}\omega \frac{\boldsymbol{x}_j \cdot \boldsymbol{n}}{c}\right) \right|^2 \\ &= I_1(\omega) \sum_{j=1}^{N} \exp\left(\mathrm{i}\omega \frac{\boldsymbol{x}_j \cdot \boldsymbol{n}}{c}\right) \sum_{k=1}^{N} \exp\left(-\mathrm{i}\omega \frac{\boldsymbol{x}_k \cdot \boldsymbol{n}}{c}\right) \ . \end{aligned}$$

This double sum yields unity for each term with $j = k$ and may thus be written as

$$I(\omega) = I_1(\omega) \left(N + \sum_{j \neq k}^{N} \exp\left(\mathrm{i}\omega \frac{(\boldsymbol{x}_j - \boldsymbol{x}_k) \cdot \boldsymbol{n}}{c}\right) \right) \ . \qquad (2.1)$$

To proceed from discrete particles to a continuous distribution, the total charge of the bunch is expressed as $Q = \int \rho(\boldsymbol{x})\, \mathrm{d}^3x$. Then the number of electrons in the infinitesimal cube between $\boldsymbol{x}$ and $\boldsymbol{x} + \mathrm{d}\boldsymbol{x}$ is $\mathrm{d}N = (\rho(\boldsymbol{x})/Q)\, \mathrm{d}^3x$, and (2.1) can be rewritten as

$$\begin{aligned} I(\omega) = I_1(\omega) \Big(N + N(N-1) \iint & \frac{\rho(\boldsymbol{x})\rho(\boldsymbol{x}')}{Q^2} \\ & \cdot \exp\left(\mathrm{i}\omega \frac{(\boldsymbol{x} - \boldsymbol{x}') \cdot \boldsymbol{n}}{c}\right) \mathrm{d}^3x\, \mathrm{d}^3x' \Big) \ . \end{aligned} \qquad (2.2)$$

If we now introduce the *form factor* $F(\omega)$ as the three-dimensional Fourier transform[1] of the charge distribution with

$$F(\omega) = \frac{1}{Q} \int \mathrm{d}^3x\, \rho(\boldsymbol{x}) \exp(-\mathrm{i}\omega(\boldsymbol{x} \cdot \boldsymbol{n})) \ , \qquad (2.3)$$

we obtain the simple relation

$$I(\omega) = I_1(\omega) \left(N + N(N-1) \left| F(\omega) \right|^2 \right) \ . \qquad (2.4)$$

This result is consistent with the qualitative considerations outlined above. For sufficiently high frequencies, the form factor vanishes and $I(\omega) = N I_1(\omega)$. In the low-frequency limit of $\omega \to 0$, $F(\omega)$ approaches unity and hence $I(\omega) = N^2 I_1(\omega)$.

It should be noted that the form factor depends on the direction $\boldsymbol{n}$ of the particular wave vector. In the case of observation along the direction of motion of the bunch, (2.3) reduces to a one-dimensional integration over the longitudinal charge distribution,

$$F_z(\omega) = \frac{1}{Q} \int \mathrm{d}z\, \rho(z) \exp(-\mathrm{i}\omega z) \ .$$

If the radiated power is confined to a small solid angle around this z-axis, even experimental setups with a broad angular acceptance will measure a spectrum that is dominated by the longitudinal form factor. It will be seen that this is the case for synchrotron radiation.

Provided that the single-particle spectrum is known, equation (2.4) is a useful tool to calculate the coherent spectrum of an electron bunch from its density distribution. Still, the reverse way – calculating the distribution from the spectrum – cannot be taken without difficulties. The problem is that only the modulus of the form factor appears in the equation, while the Fourier transform of any asymmetrical distribution has a non-vanishing imaginary part. The interferometry with CSR and a Martin-Puplett interferometer as described in this thesis shares this drawback with all frequency-domain techniques of bunch length diagnostics that rely on a measurement of the intensity spectrum alone. However, the phase of the form factor is not completely independent of its absolute distribution, and thus a *minimal phase* carrying most characteristics of the original bunch shape can be established using a *Kramers-Kronig relation*. The problem of recovering the lost phase information of the form factor is addressed in detail in chapter 4.

As mentioned before, in the context of beam diagnostics a number of different sources of coherent radiation are under investigation. Here, only synchrotron and transition radiation will be characterized briefly.

---

[1] Accelerator physicists sometimes define the form factor as the square of the Fourier transform (2.3). However, the term is most widely used in nuclear physics, and hence the convention used in the majority of textbooks from that field is followed here.

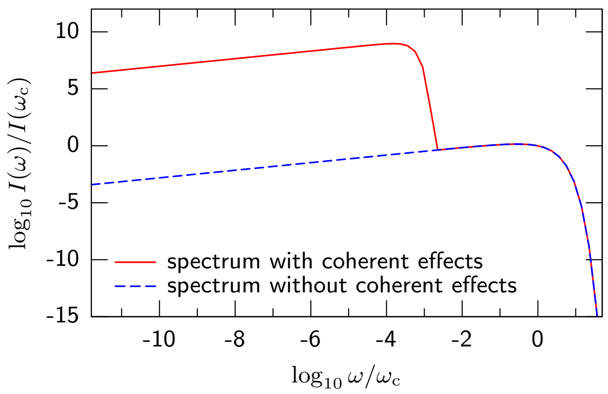

Figure 2.1: Spectrum of synchrotron radiation with coherence effects. The axes are normalized to the critical angular frequency ω_c and the synchrotron radiation intensity at that frequency. The coherent amplification is shown for a Gaussian-shaped bunch with an RMS width of 250 µm and a charge of 1 nC.

2.2 Coherent synchrotron radiation

Synchrotron radiation is produced when a relativistic charged particle is accelerated perpendicular to its direction of motion. For purely circular motion, analytical formulas describing the radiated spectrum can be found in a variety of references like [Jac98]. The total radiated power is known to scale as E^4/R^2 with E being the beam energy and R the bending radius, and at the at the critical angular frequency $\omega_c = 2\pi\nu_c = \frac{3}{2}\gamma^3\frac{c}{R}$ the spectrum is split in two halves with the same integrated power.

From the discussion above it is clear that coherence effects can only be expected for wavelengths in the order of or longer than the bunchlength, i.e. for the low-frequency part of the spectrum. Figure 2.1 shows the coherent synchrotron radiation spectrum for a Gaussian bunch of 250 µm RMS width. For conditions similar to those in bunch compressor BC2, $\gamma = 250$ and $R = 1.6$ m, the critical frequency is approximately $\nu_c \approx 7\cdot 10^{14}$ Hz, while the coherent amplification takes place below about 4 THz. In the context of bunch length measurements, a low-frequency approximation of the spectral power distribution as given by [Hof98],

$$\begin{aligned}\frac{\mathrm{d}P}{\mathrm{d}\omega} &\approx \frac{e_0^2}{2\pi\epsilon_0\Gamma(\frac{1}{3})}\left(\frac{\omega}{3cR^2}\right)^{1/3}\\ &\approx 1.7224\cdot 10^{-28}\,\mathrm{m}\frac{\mathrm{W}}{\mathrm{s}^{-1}}\cdot\left(\frac{\omega}{3cR^2}\right)^{1/3},\end{aligned} \tag{2.5}$$

can be used as $I_1(\omega)$ in (2.4) to obtain a rough estimate of the form factor.

Considering that the total radiation power scales with E^4, it is remarkable that approximation (2.5) is independent of the beam energy. As Fig. 2.2 illustrates, the incoherent synchrotron radiation spectra for various relativistic gamma factors in fact do not differ for low frequencies. If the energy is raised, only the shifting of the peak towards higher frequencies causes the integrated power to increase. For accelerator diagnostics this means that the power of the coherent radiation does not depend on beam energy, but only on shape, charge and length of the bunch. In terms of total radiated power, the incoherent part may usually be neglected when there is a significant coherent part in the spectrum.

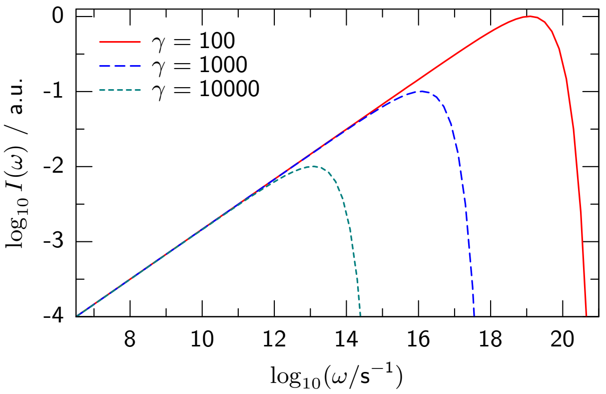

Figure 2.2: Incoherent synchrotron radiation spectra for various beam energies, given in terms of the relativistic gamma factor. For low frequencies, the spectrum is independent of the energy. For higher γ, the intensity distribution extends to higher frequencies and the total radiated power grows.

2.2.1 Angular distribution and polarization

An important characteristic of synchrotron radiation is its angular distribution. With θ denoting the angle of elevation of the observer above the plane of motion of the particles (which will here be called horizontal), [Jac98] gives the following formula for radiated energy per unit solid angle:

$$\frac{\mathrm{d}I}{\mathrm{d}\Omega} = \frac{7}{16}\cdot\frac{e_0^2}{4\pi\epsilon_0 R}\cdot\frac{1}{(1/\gamma^2+\theta^2)^{5/2}}\left[1+\frac{5}{7}\frac{\theta^2}{(1/\gamma^2)+\theta^2}\right]$$

This shows directly that most of the radiation is confined to a small angle of elevation. Moreover, the equation may be used to derive some information about the polarization of the radiation as its first term corresponds to polarization parallel to the orbital plane, and the second to the perpendicular state. The radiation emitted in the plane of motion is totally horizontally polarized. Even integrating over θ, it is found that the parallel component comprises a fraction of $7/8$ of the total emitted power. It will be seen that this property makes synchrotron radiation an ideal input to a Martin-Puplett interferometer.

By a more thorough derivation, an expression incorporating also the frequency dependence may be found. For brevity, only the most important considerations in this context will be mentioned here. A more detailed discussion can be found in a variety of textbooks like [Jac98] or [Wie03]. The average opening angle of synchrotron light is about the inverse of the relativistic gamma factor,

$$\left\langle\theta^2\right\rangle^{1/2} \approx 1/\gamma\ .$$

While for angular frequencies far above ω_c the emitted beam is narrower, it is correspondingly found to be much broader in the limit of long wavelengths; the critical angle where the relative radiated power has decreased to $1/e$ is found to be

$$\theta_c \approx \left(3\frac{c}{\omega R}\right)^{1/3} \qquad (\text{for } \omega \ll \omega_c)\ ,$$

which is again independent of the particle energy. For the conditions found in the magnetic chicane BC2, the average opening angle is 0.23°, whereas for a frequency of 1 THz the critical angle of 2.6° is about ten times bigger.

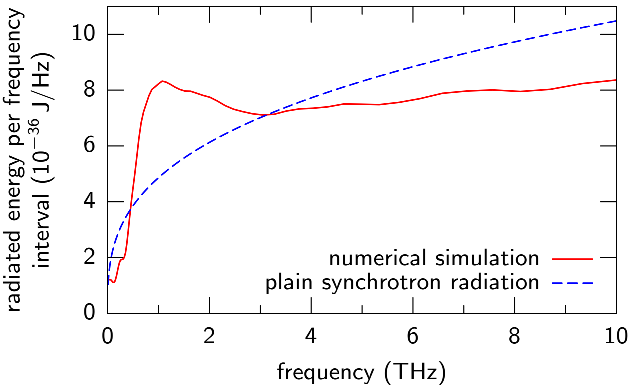

Figure 2.3: Comparison of single-particle spectra for BC2. For the simulation, 5 mirror charges on the vacuum chamber walls were taken into consideration to reproduce the low-frequency cutoff effect. The synchrotron radiation spectrum has been calculated using (2.5), and normalized to the same integrated energy.

2.2.2 Simulated CSR spectrum for bunch compressor BC2

The common analytical formulas for synchrotron radiation describe an electron orbiting in a closed circle in free space. It is obvious that these assumptions are not met by particles moving through a magnetic chicane: On the one hand, the field of a dipole magnet has areas of transition from and to zero. Thus, only a part of the orbit well within the area covered by the dipole can be regarded as the arc of a circle. The radiation contributions from the outer, inhomogeneous field regions are referred to as *edge radiation.* On the other hand, the electrons move within a metallic vacuum chamber, so additional boundary conditions have to be satisfied for a correct calculation of the electric field.

In general, this electrodynamic problem cannot be solved analytically anymore. Instead, numerical simulations are used to track the particle through the bunch compressor while calculating its time dependent electric field. Afterwards a Fourier transform is used to compute the energy spectrum.

The single-particle spectrum shown in Fig. 2.3 is based on a simulation from [Gri05] for a particle energy of 130 MeV and a bending radius of 1.6 m in the last dipole of BC2. The finite length of the magnet is taken into consideration, and the vacuum chamber is modeled as a set of two perfectly conducting horizontal planes, one 4 mm above the plane of motion, the other 4 mm below it. The corresponding boundary conditions are reproduced using the well-known method of mirror charges, of which five generations are calculated. The radiation energy is integrated over the area of the vacuum window of the bunch compressor.

For comparison, the synchrotron radiation spectrum as computed from (2.5) is also shown in Fig. 2.3, normalized to the same integrated energy as the simulated one.

The intensity of the simulated spectrum drops sharply below about 500 GHz. This effect is known from the theory of waveguides which have a cutoff frequency below which no electromagnetic waves are transported. The situation in a vacuum chamber with narrowly spaced metallic walls is similar. It will be seen that the low-frequency cutoff constitutes a severe restriction for bunch shape measurements with coherent radiation.

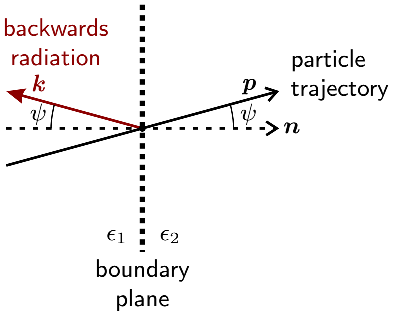

Figure 2.4: Direction of emission of transition radiation. The principal plane of emission is defined by the normal vector $\boldsymbol{n}$ to the boundary plane and the particle momentum $\boldsymbol{p}$. The main part of the backward radiated power is confined to a small angle around vector $\boldsymbol{k}$.

2.3 Coherent transition radiation

Whenever a charged particle passes the boundary between two media with different dielectric properties, a part of the electric field that it carries along is stripped off and emitted as transition radiation (TR). The probably most popular use of this process in accelerator diagnostics is the visualization of the transverse beam profile with optical transition radiation (OTR) screens. These screens are thin discs typically made of silicon, often with a metallic surface layer, which are directly inserted into the vacuum chamber. A conventional camera is then used to observe the generated picture.

While OTR applications are based on incoherent emission, short electron bunches may also generate coherent transition radiation which can be used for coherent radiation diagnostics as described in the beginning of this chapter. Because the focus of this thesis is on interferometry with synchrotron light, the properties of transition radiation will be summarized only roughly. An extended introduction with the focus on beam diagnostics can be found in [Gei99].

An important property of transition radiation is its "white" spectrum. The emitted power is independent of frequency; this is extremely helpful because I_1 in (2.4) is reduced to a constant. The main part of the radiated power is confined to a small angular range in both the forward direction – i.e. in the direction of the beam – and the backward direction as shown in Fig. 2.4. For example, all OTR screens at the VUV-FEL are mounted at an angle of $\psi = 45°$ with respect to the beam axis. The generated transition radiation is then mainly emitted in the plane spanned by that axis and the normal to the screen $\boldsymbol{n}$. Its main direction is 45° off that normal vector, which means that the backward part of the OTR leaves the vacuum chamber by an angle of 90° with respect to the beam axis.

3 The Martin-Puplett interferometer

In this chapter, the principle of spectral measurements with an interferometer of the Martin-Puplett type is discussed. A description of the actual experimental setup is found in section 5.3.

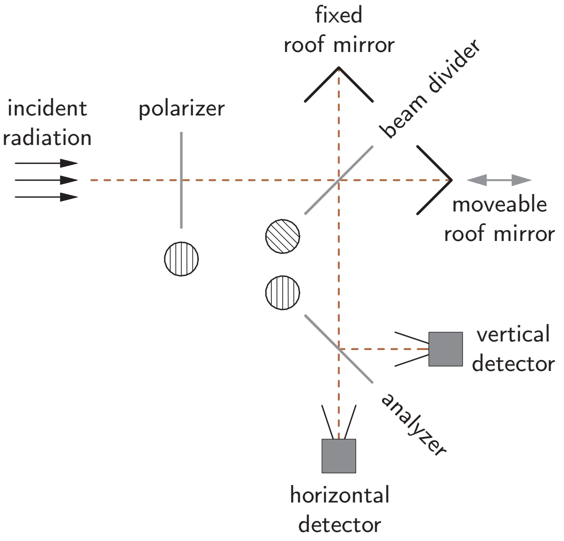

Figure 3.1: Schematic of a Martin-Puplett interferometer. The alignment of the wire grids is outlined as seen in projection by the first incident beam.

3.1 Basic design and mode of operation

The design of a Martin-Puplett interferometer resembles that of the well-known Michelson interferometer, with some additional arrangements to take advantage of the polarizability of electromagnetic radiation. A simplified schematic is given in Fig. 3.1.

The incident light enters from the left and passes a grid of vertically aligned wires acting as a horizontal polarizer for wavelengths in the FIR regime (cf. section 5.3.4). In the center of the interferometer, a similar grid is placed at an angle of 45° relative to the beam axis. Its wires are oriented at 35.3° relative to the horizontal plane, so they appear at 45° in projection (see Fig. A.1 for a drawing of the actual setup). The central grid thus acts as a beam divider that transmits one half of the incoming intensity and reflects the other half, both beams being polarized linearly, but perpendicular to each other. The radiation is then double-reflected at the roof mirrors and reaches the beam splitter again.

Because the polarization of the partial beams is flipped at the roof mirrors (cf. section 5.3.2), the previously reflected beam is now transmitted and vice versa, so that a superposition of both beams propagates into the analyzer arm of the interferometer. Here, the final wire grid separates the horizontally polarized fraction of the radiation from the vertically polarized one, each being monitored by a separate detector.

In the process of recording an interferogram, the right roof mirror is moved along the axis of the incident beam.

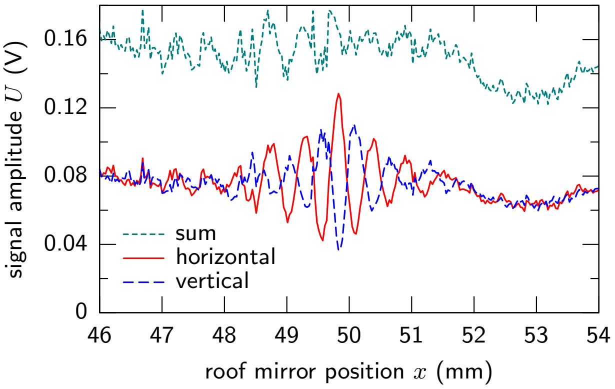

Figure 3.2: Exemplary plot of the detector signal amplitudes versus the position of the moveable roof mirror. Fluctuations and drifts of the total radiation intensity are especially discernible in the sum of the signals.

When the optical path length from the central beam divider to the moveable roof mirror matches that to the fixed one, it is obvious that – after recombination of the two rays – horizontally polarized light arrives at the analyzer grid. In any other case, the difference of the optical path lengths $2x$ gives rise to a phase shift between the reflected and the transmitted ray, and thus leads to a change of the polarization state of the recombined beam.

If two linearly polarized waves with perpendicular polarizations are recombined at non-zero phase, elliptically polarized light is produced. Because the phase depends on the wavelength λ of the radiation as $\varphi = 2\pi\frac{2x}{\lambda}$, different frequency components of the recombined beam show different degrees of ellipticity and therefore different intensities in the horizontal and vertical plane of polarization behind the analyzer grid.

3.2 The interferogram

According to the mode of operation illustrated above, the direct result of an interferometer scan is a series of data points of the two detector signal amplitudes versus the roof mirror position x, as depicted in Fig. 3.2. Fluctuations and drifts in the radiation intensity affect both detector signals similarly, whereas the interference patterns for the horizontal and the vertical polarization are anticorrelated.

The fact that ideally no intensity is lost in the interferometer, i.e. that the intensity of the beam behind the first polarizer equals the total intensity measured at both detectors, can be utilized to decrease the signal fluctuations mentioned above. If $U_\mathrm{h}(x)$ and $U_\mathrm{v}(x)$ are the signal amplitudes measured by the horizontal and vertical detector, we define the *difference interferogram* $\delta(x)$ as the difference of these amplitudes normalized to their sum:

$$\delta(x) = \frac{U_\mathrm{h}(x) - U_\mathrm{v}(x)}{U_\mathrm{h}(x) + U_\mathrm{v}(x)} \tag{3.1}$$

As seen in Fig. 3.3, the noise originating from variations of the beam intensity is almost completely removed in the difference interferogram. Consequently, the curve approaches

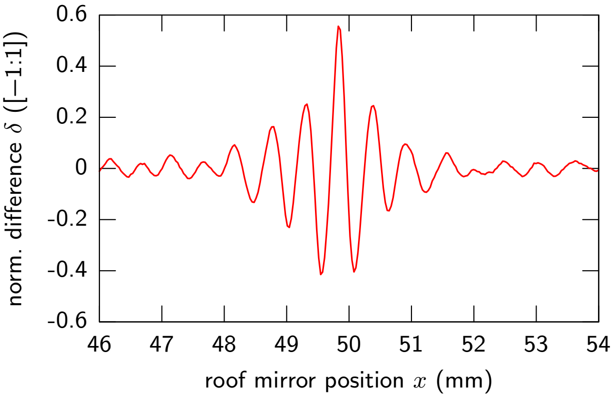

Figure 3.3: Exemplary plot of the normalized difference interferogram corresponding to the signal amplitudes shown above. By normalizing to the sum of the signals, fluctuations are eliminated to a great extent.

zero in the outer regions where less interference effects are noticeable.

3.3 The relation between the difference interferogram and the spectrum

To understand the physical meaning of the difference interferogram, a basic analysis of the functioning of the Martin-Puplett interferometer is necessary, as given for instance in [Lei98]. For this purpose, the electric field $\boldsymbol{E}$ for one frequency component ω of a reference beam is tracked through the various stages of reflection and transmission in the instrument.

Behind the first wire grid, we have a horizontally polarized plane wave with the wave vector $\boldsymbol{k}$:

$$\boldsymbol{E}(t,\boldsymbol{x}) = E(t,\boldsymbol{x})\boldsymbol{u}_\mathrm{h} = E_0 \sin(\omega t - \boldsymbol{k}\boldsymbol{x})\boldsymbol{u}_\mathrm{h}$$

For the analysis of interference effects we will compare the electric fields of partial waves at the same arbitrary location $\boldsymbol{x}$. Hence, $\boldsymbol{k}\boldsymbol{x}$ is just a constant phase offset. We are free to choose it as zero, and thus it is silently neglected in the following.

$\boldsymbol{u}_\mathrm{h}$ designates the horizontal, $\boldsymbol{u}_\mathrm{v}$ the vertical unit vector in a right-handed coordinate system moving along with the beam so that $\boldsymbol{u}_\mathrm{h} \perp \boldsymbol{k} \perp \boldsymbol{u}_\mathrm{v}$. At the beam divider, the wave is split up into a transmitted part $\boldsymbol{E}_\mathrm{t}$ and a reflected part $\boldsymbol{E}_\mathrm{r}$, both being oppositely polarized at 45° relative to the horizontal plane:

$$\boldsymbol{E}_\mathrm{t}(t) = \frac{E_0}{\sqrt{2}} \sin(\omega t) \frac{\boldsymbol{u}_\mathrm{h} + \boldsymbol{u}_\mathrm{v}}{\sqrt{2}}$$
$$\boldsymbol{E}_\mathrm{r}(t) = \frac{E_0}{\sqrt{2}} \sin(\omega t) \frac{\boldsymbol{u}_\mathrm{h} - \boldsymbol{u}_\mathrm{v}}{\sqrt{2}}$$

As outlined in section 5.3.2, the following double-reflection at the roof mirrors preserves the polarization of the beams in our $\boldsymbol{k}$-relative coordinate system. However, a phase shift results if the moveable roof mirror is in a position $\Delta x \neq 0$ where the two beams have unequal optical path lengths. The path difference $2\Delta x$ is equivalent to a time offset $\tau = \frac{2\Delta x}{c}$, and the resulting electric fields are

$$\begin{aligned} \boldsymbol{E}'_\mathrm{t}(t) = \boldsymbol{E}_\mathrm{t}(t-\tau) &= \frac{E_0}{\sqrt{2}} \sin(\omega\,(t-\tau)) \frac{\boldsymbol{u}_\mathrm{h} + \boldsymbol{u}_\mathrm{v}}{\sqrt{2}} \\ \boldsymbol{E}'_\mathrm{r}(t) = \boldsymbol{E}_\mathrm{r}(t) \qquad &= \frac{E_0}{\sqrt{2}} \sin(\omega t) \frac{\boldsymbol{u}_\mathrm{h} - \boldsymbol{u}_\mathrm{v}}{\sqrt{2}} \ . \end{aligned}$$

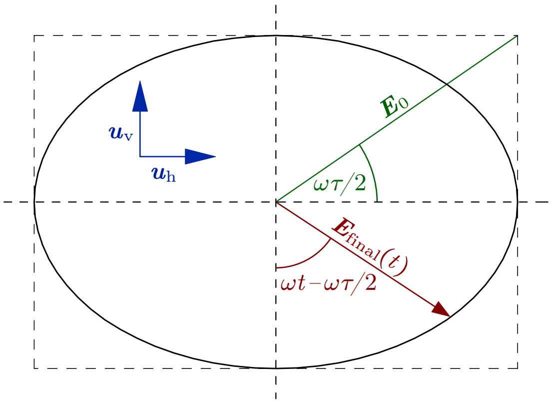

Figure 3.4: Elliptical polarization of light in the analyzer arm of the interferometer

Now, $\boldsymbol{E}'_\mathrm{t}$ is reflected at the central wire grid while $\boldsymbol{E}'_\mathrm{r}$ is transmitted. Hence the total field in front of the analyzer grid becomes

$$\begin{aligned} \boldsymbol{E}_\mathrm{final}(t) &= \boldsymbol{E}'_\mathrm{t}(t) + \boldsymbol{E}'_\mathrm{r}(t) \\ &= \frac{E_0}{2} \Big[\quad (\sin(\omega t - \omega\tau) + \sin\omega t)\,\boldsymbol{u}_\mathrm{h} \\ &\qquad + (\sin(\omega t - \omega\tau) - \sin\omega t)\,\boldsymbol{u}_\mathrm{v} \Big] \ . \end{aligned} \tag{3.2}$$

To get a better view of the polarization state of the radiation, (3.2) can be rewritten using trigonometric sum formulas. This yields

$$\begin{aligned} \boldsymbol{E}_\mathrm{final}(t) = E_0 \Big[& \quad \sin\Big(\omega t - \frac{\omega\tau}{2}\Big) \cos\Big(\frac{\omega\tau}{2}\Big)\,\boldsymbol{u}_\mathrm{h} \\ & - \cos\Big(\omega t - \frac{\omega\tau}{2}\Big) \sin\Big(\frac{\omega\tau}{2}\Big)\,\boldsymbol{u}_\mathrm{v} \Big] \ . \end{aligned} \tag{3.3}$$

From this equation it becomes clear that the horizontal and vertical components are out of phase by 90°, with amplitudes determined by the time shift τ. The light is therefore eliptically polarized as shown in Fig. 3.4. For zero path difference ($\tau = 0$) we get horizontal polarization as expected.

However, the detectors measure intensities and not electric fields, and due to their time constant they integrate over the incoming radiation. Hence we can expect the detector signals to be proportional to the time average of the squared electric field:

$$U_\mathrm{h,v}(\tau) \propto \lim_{T\to\infty} \frac{1}{2T} \int_{-T}^{T} (\boldsymbol{E}_\mathrm{final} \cdot \boldsymbol{u}_\mathrm{h,v})^2 \,\mathrm{d}t$$

After integrating we get

$$U_\mathrm{h}(\tau) \propto \frac{{E_0}^2}{2} \cos^2 \frac{\omega\tau}{2}$$
$$U_\mathrm{v}(\tau) \propto \frac{{E_0}^2}{2} \sin^2 \frac{\omega\tau}{2} \ ,$$

which already shows that the signals have to be *anticorrelated*, i.e. one detector shows a maximum when the other shows a minimum and vice versa. From (3.1), we can now calculate the expected form of the difference interferogram for monochromatic light:

$$\begin{aligned} \delta_\mathrm{mono}(\tau) &= \frac{\cos^2 \frac{\omega\tau}{2} - \sin^2 \frac{\omega\tau}{2}}{\cos^2 \frac{\omega\tau}{2} + \sin^2 \frac{\omega\tau}{2}} \\ &= \cos\omega\tau \end{aligned}$$

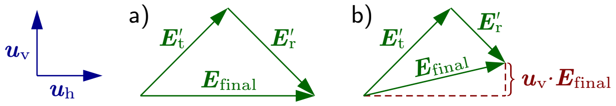

Figure 3.5: Electric field vectors for the recombination of the partial beams in front of the analyzer grid at zero path difference.
a) In a well-aligned interferometer, the amplitudes of the electric fields are equal. The recombined wave is horizontally polarized.
b) If there is some misalignment, the amplitudes differ. The vertical component of the recombined field does not vanish.

It is straightforward to generalize this result to the case of a whole spectrum with an arbitrary intensity distribution $I(\omega)$. In this case, the integrated detector signals are given by

$$U_\text{h}(\tau) \propto \int_0^\infty I(\omega)\cos^2\frac{\omega\tau}{2}\mathrm{d}\omega$$
$$U_\text{v}(\tau) \propto \int_0^\infty I(\omega)\sin^2\frac{\omega\tau}{2}\mathrm{d}\omega\ ,$$

and therefore the difference interferogram becomes

$$\delta(\tau) = \frac{\int_0^\infty I(\omega)\left(\cos^2\frac{\omega\tau}{2}-\sin^2\frac{\omega\tau}{2}\right)\mathrm{d}\omega}{\int_0^\infty I(\omega)\left(\cos^2\frac{\omega\tau}{2}+\sin^2\frac{\omega\tau}{2}\right)\mathrm{d}\omega} = \frac{\int_0^\infty I(\omega)\cos(\omega\tau)\,\mathrm{d}\omega}{\int_0^\infty I(\omega)\,\mathrm{d}\omega}\ .$$

This is the Fourier cosine transform of $I(\omega)$, normalized to the integrated intensity. In short, *the difference interferogram is the Fourier transform of the spectrum.*

3.4 Influence of misalignments

A detailed analysis of various types of interferometer misalignments and of their influence on the interferogram can be found in the literature (e.g. [Lam78], [Les90]). However, a relatively simple consideration can already give some insight.

Almost all conceivable misalignments of a Martin-Puplett interferometer have the effect in common that the interfering electric fields in front of the analyzer grid do not have the same amplitude anymore, as they would in a well-aligned instrument. We can imitate this by introducing a factor ξ to one of the two perpendicular fields in (3.2):

$$\boldsymbol{E}_\text{final}(t) = \boldsymbol{E}'_\text{t}(t) + \xi\boldsymbol{E}'_\text{r}(t) \tag{3.4}$$

The placement of the *misalignment parameter* ξ is arbitrary. A more practical definition is

$$\xi = \frac{\max(E'_\text{r}, E'_\text{t})}{\min(E'_\text{r}, E'_\text{t})}\ , \tag{3.5}$$

so ξ is the ratio of the electric field amplitudes of the two beams in front of the analyzer grid, and it is restricted to $0 \leqslant \xi \leqslant 1$.

The consequences of a misalignment with $\xi < 1$ are illustrated in Fig. 3.5. Even if the interferometer is set to an equal optical path length in both arms, the recombination of the partial beams does not yield horizontally polarized light anymore. The influence can be calculated by decomposing (3.4) into its horizontal and vertical components:

$$\boldsymbol{E}_\text{final}(t)/E_0 = \left(\frac{1-\xi}{2}\sin(\omega t-\omega\tau)+\xi\sin\left(\omega t-\frac{\omega\tau}{2}\right)\cos\frac{\omega\tau}{2}\right)\boldsymbol{u}_\text{h} + \left(\frac{\xi-1}{2}\sin(\omega t-\omega\tau)-\xi\cos\left(\omega t-\frac{\omega\tau}{2}\right)\sin\frac{\omega\tau}{2}\right)\boldsymbol{u}_\text{v}$$

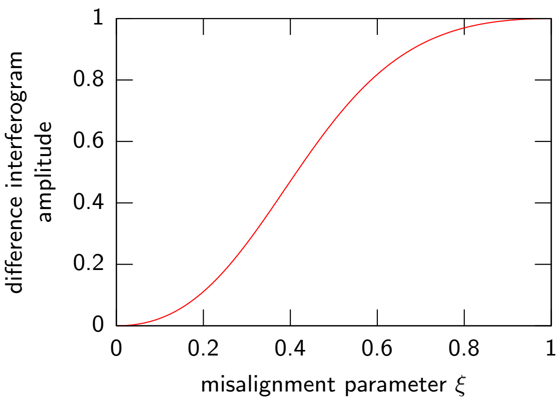

Figure 3.6: Amplitude of the difference interferogram as a function of the misalignment parameter ξ. For a perfectly aligned interferometer, ξ is unity.

This result is similar to (3.3), but the field components now have an additional, equal in-phase contribution. Proceeding to the detector intensities, we obtain

$$U_\text{h}(\tau) \propto \left(\frac{\xi^2}{2}\cos^2\frac{\omega\tau}{2}+\frac{(1-\xi)^2}{8}\right){E_0}^2$$
$$U_\text{v}(\tau) \propto \left(\frac{\xi^2}{2}\sin^2\frac{\omega\tau}{2}+\frac{(1-\xi)^2}{8}\right){E_0}^2\ .$$

So, if one of the two interfering beams in front of the analyzer has a different intensity than the other, a constant offset is found in the detected signals. The difference interferogram is affected as well, and the calculation leads to

$$\delta(\tau) = \frac{1}{1+\frac{1}{2}\left(\frac{1}{\xi}-1\right)^2}\,\frac{\int_0^\infty I(\omega)\cos(\omega\tau)\,\mathrm{d}\omega}{\int_0^\infty I(\omega)\,\mathrm{d}\omega}\ . \tag{3.6}$$

This is the same result as found before, except for a scaling factor that depends solely on the misalignment parameter ξ. The difference interferogram does not change, only its amplitude is influenced as shown in Fig. 3.6.

3.5 Comparison with the Michelson interferometer

When compared with interferometers of the Michelson type, the Martin-Puplett design reveals its most obvious advantage in having two outputs instead of one, because the differential measurement improves the signal-to-noise ratio. The fact that the total incoming intensity behind the initial polarizer matches the sum of the final intensities at the detectors permits a very accurate normalization, allowing to remove almost all effects originating from variations in the initial intensity. This feature is especially useful for synchrotron radiation measurements as the beam charge and other accelerator parameters can be subject to strong fluctuations.

In a Michelson interferometer, only one half of the initial intensity finds its way to the detector while the other half is reflected back in the direction of the source. Due to the nature of the central beam divider, the Martin-Puplett type ideally transports all of the incoming polarized light to the detectors. However, this advantage can only be brought to bear in the case of light having mainly the right polarization. Otherwise, a smaller or greater part of the radiation is reflected at the first wire grid, thus lowering the intensity yield of the Martin-Puplett instrument.

4 Kramers-Kronig analysis

Any intensity-based interferometry method is subject to the limitation that only the absolute value of the form factor can be measured, and not its complex phase. However, it is possible to recover the missing phase information by a *Kramers-Kronig analysis*, a technique proposed by R. Lai and A. J. Sievers in [Lai94] and summarized in [Lai97], that takes advantage of the formal similarity with the analysis used in optics to reconstruct complex reflectivities.

An outline of the mathematical foundations given in [Tol56] will be presented here in a form already adapted to the problem of deriving the complex form factor.

4.1 Definitions and prerequisites

Remembering that the complex form factor is the Fourier transform of the charge distribution[1] $\rho(t)$,

$$F(\omega) = \frac{1}{Q} \int_{-\infty}^{+\infty} \rho(t) \exp(-\mathrm{i}\omega t)\,\mathrm{d}t\ , \tag{4.1}$$

we know that $F(0) = 1$, and hence $|F(\omega)|$ is bounded by unity for all frequencies ω. For a real bunch of finite length it is also obvious that $F(\omega) \to 0$ for $\omega \to \infty$.

We are now looking for the most common expression for $F(\omega)$ for a given modulus $|F(\omega)|$. To facilitate the discussion of the problem, we do not require ω to be real, but allow for complex values. As we can assume that $\rho(t) \to 0$ for $t \to \infty$, it follows from (4.1) that the form factor is analytic[2] in the upper half of the complex ω plane. Furthermore, the reality of $\rho(t)$ determines the symmetry of the form factor $F(\omega_\mathrm{r})$ for real ω_r:

$$F(-\omega_\mathrm{r}) = F^*(\omega_\mathrm{r})$$

If we look at a complex $\omega = \omega_\mathrm{r} + \mathrm{i}\omega_\mathrm{i}$, it is easy to find a generalization of this rule:

$$F(-\omega_\mathrm{r} + \mathrm{i}\omega_\mathrm{i}) = F^*(\omega_\mathrm{r} + \mathrm{i}\omega_\mathrm{i}) \tag{4.2}$$

Postulating that the bound $|F(\omega)| \leqslant 1$ holds for all complex $\omega \in \mathbf{C}$, we can introduce a complex phase

$$\eta(\omega) = \eta_\mathrm{r}(\omega) + \mathrm{i}\eta_\mathrm{i}(\omega)$$

with $\eta_\mathrm{i}, \eta_\mathrm{r} \in \mathbf{R}$, $\eta_\mathrm{i} \geqslant 0$, and write $F(\omega)$ as

$$\begin{aligned} F(\omega) &= \exp(\mathrm{i}\eta(\omega)) \\ &= \exp(-\eta_\mathrm{i}(\omega)) \exp(\mathrm{i}\eta_\mathrm{r}(\omega))\ . \end{aligned}$$

The complex phase $\eta(\omega)$ is just another way of representing the form factor $F(\omega)$; both descriptions are equivalent and can be converted into each other. Solving for the phase, we get

$$\begin{aligned} \eta_\mathrm{i}(\omega) &= -\ln|F(\omega)| \\ \eta_\mathrm{r}(\omega) &= \arg F(\omega)\ . \end{aligned}$$

This means that the imaginary part of the phase is determined by the given absolute value of the form factor while the real part remains unknown. Although the information is insufficient for an exact determination of this real part, the knowledge of $\eta_\mathrm{i}(\omega)$ and of certain properties of $F(\omega)$ can be used to find some restraints, and especially a minimal value, for $\eta_\mathrm{r}(\omega)$.

4.2 Contributions to the form factor

Because we are only interested in the value of $F(\omega)$ for real ω, we may multiply it with any function provided that the absolute value $|F(\omega)|$ on the real ω axis is not changed and that the so-called *regularity condition* is still fulfilled – i.e. $F(\omega_\mathrm{r})$, $\omega_\mathrm{r} \in \mathbf{R}$, is the boundary value function of $F(\omega)$ which is itself bounded and analytic in the upper half of the complex ω plane.

One multiplicative term that complies with these requirements is the following:

$$B_n(\omega) = \frac{\omega - \mu_n}{\mu_n^* - \omega} \tag{4.3}$$

Here, μ_n is any number from the upper half of the complex plane. Obviously, $B_n(\omega)$ has exactly one zero at μ_n and one pole at μ_n^*, which means that there is no singularity in the upper half of the complex ω plane. For real ω_r, $|B_n(\omega_\mathrm{r})| = 1$ holds as required, ensuring that the absolute value of the form factor is not changed:

$$|B_n(\omega_\mathrm{r}) F(\omega_\mathrm{r})| = |F(\omega_\mathrm{r})|$$

Rewriting (4.3) with the real and imaginary parts of the differences, we get

$$B_n(\omega) = -\frac{\Re(\omega - \mu_n) + \mathrm{i}\Im(\omega - \mu_n)}{\Re(\omega - \mu_n) + \mathrm{i}\Im(\omega + \mu_n)}\ .$$

From this, we can see that $|B_n(\omega)| < 1$ holds in the upper half of the complex ω plane, with $\Im(\omega) > 0$ and $\Im(\mu_n) \geqslant 0$. Thus, the regularity condition is still met by $B_n(\omega)F(\omega)$.

Taking this into account, it can be shown that the most common form for $F(\omega)$ is

$$F(\omega) = \tilde{F}(\omega) B(\omega) C(\omega)$$

with $\tilde{F}(\omega)$ bounded, analytic, and *nonzero* in the upper half of the complex ω plane and $B(\omega)$ a product of the terms $B_n(\omega)$ examined above:[3]

$$\begin{aligned} B(\omega) &= \prod_n B_n(\omega) \\ &= \prod_n \frac{\omega - \mu_n}{\mu_n^* - \omega} \end{aligned}$$

The term $B(\omega)$ is called a *Blaschke product*. It introduces exactly n zeros in the upper half of the complex ω plane. The calculation of its phase when written as $B(\omega) = \exp(\mathrm{i}\xi(\omega))$ is straightforward and yields

$$\xi(\omega) = -\mathrm{i} \sum_n \ln \frac{\omega - \mu_n}{\omega - \mu_n^*}\ . \tag{4.4}$$

---

[1] As $\rho(t)$ actually carries the unit C/s, it would be more accurate to speak of a *current distribution*. However, in the context of bunch lengths it is often used interchangeably with the spatial $\rho(x)$, and therefore both are comprehended under the same notion.

[2] A function $f : U \subseteq \mathbf{C} \to \mathbf{C}$ is referred to as *analytic* (or holomorphic) on an open set U if f is complex differentiable at every point in U [Bro96].

[3] [Tol56] refers to [Nev36] and [Sho43] for a discussion of this mathematical theorem, as well as to personal communications with Prof. Marcel Riesz.

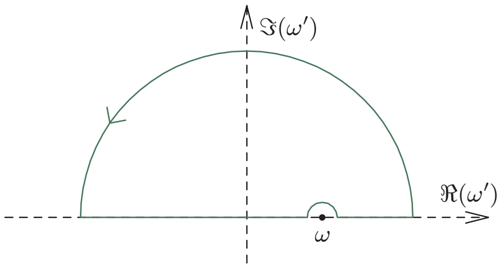

Figure 4.1: Integration path for equations (4.6) and (4.7). $f(\omega')$ is singular at $\omega' = \omega$.

Bearing in mind the definition of the complex logarithm, $\ln z = \ln|z| + \mathrm{i} \arg z$, we can conclude from the discussion of the single terms $B_n(\omega)$ above that the imaginary part of $\xi(\omega)$ is in fact zero on the real axis, i.e. for $\omega_\mathrm{r} \in \mathbf{R}$

$$\xi(\omega_\mathrm{r}) = \sum_n \arg \frac{\omega_\mathrm{r} - \mu_n}{\omega_\mathrm{r} - \mu_n^*}$$

holds, which can be shown to be a monotonically increasing, positive function of frequency.

$C(\omega)$ is a negligible term in our case. It contains a factor $\exp(\mathrm{i}d\omega)$, $d \in \mathbf{R}_0^+$, that merely introduces a constant displacement of the bunch, so we may arbitrarily choose $d = 0$. If furthermore $\eta(\omega)$ is continuous on the real ω axis, it can be assumed that $C(\omega) = 1$.

Under these circumstances, $\tilde{F}(\omega)$ can be understood as the function $F(\omega)$ after removal of its complex zeros. For convenience, this can again be expressed in phase form as $\tilde{F}(\omega) = \exp(\mathrm{i}\tilde{\eta}(\omega))$. Looking at the total phase for our form factor, we get

$$\eta(\omega) = \tilde{\eta}(\omega) + \xi(\omega) \ . \tag{4.5}$$

This means that $\tilde{\eta}(\omega)$ is the *minimal phase* allowed by specifying a certain $|F(\omega)|$, and also the phase minimally increasing with ω — which is a statement that must be understood in the context that terms growing linearly with ω have already been disregarded. However, there may be a contribution from complex zeros of the form factor in the upper half ω plane. These terms $\xi(\omega)$, the phases of the Blaschke products, make the actual phase rise faster than the minimal one.

There seems to be no way to determine the magnitude of $\xi(\omega)$ from the modulus of a form factor. However, it will be shown that the minimal phase can be calculated. Hence, the Blaschke phase can be obtained from (4.5) if a bunch shape – and with it a full complex form factor – is specified. This way, it can be shown that the minimal phase is a good approximation of the actual form factor phase for bunch shapes typically expected in accelerators, including single or superpositions of multiple Gaussians, and simple asymmetric shapes [Lai97].

Still, the Blaschke contribution can be non-negligible for certain atypical shapes like symmetric Lorentzian distributions. But even in these cases, basic parameters of the density distribution like peak width and amplitude are found to be largely preserved.

4.3 Derivation of the minimal phase

To find a connection between the initially known $\eta_\mathrm{i}(\omega)$ and the minimal phase $\tilde{\eta}(\omega)$, a reasonable starting point would be to make use of Cauchy's integral formula to get an integral expression for $\tilde{\eta}(\omega)$:

$$\tilde{\eta}(\omega) = \frac{1}{2\pi\mathrm{i}} \oint_\kappa \frac{\tilde{\eta}(\omega')}{\omega' - \omega} \mathrm{d}\omega' \tag{4.6}$$

Here, κ could be any contour enclosing the point ω counterclockwise. However, we know that $F(\omega')$ approaches zero for $|\omega'| \to \infty$, which in turn means for the phase that $|\eta(\omega')| = |-\mathrm{i} \ln F(\omega')| \to \infty$. Hence the integral (4.6) cannot be evaluated properly. Instead we choose a more well-behaved function and follow the derivation given in [Woo72]:

$$f(\omega') = \frac{(1 + \omega\omega')\mathrm{i}\tilde{\eta}(\omega')}{(1 + \omega'^2)(\omega - \omega')}$$

It is plausible and can be rigorously proven that $|f(\omega')| \to 0$ for $|\omega'| \to \infty$.

If we now choose an integration contour κ consisting of a counterclockwise semicircle in the upper half of the complex ω plane and a return path along the real axis, we realize the existence of a singularity of $f(\omega')$ at $\omega' = \omega$. Therefore, we give κ a small detour above this point as shown in Fig. 4.1. Using the residue theorem, we can then write

$$\oint_\kappa f(\omega')\,\mathrm{d}\omega' = 2\pi\mathrm{i} \sum_{j=1}^{n} \operatorname{Res} f(\omega_j) \ . \tag{4.7}$$

Now we have to look for singularities to calculate the complex residues on the right hand side of (4.7). Knowing that $\tilde{F}(\omega')$ has no zeros in the upper half plane, $\tilde{\eta}(\omega')$ has no singularities itself. From the definition of $f(\omega')$ we can then conclude that there is only one singular point at $\omega' = \mathrm{i}$, so we may write

$$\oint_\kappa f(\omega')\,\mathrm{d}\omega' = 2\pi\mathrm{i} \operatorname{Res} f(\mathrm{i}) \ . \tag{4.8}$$

Now the radius of the upper semicircle of the contour κ is extended to infinity. The properties of $f(\omega')$ are such that the corresponding contribution to the integral vanishes. Two parts remain, firstly the path along the real axis excluding the pole $\omega' = \omega$, which is a construct referred to as the *Cauchy principal value*, commonly designated by PV [Bro96]:

$$\begin{aligned} \mathrm{PV} \int_{-\infty}^{+\infty} f(\omega')\,\mathrm{d}\omega' = \\ \lim_{\epsilon \to +0} \left(\int_{-\infty}^{\omega-\epsilon} f(\omega')\,\mathrm{d}\omega' + \int_{\omega+\epsilon}^{\infty} f(\omega')\,\mathrm{d}\omega' \right) \end{aligned}$$

The second remaining part of the contour integral originates from the singularity itself; the corresponding section of the integration path is an infinitesimally small semicircle above ω. The integral can be calculated if we let $\omega' = \omega + \epsilon \exp \mathrm{i}\phi$:

$$\begin{aligned} \int_{\frown} f(\omega')\mathrm{d}\omega' &= \lim_{\epsilon \to 0} \int_\pi^0 f(\omega + \epsilon \exp \mathrm{i}\phi)\,\mathrm{d}(\omega + \epsilon \exp \mathrm{i}\phi) \\ &= \int_\pi^0 \frac{(1 + \omega^2)\mathrm{i}\tilde{\eta}(\omega) \cdot \mathrm{i}\epsilon \exp \mathrm{i}\phi}{(1 + \omega^2)(\omega - \omega - \epsilon \exp \mathrm{i}\phi)}\,\mathrm{d}\phi \\ &= -\pi\tilde{\eta}(\omega) \end{aligned}$$

Inserting these two parts in (4.8), only the residue of $f(\mathrm{i})$ remains to be determined:

$$\begin{aligned} \mathrm{PV}\int_{-\infty}^{+\infty} f(\omega')\,\mathrm{d}\omega' - \pi\tilde{\eta}(\omega) &= 2\pi\mathrm{i}\,\mathrm{Res}\,f(\mathrm{i}) \\ &= 2\pi\mathrm{i}\,\frac{\tilde{\eta}(\mathrm{i})(\omega-\mathrm{i})}{-2(1+\mathrm{i}\omega)} \\ &= -\pi\tilde{\eta}(\mathrm{i}) \qquad (4.9) \end{aligned}$$

To proceed, some insight to the properties of $\tilde{\eta}(\mathrm{i})$ is required. If we remember the symmetry condition (4.2) and rewrite it with respect to the complex phase, we get

$$\begin{aligned} \eta_{\mathrm{r}}(-\omega_{\mathrm{r}}+\mathrm{i}\omega_{\mathrm{i}}) &= -\eta_{\mathrm{r}}(\omega_{\mathrm{r}}+\mathrm{i}\omega_{\mathrm{i}}) \\ \eta_{\mathrm{i}}(-\omega_{\mathrm{r}}+\mathrm{i}\omega_{\mathrm{i}}) &= \eta_{\mathrm{i}}(\omega_{\mathrm{r}}+\mathrm{i}\omega_{\mathrm{i}}) \end{aligned}$$

or, in more condensed but less readable form,

$$\eta(\omega) = -\eta^*(-\omega^*)\ . \qquad (4.10)$$

It is now obvious that $\eta(\mathrm{i})$ is imaginary for $\omega_{\mathrm{r}} = 0$. Because the charge distribution $\rho(t)$ is real, complex zeros of the form factor also appear symmetrically, i.e. a zero at μ_j always has a twin at $-\mu_j^*$. Thus, the contribution of the Blaschke product is symmetrical with respect to the imaginary axis, and (4.10) is valid for the minimal phase $\tilde{\eta}(\omega)$ as well. So finally, we are able to conclude that $\tilde{\eta}(\mathrm{i})$ *is imaginary.*

We make use of this finding by taking the real part of equation (4.9):

$$\Re\left[\mathrm{PV}\int_{-\infty}^{+\infty}\frac{(1+\omega\omega')\mathrm{i}\tilde{\eta}(\omega')}{(1+\omega'^2)(\omega-\omega')}\,\mathrm{d}\omega'\right] = \Re\left[\pi\tilde{\eta}(\omega)-\pi\tilde{\eta}(\mathrm{i})\right]$$

$$\mathrm{PV}\int_{-\infty}^{+\infty}\frac{-(1+\omega\omega')\tilde{\eta}_{\mathrm{i}}(\omega')}{(1+\omega'^2)(\omega-\omega')}\,\mathrm{d}\omega' = \pi\tilde{\eta}_{\mathrm{r}}(\omega) \qquad (4.11)$$

As stated above, (4.10) is a valid symmetry relation also for the minimal phase $\tilde{\eta}(\omega)$, i.e. for real frequencies $\tilde{\eta}(-\omega_{\mathrm{r}}) = -\tilde{\eta}^*(\omega_{\mathrm{r}})$. With this, we can now transform the integral (4.11) to cover only positive frequencies:

$$\begin{aligned} \tilde{\eta}_{\mathrm{r}}(\omega) &= \frac{1}{\pi}\Bigg(\ \mathrm{PV}\int_{-\infty}^{0}\frac{-(1+\omega\omega')\tilde{\eta}_{\mathrm{i}}(\omega')}{(1+\omega'^2)(\omega-\omega')}\,\mathrm{d}\omega' \\ &\qquad +\mathrm{PV}\int_{0}^{\infty}\frac{-(1+\omega\omega')\tilde{\eta}_{\mathrm{i}}(\omega')}{(1+\omega'^2)(\omega-\omega')}\,\mathrm{d}\omega'\ \Bigg) \\ &= \frac{1}{\pi}\Bigg(-\mathrm{PV}\int_{0}^{\infty}\frac{-(1+\omega(-\omega'))\tilde{\eta}_{\mathrm{i}}(-\omega')}{(1+(-\omega')^2)(\omega-(-\omega'))}\,\mathrm{d}\omega' \\ &\qquad +\mathrm{PV}\int_{0}^{\infty}\frac{-(1+\omega\omega')\tilde{\eta}_{\mathrm{i}}(\omega')}{(1+\omega'^2)(\omega-\omega')}\,\mathrm{d}\omega'\ \Bigg) \\ &= \frac{1}{\pi}\ \mathrm{PV}\int_{0}^{\infty}\frac{\tilde{\eta}_{\mathrm{i}}(\omega')}{(1+\omega'^2)(\omega^2-\omega'^2)}\cdot \\ &\qquad \Big[(-1+\omega\omega')(\omega-\omega')+ \\ &\qquad (-1-\omega\omega')(\omega+\omega')\Big]\,\mathrm{d}\omega' \\ &= -\frac{2\omega}{\pi}\ \mathrm{PV}\int_{0}^{\infty}\frac{\tilde{\eta}_{\mathrm{i}}(\omega')}{\omega^2-\omega'^2}\,\mathrm{d}\omega' \qquad (4.12) \end{aligned}$$

To dispose of the singularity at $\omega' = \omega$, we can once more apply a well-known trick from complex analysis by introducing an integral of value zero:

$$\frac{2\omega}{\pi}\ \mathrm{PV}\int_{0}^{\infty}\frac{\tilde{\eta}_{\mathrm{i}}(\omega)}{\omega^2-\omega'^2}\,\mathrm{d}\omega' = 0 \qquad (4.13)$$

The validity of (4.13) can be shown by an integration similar to the one carried out above. If we now add (4.13) to (4.12), the singularity is replaced by a removable discontinuity, and thus the need to take the Cauchy principal value is lifted:

$$\tilde{\eta}_{\mathrm{r}}(\omega) = \frac{2\omega}{\pi}\int_{0}^{\infty}\frac{\tilde{\eta}_{\mathrm{i}}(\omega)-\tilde{\eta}_{\mathrm{i}}(\omega')}{\omega^2-\omega'^2}\,\mathrm{d}\omega' \qquad (4.14)$$

This is the *Kramers-Kronig relation* for the minimal phase. It can be recognized immediately that in this integral formula the real part of the phase depends only on its own imaginary part and vice versa. However, as yet it does not contain information on how to calculate the minimal phase from known quantities. As a matter of fact, the final step is simple when we remember that $|F(\omega_{\mathrm{r}})| = |\tilde{F}(\omega_{\mathrm{r}})|$ and hence $\eta_{\mathrm{i}}(\omega_{\mathrm{r}}) = \tilde{\eta}_{\mathrm{i}}(\omega_{\mathrm{r}})$. Insertion into (4.14) yields the final expression for the calculation of the minimal phase,

$$\tilde{\eta}_{\mathrm{r}}(\omega) = \frac{2\omega}{\pi}\int_{0}^{\infty}\frac{\eta_{\mathrm{i}}(\omega)-\eta_{\mathrm{i}}(\omega')}{\omega^2-\omega'^2}\,\mathrm{d}\omega' \qquad (4.15)$$

$$\text{or}\quad \tilde{\eta}_{\mathrm{r}}(\omega) = \frac{2\omega}{\pi}\int_{0}^{\infty}\frac{\ln\frac{|F(\omega')|}{|F(\omega)|}}{\omega^2-\omega'^2}\,\mathrm{d}\omega'\ . \qquad (4.16)$$

5 Experimental setup

In this chapter, an overview of the experimental setup used for interferometry with coherent synchrotron radiation is given, together with an analysis of its expected influence on the measurement results. If necessary, the functional principle of single components is discussed as well.

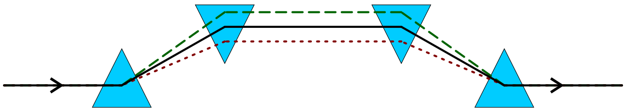

Figure 5.1: Functional principle of a bunch compressor. A magnetic chicane introduces a dispersive section to the accelerator in a way that electrons with a lower-than-nominal energy have a longer orbit (dashed) and those with higher energy have a shorter orbit (dotted).

5.1 Injector and bunch compressor

High peak beam current and low transverse emittance are needed to operate a high-gain FEL. Both of these parameters are intrinsically limited by the performance of the injector. For a bunch charge of 1 nC, the current VUV-FEL photoinjector is capable of generating an electron beam with a normalized emittance of 1.7 mm mrad as geometrical average of the horizontal and vertical plane [Ste04]. The charge is extracted from a photocathode with a laser pulse and accelerated in the 1 1/2-cell RF cavity of the gun, generating a longitudinally Gaussian-shaped bunch[1] with an RMS width of (1.7 ± 0.2) mm, as measured with a streak camera in the BC2 section [Hon04]. As the maximum charge density in the sub-relativistic energy domain of the gun is limited by space-charge effects, the electron bunches need to be compressed to reach the desired high peak current of about 2500 A at ultra-relativistic energies.

At the VUV-FEL, bunch compression is achieved by two magnetic chicanes. The first, BC2, consists of four equal dipole magnets that are arranged in the shape of a “C”, or trapezoid. The second, BC3, is “S”-shaped and will not be discussed here. Nevertheless, its basic functional principle is the same; a detailed comparison of bunch compressor geometries is found in [Stu04].

The dipoles of BC2 are all driven by the same power supply in a series connection to make their magnetic field differ only in sign. This ideally introduces a section of closed dispersion to the linac. Because the deflection of charges in a dipole field is energy-dependent, electrons with higher energy will have a shorter trajectory through the magnetic chicane than those with lower energy (Fig. 5.1). To take advantage of this, an energy slope has to be induced along the bunch in such a way that the particles in its front part have smaller energy than those in its rear part. This is achieved by shifting the phase of the accelerating RF wave so that the electron packet is not accelerated on the peak of the electric field (“on-crest” operation), but on its ascending slope (“off-crest”), as illustrated in Fig. 5.2.

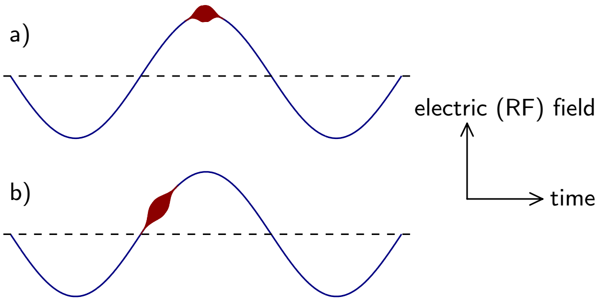

Figure 5.2: Comparison of different acceleration phases.
a) On-crest operation. The RF field is nearly constant over the length of the bunch.
b) Off-crest operation. The head of the bunch (i.e. the end with earlier arrival time) experiences a lower acceleration field than the tail.

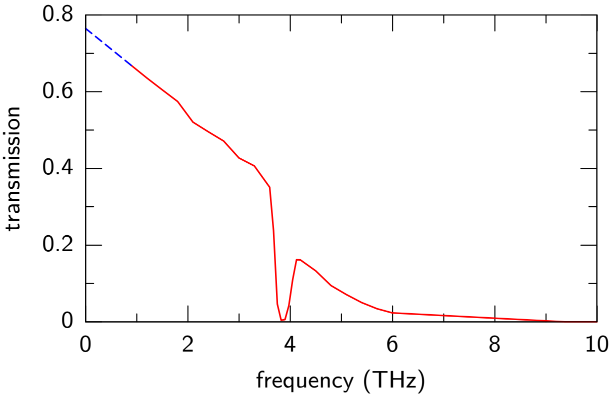

Figure 5.3: Transmission of the BC2 vacuum chamber window. The values have been calculated for 4.8 mm thick crystalline α-quartz using data from [Pal97]. Below 900 GHz, the transmission has been extrapolated linearly.

5.1.1 Vacuum chamber window

Synchrotron radiation is extracted from the last dipole magnet of the bunch compressor through a commercially available 4.8 mm thick vacuum window made of a z-cut quartz single crystal (see Fig. A.4). Its transmission for terahertz radiation has been calculated from the absorption coefficients given in [Pal97] and is shown in Fig. 5.3. A strong absorption band at 3.8 THz is discernible that virtually constitutes an upper limit for spectral measurements. Because no experimental data is known for the transmission below 900 GHz, the curve is extrapolated linearly.

In the spectral range of 0–3.5 THz, the transmission drops roughly by a factor of two. In interferometer measurements, this is corrected by use of an appropriate transfer function (cf. section 6.3.3).

---

[1] The gun reaches its minimum possible emittance only with a “flat-top”, i.e. a rectangular laser pulse. In the cited measurement, this was achieved using a laser pulse shaper. However, no such pulse shaper is currently installed at the VUV-FEL.

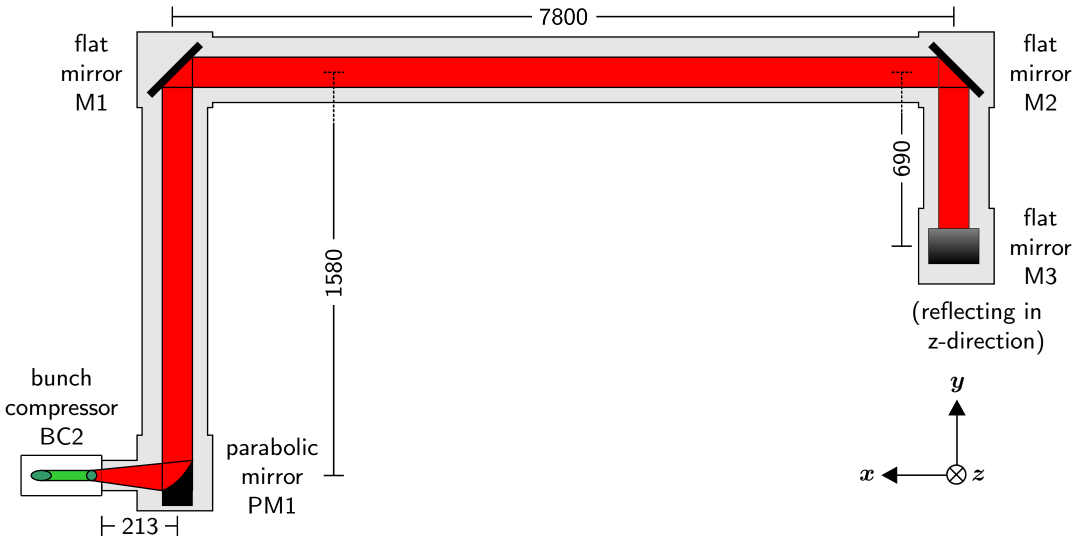

Figure 5.4: Sketch of the infrared beam transfer line. All measures are given in mm. M3 reflects the beam perpendicularly onto the polarizer grid of the interferometer.

mirror	diameter
PM1	100 mm
M1	250 mm
M2	150 mm
M3	150 mm

Table 5.1: Mirror sizes for the radiation transfer line. All flat mirrors have circular shape. For the paraboloid, the diameter of the cylinder from which the surface is milled is given.

5.2 The radiation transfer line

For easier access, the interferometer is not placed in the accelerator tunnel, but in a laboratory container outside. The radiation is transported there by a set of mirrors as shown in Fig. 5.4. The first one is an off-axis paraboloid[2] placed at a distance of 21 cm from the vacuum window. Its effective focal length of 81 cm has been chosen based on the assumption that the focal point coincides with the beam position in the vacuum chamber at the beginning of the last dipole magnet. Thus, the radiation beam is parallelized and reflected upwards onto a flat mirror oriented at 45° against the yz-plane. This mirror deflect the beam outside the tunnel, and two others lead it down to the level of the experiment and finally in z-direction into the interferometer. Because the optics of terahertz waves is strongly diffraction-limited, the sizes of all mirrors have been laid out generously; a list of the diameters is given in Tab. 5.1. All mirrors are adjustable in two angles to allow an optimization of the transmission of the transfer line.

The whole transfer line is enclosed by blackened metallic tubes of at least 20 cm diameter, the mirrors and the interferometer are placed in black plastic or metallic casings. The system can be flooded with dry nitrogen from the interferometer end while a small hole near the vacuum window provides for venting. As a homonuclear diatomic molecule, N_2 has no permanent dipole moment and consequently does not show any absorption in the infrared or far-infrared at normal pressures. Although the transfer line is not expected to be wholly gas-tight, the nitrogen flushing is capable of strongly reducing the absorption effects of water vapor.

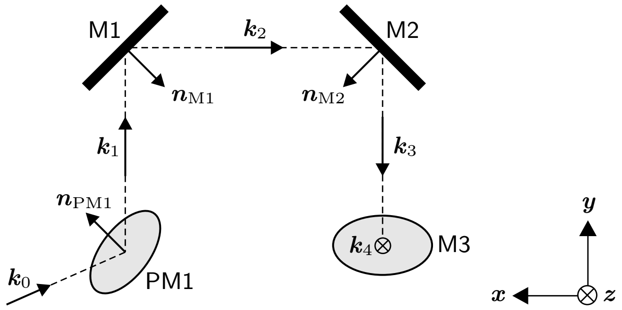

Figure 5.5: Sketch of the transfer line with the vector designations used in the model

5.2.1 Mathematical model of the transfer line

It is not obvious how the alignment of the four mirrors affects the polarization of the transported light. Hence, a simple mathematical model of the transfer line has been developed. To facilitate the description of the beam transfer line, the parabolic mirror PM1 is treated as a flat mirror, and the incident radiation is assumed to be a plane wave. This way, only a single wave vector needs to be traced, using the law of reflection. As we are only interested in the direction of the electric field and of the wave vectors, we can restrict the discussion to unit vectors. Let $\boldsymbol{n}_{\mathrm{PM1}}$, $\boldsymbol{n}_{\mathrm{M1}}$, $\boldsymbol{n}_{\mathrm{M2}}$, $\boldsymbol{n}_{\mathrm{M3}}$ be the normals of the mirrors as displayed in Fig. 5.5. If $\tilde{\boldsymbol{k}}_0$ is the normalized wave vector of a plane electromagnetic wave incident on PM1, the direction of the reflected waves is given by

$$\begin{aligned}
\tilde{\boldsymbol{k}}_1 &= \tilde{\boldsymbol{k}}_0 - (2\boldsymbol{n}_{\mathrm{PM1}} \cdot \tilde{\boldsymbol{k}}_0)\, \boldsymbol{n}_{\mathrm{PM1}} \\
\tilde{\boldsymbol{k}}_2 &= \tilde{\boldsymbol{k}}_1 - (2\boldsymbol{n}_{\mathrm{M1}} \cdot \tilde{\boldsymbol{k}}_1)\, \boldsymbol{n}_{\mathrm{M1}} \\
\tilde{\boldsymbol{k}}_3 &= \tilde{\boldsymbol{k}}_2 - (2\boldsymbol{n}_{\mathrm{M2}} \cdot \tilde{\boldsymbol{k}}_2)\, \boldsymbol{n}_{\mathrm{M2}} \\
\tilde{\boldsymbol{k}}_4 &= \tilde{\boldsymbol{k}}_3 - (2\boldsymbol{n}_{\mathrm{M3}} \cdot \tilde{\boldsymbol{k}}_3)\, \boldsymbol{n}_{\mathrm{M3}} \ ,
\end{aligned} \tag{5.1}$$

with $\tilde{\boldsymbol{k}}_4$ specifying the direction of incidence onto the polarizer grid of the Martin-Puplett interferometer.

In the case of reflection at a perfectly conducting surface, the component of the electric field perpendicular to the plane of incidence retains amplitude and direction (except

---

[2] See section 5.3.3 for a short description of the functional principle of an off-axis parabolic mirror.

for a phase jump of 180°, which is not of concern for this consideration). The amplitude of the parallel component also stays constant, but the direction changes to obey the law of reflection. We designate the plane of incidence that is spanned by $\tilde{\boldsymbol{k}}_{\text{in}}$ and $\tilde{\boldsymbol{k}}_{\text{out}}$ by means of the unit normal vector $\boldsymbol{u} = \tilde{\boldsymbol{k}}_{\text{in}} \times \tilde{\boldsymbol{k}}_{\text{out}}$, and for the mirrors of the transfer line we obtain

$$\begin{aligned} \boldsymbol{u}_{\text{PM1}} &= \tilde{\boldsymbol{k}}_0 \times \tilde{\boldsymbol{k}}_1 \\ \boldsymbol{u}_{\text{M1}} &= \tilde{\boldsymbol{k}}_1 \times \tilde{\boldsymbol{k}}_2 \\ \boldsymbol{u}_{\text{M2}} &= \tilde{\boldsymbol{k}}_2 \times \tilde{\boldsymbol{k}}_3 \\ \boldsymbol{u}_{\text{M3}} &= \tilde{\boldsymbol{k}}_3 \times \tilde{\boldsymbol{k}}_4 \ . \end{aligned} \tag{5.2}$$

The two components of the incident electric field vector can then be calculated as

$$\tilde{E}_\perp = \tilde{\boldsymbol{E}}_{\text{in}} \cdot \boldsymbol{u}, \qquad \tilde{E}_\parallel = \left| \tilde{\boldsymbol{E}}_{\text{in}} \times \boldsymbol{u} \right| \ ,$$

and the reflected electric fields are found by combining these components with the appropriate direction vectors:

$$\begin{aligned} \tilde{\boldsymbol{E}}_1 &= \left(\tilde{\boldsymbol{E}}_0 \cdot \boldsymbol{u}_{\text{PM1}}\right) \boldsymbol{u}_{\text{PM1}} + \left|\tilde{\boldsymbol{E}}_0 \times \boldsymbol{u}_{\text{PM1}}\right| \left(\boldsymbol{u}_{\text{PM1}} \times \tilde{\boldsymbol{k}}_1\right) \\ \tilde{\boldsymbol{E}}_2 &= \left(\tilde{\boldsymbol{E}}_1 \cdot \boldsymbol{u}_{\text{M1}}\right) \boldsymbol{u}_{\text{M1}} + \left|\tilde{\boldsymbol{E}}_1 \times \boldsymbol{u}_{\text{M1}}\right| \left(\boldsymbol{u}_{\text{M1}} \times \tilde{\boldsymbol{k}}_2\right) \\ \tilde{\boldsymbol{E}}_3 &= \left(\tilde{\boldsymbol{E}}_2 \cdot \boldsymbol{u}_{\text{M2}}\right) \boldsymbol{u}_{\text{M2}} + \left|\tilde{\boldsymbol{E}}_2 \times \boldsymbol{u}_{\text{M2}}\right| \left(\boldsymbol{u}_{\text{M2}} \times \tilde{\boldsymbol{k}}_3\right) \\ \tilde{\boldsymbol{E}}_4 &= \left(\tilde{\boldsymbol{E}}_3 \cdot \boldsymbol{u}_{\text{M3}}\right) \boldsymbol{u}_{\text{M3}} + \left|\tilde{\boldsymbol{E}}_3 \times \boldsymbol{u}_{\text{M3}}\right| \left(\boldsymbol{u}_{\text{M3}} \times \tilde{\boldsymbol{k}}_4\right) \end{aligned} \tag{5.3}$$

With the help of equations (5.1), (5.2), (5.3) it is now possible to calculate the polarization of the plane wave in each section of the transfer line. For a first check of the model, the mirrors are placed in a way to obtain an optical path with only right angles. The wavefront incident on PM1 is assumed to be horizontally polarized and to propagate in z-direction, and the paraboloid itself is only reflecting upwards. The normal vectors of the mirrors, and the resulting wave vectors, planes of incidence, and electric field vectors are summarized in Tab. 5.2.

It is found that the electric field of the wave entering the interferometer is pointing in x-direction. This meets the expectations that horizontally polarized light incident on one end of the ideal transfer line is mapped to horizontally polarized light on the other end.

However, in the actual setup the CSR beam is not leaving the vacuum chamber in z-direction, but under an angle of about 18° as shown in Fig. A.4. This situation is described by an incident unit wave vector of

$$\tilde{\boldsymbol{k}}_0 = (-\sin(18°),\, 0,\, \cos(18°))$$

and the corresponding unit vector of the electric field for horizontal polarization,

$$\tilde{\boldsymbol{E}}_0 = (-\cos(18°),\, 0,\, -\sin(18°)) \ .$$

Of course it is also necessary to turn PM1 towards the vacuum window to obtain a correctly upwards-reflected beam:

$$\boldsymbol{n}_{\text{PM1}} = (\sin(18°),\, 1,\, -\cos(18°)) \,/\sqrt{2}$$

Under these initial conditions, the calculation summarized in Tab. 5.3 shows that the resulting polarization in front of the interferometer is tilted by 18° against the horizontal plane. As the wires of the polarizer grid are usually oriented vertically, this means the loss of a fraction of $\sin^2(18°) \approx 10\%$ of the incident radiation intensity.

A comparatively easy remedy for this problem is to turn the final mirror around its y-axis so that the beam reflected by M3 is parallel to the incident beam at the beginning of the transfer line. Table 5.4 shows that in this case the plane of polarization is restored to the xz-plane. As the wave vector incident on the interferometer also changes its direction, a relocation of the whole instrument is needed as well.

Another option is to adjust the polarizer angle to match the tilted plane of polarization. However, this would cause exactly the alignment error discussed in section 3.4, because the intensities of the two partial beams after transmission and reflection at the 45°-aligned beam divider grid would differ. In terms of the electric field, this means

$$\begin{aligned} E_{\text{r}} &= E_0 \cos(45° - 18°) \\ E_{\text{t}} &= E_0 \sin(45° - 18°) \ , \end{aligned}$$

and using definition (3.5), we find a misalignment parameter of $\xi = 0.51$. Following (3.6), the amplitude of the difference interferogram would hence be reduced to 68%.

Compared with the intensity loss of 10%, the latter option is clearly unacceptable. The vertical alignment of the polarizer wires should be retained, and the final transfer line mirror and the interferometer itself should be adjusted in angle as far as this is possible without requiring additional constructional effort.

completely rectangular optical path	
mirror normals	**wave vectors**
$\boldsymbol{n}_{\mathrm{PM1}} = (0, 1, -1)/\sqrt{2}$ $\boldsymbol{n}_{\mathrm{M1}} = (-1, -1, 0)/\sqrt{2}$ $\boldsymbol{n}_{\mathrm{M2}} = (1, -1, 0)/\sqrt{2}$ $\boldsymbol{n}_{\mathrm{M3}} = (0, 1, 1)/\sqrt{2}$	$\tilde{\boldsymbol{k}}_0 = (0, 0, 1)$ $\tilde{\boldsymbol{k}}_1 = (0, 1, 0)$ $\tilde{\boldsymbol{k}}_2 = (-1, 0, 0)$ $\tilde{\boldsymbol{k}}_3 = (0, -1, 0)$ $\tilde{\boldsymbol{k}}_4 = (0, 0, 1)$
plane-of-incidence normals	**electric field**
$\boldsymbol{u}_{\mathrm{PM1}} = (-1, 0, 0)$ $\boldsymbol{u}_{\mathrm{M1}} = (0, 0, 1)$ $\boldsymbol{u}_{\mathrm{M2}} = (0, 0, 1)$ $\boldsymbol{u}_{\mathrm{M3}} = (-1, 0, 0)$	$\tilde{\boldsymbol{E}}_0 = (1, 0, 0)$ $\tilde{\boldsymbol{E}}_1 = (1, 0, 0)$ $\tilde{\boldsymbol{E}}_2 = (0, -1, 0)$ $\tilde{\boldsymbol{E}}_3 = (1, 0, 0)$ $\tilde{\boldsymbol{E}}_4 = (1, 0, 0)$

Table 5.2: Unit vectors specifying the directions of mirrors, wave vectors, planes of incidence, and electric fields for an ideal beam transfer line with exact right angles. The vectors are specified as (x, y, z) triples following the coordinate system indicated in Fig. 5.5.

actual transfer line setup	
mirror normals	**wave vectors**
$\boldsymbol{n}_{\mathrm{PM1}} = (\sin 18°, 1, -\cos 18°)/\sqrt{2}$ $\boldsymbol{n}_{\mathrm{M1}} = (-1, -1, 0)/\sqrt{2}$ $\boldsymbol{n}_{\mathrm{M2}} = (1, -1, 0)/\sqrt{2}$ $\boldsymbol{n}_{\mathrm{M3}} = (0, 1, 1)/\sqrt{2}$	$\tilde{\boldsymbol{k}}_0 = (-\sin 18°, 0, \cos 18°)$ $\tilde{\boldsymbol{k}}_1 = (0, 1, 0)$ $\tilde{\boldsymbol{k}}_2 = (-1, 0, 0)$ $\tilde{\boldsymbol{k}}_3 = (0, -1, 0)$ $\tilde{\boldsymbol{k}}_4 = (0, 0, 1)$
plane-of-incidence normals	**electric field**
$\boldsymbol{u}_{\mathrm{PM1}} = (-\cos 18°, 0, -\sin 18°)$ $\boldsymbol{u}_{\mathrm{M1}} = (0, 0, 1)$ $\boldsymbol{u}_{\mathrm{M2}} = (0, 0, 1)$ $\boldsymbol{u}_{\mathrm{M3}} = (-1, 0, 0)$	$\tilde{\boldsymbol{E}}_0 = (-\cos 18°, 0, -\sin 18°)$ $\tilde{\boldsymbol{E}}_1 = (-\cos 18°, 0, -\sin 18°)$ $\tilde{\boldsymbol{E}}_2 = (0, -\cos 18°, -\sin 18°)$ $\tilde{\boldsymbol{E}}_3 = (\cos 18°, 0, -\sin 18°)$ $\tilde{\boldsymbol{E}}_4 = (\cos 18°, \sin 18°, 0)$

Table 5.3: Unit vectors for the actual setup of the beam transfer line (assuming design orientations). The resulting polarization is tilted against the horizontal plane by 18°.

improved transfer line setup	
mirror normals	**wave vectors**
$\boldsymbol{n}_{\mathrm{PM1}} = (\sin 18°, 1, -\cos 18°)/\sqrt{2}$ $\boldsymbol{n}_{\mathrm{M1}} = (-1, -1, 0)/\sqrt{2}$ $\boldsymbol{n}_{\mathrm{M2}} = (1, -1, 0)/\sqrt{2}$ $\boldsymbol{n}_{\mathrm{M3}} = (\sin 18°, 1, \cos 18°)/\sqrt{2}$	$\tilde{\boldsymbol{k}}_0 = (-\sin 18°, 0, \cos 18°)$ $\tilde{\boldsymbol{k}}_1 = (0, 1, 0)$ $\tilde{\boldsymbol{k}}_2 = (-1, 0, 0)$ $\tilde{\boldsymbol{k}}_3 = (0, -1, 0)$ $\tilde{\boldsymbol{k}}_4 = (\sin 18°, 0, \cos 18°)$
plane-of-incidence normals	**electric field**
$\boldsymbol{u}_{\mathrm{PM1}} = (-\cos 18°, 0, -\sin 18°)$ $\boldsymbol{u}_{\mathrm{M1}} = (0, 0, 1)$ $\boldsymbol{u}_{\mathrm{M2}} = (0, 0, 1)$ $\boldsymbol{u}_{\mathrm{M3}} = (-\cos 18°, 0, \sin 18°)$	$\tilde{\boldsymbol{E}}_0 = (-\cos 18°, 0, -\sin 18°)$ $\tilde{\boldsymbol{E}}_1 = (-\cos 18°, 0, -\sin 18°)$ $\tilde{\boldsymbol{E}}_2 = (0, -\cos 18°, -\sin 18°)$ $\tilde{\boldsymbol{E}}_3 = (\cos 18°, 0, -\sin 18°)$ $\tilde{\boldsymbol{E}}_4 = (\cos 18°, 0, -\sin 18°)$

Table 5.4: Unit vectors for an improved setup of the beam transfer line. The resulting polarization is in the xz-plane.

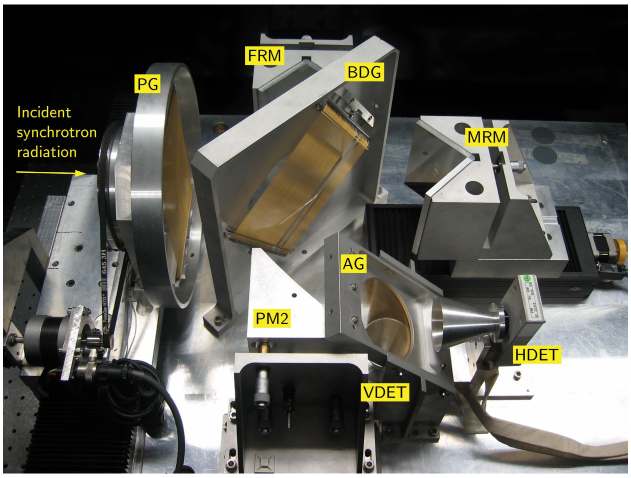

Figure 5.6: Photograph of the interferometer setup. The depicted elements are: PG – Rotatable polarizer grid. BDG – Beam divider grid. FRM – Fixed roof mirror. MRM – Moveable roof mirror. PM2 – Parabolic mirror. AG – Analyzer grid. VDET – Detector for vertical polarization. HDET – Detector for horizontal polarization.

5.3 The Martin-Puplett interferometer

The actual interferometer setup used for the synchrotron radiation measurements is very similar to the basic layout presented in Fig. 3.1. The main difference is the presence of a 90° off-axis parabolic mirror that collects the elliptically polarized radiation behind the beam divider and focuses it onto the detectors (Fig. 5.6). The analyzer grid is placed at an angle of 45° relative to the horizontal plane, and its wires are oriented in a way that detector VDET – below the grid – measures the vertically polarized component whereas HDET – behind the grid as seen from the paraboloid – measures the horizontal component.

In the following, a brief summary of the characteristics of the optical components used in the interferometer is given. Where applicable, spectral limitations arising from the specific properties of these components are pointed out.

5.3.1 Flat mirrors

The mirrors of the interferometer as well as those used in the beam transport line have polished aluminum surfaces. According to [Spa79], the plasma frequency of this material is $3.55{\cdot}10^{15}$ Hz, which corresponds to a wavelength of about 85 nm. All waves with frequencies much lower than the plasma frequency are almost completely reflected at the metal, with the electric field penetrating the surface only by a very short distance. Hence for light in the infrared or far infrared regime with substantially longer wavelengths of micro- or millimeters, absorption and transmission are negligible.

A surface is commonly regarded as a good reflector if its roughness, i.e. the peak-to-peak distance of the fine valleys and ridges on the surface, is below $^1/_{10}$ of the wavelength. As polished metal surfaces have a roughness of about one micrometer or below, the mirrors of the interferometer and of the transfer line can be regarded as perfect reflectors for wavelengths down to at least 10 µm, which corresponds to a frequency of 30 THz.

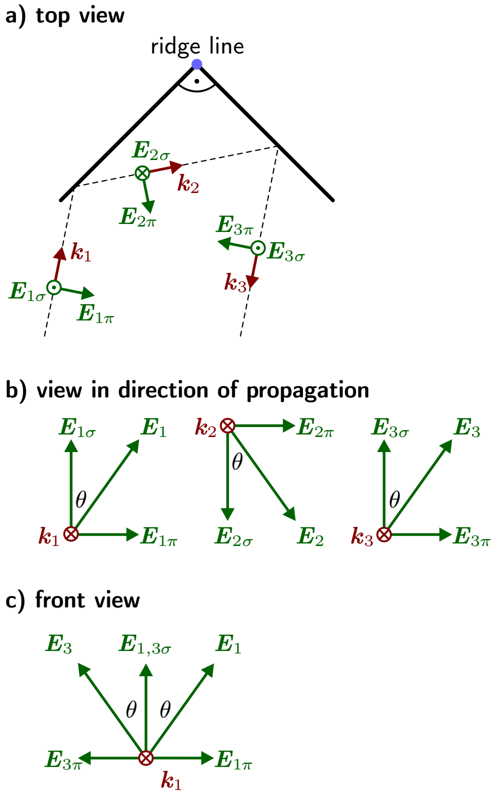

Figure 5.7: Functional principle of a roof mirror.
a) Top view. The electric field component perpendicular to the plane of incidence ($\boldsymbol{E}_{n\sigma}$) is inverted twice.
b) View in the direction of the single wave vectors. In this frame of reference, the polarization state is restored after the second reflection.
c) Front view. In the fixed reference frame of the roof mirror, the field component parallel to the plane of incidence ($\boldsymbol{E}_{n\pi}$) is inverted by the double-reflection.

5.3.2 Roof mirrors

A roof mirror consists of two flat mirrors which are joined at one side under an angle of 90°. The junction is referred to as the ridge line. An incident ray of light is reflected at each of the two surfaces, leaving the mirror parallel to its direction of incidence (Fig. 5.7a).

If the incident plane wave is linearly polarized, its electric field $\boldsymbol{E}_1$ can be split in two components, one parallel to the plane of incidence ($\boldsymbol{E}_{1\pi}$), and one perpendicular to it ($\boldsymbol{E}_{1\sigma}$). This way of decomposition implies that the latter component lies in the reflector plane, where no electric field can be sustained. Hence, in the case of total reflection at a metal surface, the perpendicular component $\boldsymbol{E}_{2\sigma}$ of the reflected field must be found by inversion of $\boldsymbol{E}_{1\sigma}$:

$$\boldsymbol{E}_{2\sigma} = -\boldsymbol{E}_{1\sigma}$$

As this effect is repeated in the second reflection, we see that the σ-component of the outgoing wave is the same as that of the incident wave, $\boldsymbol{E}_{3\sigma} = \boldsymbol{E}_{1\sigma}$.

From Fig. 5.7a, it becomes clear that the parallel component of the electric field is rotated by 180° in the two successive reflections, so that $\boldsymbol{E}_{3\pi} = -\boldsymbol{E}_{1\pi}$. This means that the plane of polarization of the incident wave is mirrored at a plane given by the initial wave vector $\boldsymbol{k}_1$ and the ridge line (Fig. 5.7c).

However, if we observe the electric field in a frame of reference that is attached to the respective wave vector – if

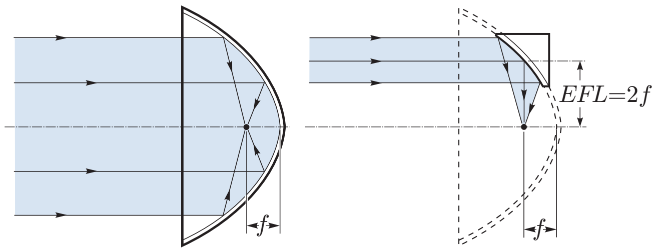

Figure 5.8: Effective focal length (*EFL*) of an off-axis parabolic mirror (drawing from [Ori04])

we look “in the direction of the beam” –, the polarization of the incident wave is found to be the same as that of the outgoing wave (Fig. 5.7b). In this sense, the function of a roof mirror can be described as changing the direction of a wave by 180° while preserving its polarization state.

5.3.3 Parabolic mirrors

In infrared applications, quasi-optical lenses made of low-loss materials like polyethylene, polypropylene or Teflon are frequently used for the purpose of focusing parallel beams or for parallelizing light from a point source. Parabolic mirrors have certain advantages over these diffractive elements that make them indispensible especially for the use with far-infrared radiation. Firstly, the very good reflectivity of polished metal surfaces avoids absorption losses that inevitably occur in any lens material. Secondly, chromatic aberration does not appear, so the focal point is the same for light of all wavelengths.

For practical reasons, it is often desirable to have an off-axis focus. To accomplish this, an outer section of a full paraboloid can be used. A setup as shown on the right side of Fig. 5.8 is called a 90° off-axis parabolic mirror. Its effective focal length is twice the focal length of the full paraboloid [Ori04].

5.3.4 Wire grids

For Michelson interferometers it is customary to use some kind of semitransparent dielectric foil as a beam divider. Although instruments of the Martin-Puplett type are sometimes set up in a similar way with polarizing foils, they are found to be strongly bandwidth-limited by the frequency dependence of the optical properties of the specific material.

For far-infrared spectroscopy, an effective polarizer can be made from an array of closely spaced parallel metallic wires, a so-called *wire grid*. Any incident electric field can be divided into one component parallel and one perpendicular to the wires. The parallel component induces a counteracting current in the metal and is thus reflected, whereas the normal component can pass the grid with little attenuation. If the thickness d of the wires and the spacing s (from center to center) are small compared to the wavelength of the incident light, the moduli of the reflection coefficients for the electric field components parallel and perpendicular to the wires can be calculated as follows [Les90]:

$$|r_{\parallel}| = \left[1 + \left(\frac{2s}{\lambda}\right)^2 \ln\left(\frac{s}{\pi d}\right)^2\right]^{-\frac{1}{2}} \tag{5.4}$$

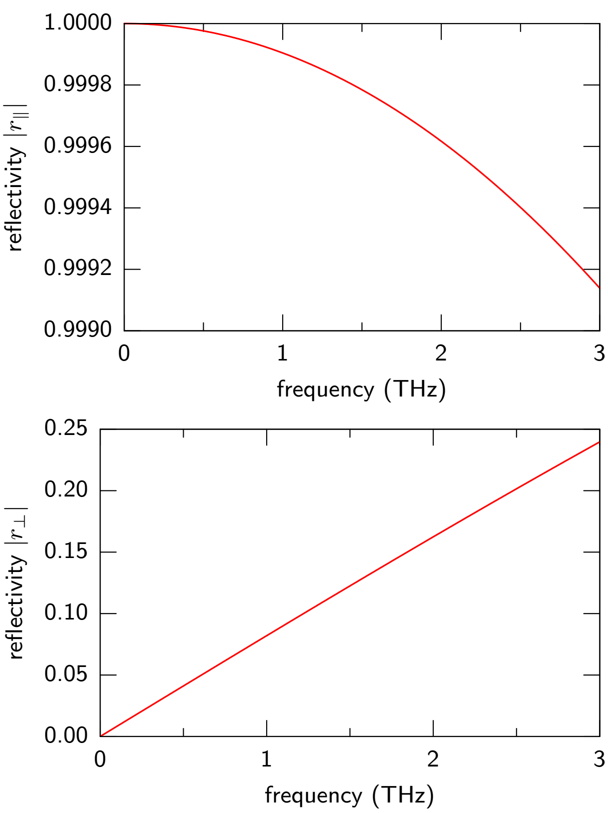

Figure 5.9: Calculated reflectivity for the parallel and normal components of an incident electric field on a wire grid of 15 µm thick perfectly conducting wires with a spacing of 45 µm (center-center). The parallel component is nearly perfectly reflected. For the normal component, the reflectivity of the field increases by about 25% in amplitude towards a frequency of 3 THz.

$$|r_{\perp}| = \left[1 + \frac{(2\lambda s)^2}{\pi^4 d^4}\right]^{-\frac{1}{2}} \tag{5.5}$$

The grids used in the experimental setup consist of 15 µm thick gold-coated tungsten wires placed at a distance of 45 µm. The reflectivity of the electric field for these parameters is plotted in Fig. 5.9 for frequencies up to 3 THz. While the parallel component is reflected nearly perfectly over the whole spectral range, the transmission of the normal component decreases towards higher frequencies; nearly 25% of the electric field are reflected at 3 THz, equivalent to about five percent of the radiation power of that component.

The upper frequency of 3 THz corresponds to a wavelength of about 100 µm, sufficiently fulfilling the condition $\lambda \gg s, d$. However, for higher frequencies the equations (5.4), (5.5) do not hold anymore. For the purpose of bunch length measurements at the bunch compressor BC2 this spectral range is wide enough, as it will be seen that no significant intensity contribution at frequencies above 2 THz is found anyway. Hence, in this context, the wire grids can be treated as ideal polarizers. A comprehensive treatment of the properties of wire grids for a broad spectral range is found in [Cha80].

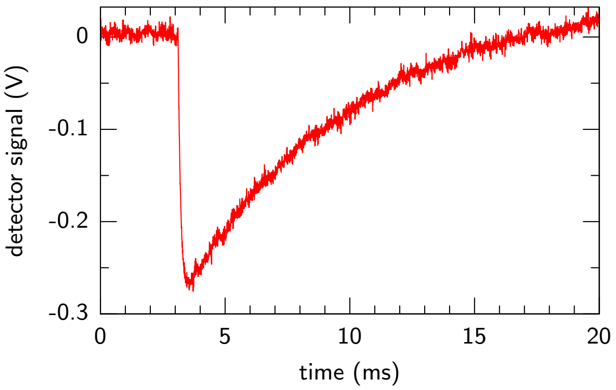

Figure 5.10: Signal shape of a DTGS pyroelectric detector. The rise time is within a few hundred microseconds, the signal decay takes several milliseconds. Hence the detector measures the radiation from a whole macropulse, and single bunches cannot be distinguished. The voltage is negative by convention.

5.4 Detectors

5.4.1 Pyroelectric detectors

All interferometric measurements discussed in this thesis have been done with a pair of DLaTGS detectors (model Bruker GAT202). Their infrared sensitive component is a pyroelectric deuterated triglycine sulphate crystal doped with L-α-alanine. As the crystal diameter is 2 mm, it can be expected that the sensitivity drops sharply for radiation of millimeter and longer wavelengths. The detector window is shielded against visible light by a black polyethylene foil and a few millimeter thick layer of an unknown plastic material of white color.

Ferroelectric crystals are called pyroelectric at a given temperature when their electric dipole moment cannot be changed by applying an external electric field; they often exhibit a change of their spontaneous polarization due to temperature variations [Kit96]. This is the case with DTGS. When the crystal absorbs radiation, it is heated and the resulting change of dipole moment can be measured as a current between two electrodes. As this current balances the spontaneous polarization, it is only of short duration and quickly decays to zero. Hence a pyroelectric detector is sensitive only to temperature *changes*, or in other terms only to radiation of altering intensity, because the absorption of any constant radiation power takes the crystal into thermal equilibrium.

These properties are well suited for the measurement of short pulses of synchrotron radiation. In Fig. 5.10, the response of one of the DTGS detectors mounted in the interferometer is shown for a macropulse of 10 bunches, each carrying a charge of 1 nC, at medium compression in BC2. While the rise time of the signal is within a few hundred microseconds, its decay is mainly determined by the detector electronics and lies in the range of several milliseconds[3]. Hence it is obvious that single bunches within a macropulse cannot be distinguished.

To enlarge the effective active area of the detectors, radiation is collected using metallic cones as laid out in Fig. A.5. Although the cones introduce a strong angular dependence to the detector acceptance, they help to increase the overall signal amplitude and the tolerance against transverse position errors.

5.4.2 Cryogenic bolometer

For the measurement of the transfer function described in section 7.5.1, a cryogenic bolometer built by the Max Planck Institute for Radio Astronomy[4] has been used. Its FIR-sensitive part is an indium antimonide (InSb) crystal cooled by a liquid helium dewar. The operating temperature of 2 K is reached by pumping the helium. Because a filling of helium lasts only for few hours and an outer tank has to be constantly refilled with liquid nitrogen to shield the inner dewar, the handling is quite cumbersome and the instrument is only used when high sensitivity is needed.

The InSb crystal is a semiconductor whose intrinsic conductivity changes as a function of temperature. When a bias voltage is applied across it, the resulting current is a measure for the absolute temperature of the crystal; by cryogenic cooling, the absorption of far-infrared radiation can thus be detected with high precision and low noise. It is clear that the signal decay time is influenced by the quality of the thermal contact to the cooling reservoir. To protect the device from too big heat loads, it is shielded from (short wavelength) infrared radiation by a spectral filter.

---

[3] Other pyrodetectors show a much faster response with decay times of down to 100 ns. However, this advantage is bought at the cost of signal amplitude, as these devices do not integrate over the intensity of a whole bunch train.

[4] Max-Planck-Institut für Radioastronomie, Bonn, Germany

6 Measuring principle and reconstruction process

THE reconstruction of the longitudinal charge density distribution from an interferometric measurement of coherent radiation is a complex process comprising several steps. In this chapter, a detailed overview of the measuring principle is given and typical difficulties are pointed out.

6.1 Detector signals

The signals of the two pyroelectric detectors are sampled with an ADC, triggered by the VUV-FEL macropulse trigger with a frequency of typically 1–10 Hz. For each bunch train, 4096 data samples are taken at a rate of 200 kHz, so one ADC buffer covers a time span of 20.5 ms. Because the rise time of the pyroelectric detectors is small compared to this, a baseline and a peak voltage can be calculated as averages over fixed ranges of the buffer as depicted in Fig. 6.1. The amplitude is then calculated as the difference of baseline and peak voltage. The amplitude value is often simply referred to as the “detector signal”.

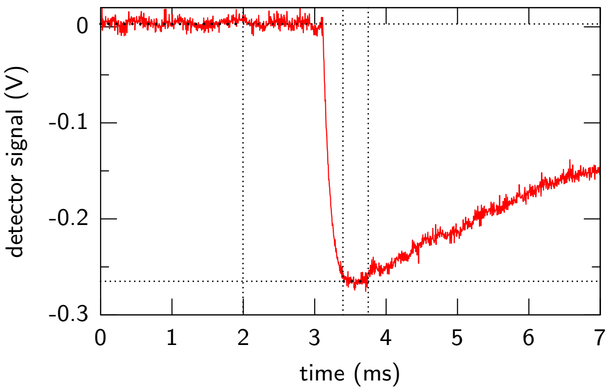

Figure 6.1: Amplitude calculation for a DTGS detector signal. 4096 data samples are taken. The baseline voltage is averaged over the first 400, the peak voltage over 70 samples around the peak of the signal. The amplitude is the difference of baseline and peak voltage.

6.2 Interferograms

In the process of recording an interferogram, the signal amplitudes are measured for a number N_a of consecutive macropulses at each position of the moveable roof mirror. The single data point of the raw interferogram is given by the mean value of these N_a measurements, its error is the corresponding standard deviation. While a higher number of measurements leads to more precise values for the single data points, a whole interferogram scan will take proportionally longer. A typical value is $N_\mathrm{a} = 5$.

The alignment of the interferometer is a critical factor for the magnitude of the signals. Also the electric properties of the readout electronics of each detector are expected to differ slightly. As a consequence, the absolute sensitivities of the two detectors are not equal, as seen in the raw interferogram shown in Fig. 6.2. Hence, to allow a normalization to the total intensity, a correction of the measured voltages is necessary. To determine the correction factor, an average over the signals of the left and right quarter of the interferogram is calculated for each of the two detectors. The correction factor is then simply the ratio of these two values, and the result of its application is an interferogram like the one presented earlier in Fig. 3.2.

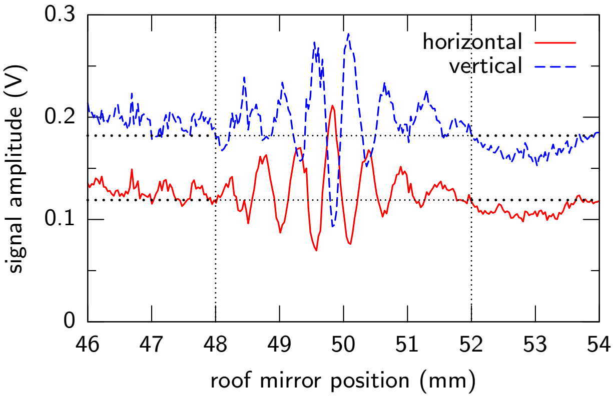

Figure 6.2: Raw interferogram with uncorrected signal amplitudes. The horizontal detector has a smaller sensitivity than the vertical one.

The specific range for averaging – i.e. the two outer quarters of the interferogram – is meant to exclude the center burst[1], where the horizontally and vertically polarized components of the radiation are indeed expected to have different intensities. Obviously, the algorithm fails when the scan range is too small or not properly centered.

If the data have been thus corrected, the normalized difference interferogram $\delta(x)$ can be obtained directly from equation (3.1). The error is calculated using Gaussian error propagation with s_1 and s_2 denoting the standard deviations of the corrected signal amplitudes:

$$\begin{aligned} s_\delta &= \sqrt{\left[\left(\frac{\partial\delta}{\partial U_1}\right) s_1\right]^2 + \left[\left(\frac{\partial\delta}{\partial U_2}\right) s_2\right]^2} \\ &= 2\,\frac{\sqrt{(U_2 s_1)^2 + (U_1 s_2)^2}}{(U_1+U_2)^2} \end{aligned}$$

It is often necessary to specify an interferogram not as a function of the roof mirror position x, but of the corresponding time shift τ that is induced between the two components of the beam. The position x_0 of the center burst is defined by the maximum of the difference interferogram, and the time shift is then calculated as $\tau = 2(x - x_0)/c$.

6.3 Spectra

It has already been pointed out that the difference interferogram is the Fourier cosine transform of the radiation

---

[1] The *center burst* is the central maximum of an interferogram. It is located at the position of zero path difference between the partial beams.

intensity spectrum. Because the cosine transform is inverse to itself, we may in principle obtain the spectrum[2] as

$$I(\omega) = \int_{-\infty}^{\infty} \delta(\tau) \cos(\omega\tau) \, \mathrm{d}\tau \ .$$

However, as only a discrete number N of points is measured over a limited range $[\tau_{\mathrm{min}}, \tau_{\mathrm{max}}]$, this approach has to be modified. We have to replace the continuous transform by a discrete one, and noting that the cosine transform of a real signal is just the real part of the corresponding complex Fourier transform, we get

$$I(\omega_k) = \frac{1}{N} \Re \sum_{n=1}^{N} \delta(\tau_n) \exp(\mathrm{i}\omega_k\tau_n) \ . \qquad (6.1)$$

Because the measuring positions of the moveable roof mirror during an interferometer scan are spaced equidistantially, (6.1) can be computed with common DFT or FFT (Discrete/Fast Fourier Transform) algorithms, yielding $K = N/2$ non-redundant intensity values equally distributed on the interval $[0, \nu_{\mathrm{max}}]$, with the upper frequency limit $\nu_{\mathrm{max}} = N/2/(\tau_{\mathrm{max}} - \tau_{\mathrm{min}})$.

6.3.1 Avoiding spectral artifacts

Asymmetric scan range

The scan range is virtually never exactly symmetric around the center position of the roof mirror. Hence, the interferogram is divided into a one-sided and a double-sided part, the latter extending around the center burst by an equal distance to the left and to the right. The double-sided part would effectively be counted twice in the transformation. To avoid this, it is beforehand multiplied with a ramp that rises linearly from zero to one (Fig. 6.3). The effect can be understood if the ramp is decomposed into a constant part of $1/2$ and a part rising from $-1/2$ to $+1/2$. The constant part serves to compensate the double-counting while the rising part is introduced to avoid a step between the two regions of the interferogram. As it is antisymmetric around the origin, it generates only imaginary Fourier components that are discarded anyway.

Apodization

Some further precautions have to be taken in order to avoid spectral artifacts. For example, the finite extent of the difference interferogram on the τ axis leads to an effect commonly referred to as *leakage*. Because the intensity is sharply cut to zero at the boundaries of the measurement range, some frequency components are errorneously populated. This can be seen if the finite-width interferogram is described as the product of an interferogram of infinite length and a window function that is 1 in the measured range and 0 outside. Because of its rectangular shape, this function is often referred to as the "boxcar" function. In the frequency domain, the product is represented by a convolution. Thus, each frequency component of the interferogram is distributed in the spectrum with a lineshape given by the Fourier transform of the window function.

In Fig. 6.4, a boxcar function of 50 ps width and the corresponding lineshape are shown. Each spectral line has an infinite number of sidelobes; the intensity "leaks" over a broad spectral range. The problem of leakage is addressed by choosing a window function that approaches zero more smoothly towards the outer ends. For all spectra presented in this thesis, a four-term Blackmann-Harris function as parametrized in [Gro84] has been used:

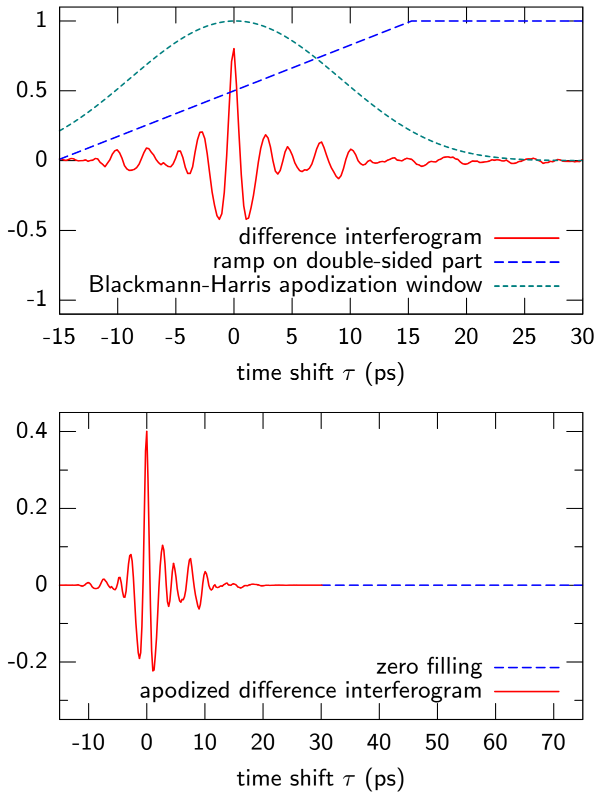

Figure 6.3: Preparation steps for computation of the spectrum. The double-sided part of the difference interferogram is multiplied with a ramp to avoid counting it twice, and apodized with a Blackmann-Harris window to reduce leakage. The result is then padded with zeros to avoid the "picket fence effect".

$$\begin{aligned} BH(\tau) = 0.35875 &+ 0.48829 \cos \frac{\pi\tau}{\tau_{\mathrm{max}}} \\ &+ 0.14128 \cos \frac{2\pi\tau}{\tau_{\mathrm{max}}} + 0.01168 \cos \frac{3\pi\tau}{\tau_{\mathrm{max}}} \end{aligned}$$

Figure 6.4 shows that the sidelobes are completely suppressed – however, at the cost of a significant increase in the width of the main line.

Zero filling

Another common problem of discrete Fourier transforms, the *picket fence effect*, stems from the finite number of output points. As mentioned before, the number K of frequency domain points obtained by a DFT computation of (6.1) amounts to only half the number N of time domain points, $K = N/2$. Because the DFT thus produces samples for fixed frequencies $\nu_k = \nu_{\mathrm{max}} \frac{k}{K}$, it may happen that a spectral line falls directly between two sampling positions – it appears as if seen through a picket fence. Depending on the linewidth, this may introduce a considerable amplitude error.

Relief can be afforded in a simple way by appending $N \cdot (\zeta - 1)$ zeros to the interferogram, which increases the number of points of the spectrum without introducing any

---

[2] Because any information about the absolute radiation power is lost in the normalization step, the spectrum is referred to as a relative quantity and specified in arbitrary units. Thus, constant factors in the Fourier transforms are omitted here.

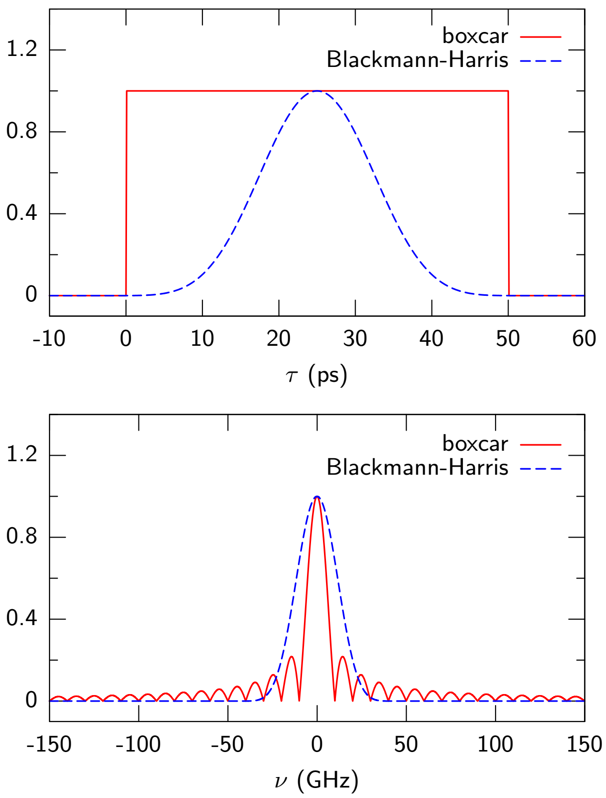

Figure 6.4: Comparison of the performance of the Blackmann-Harris apodization window and the rectangular "boxcar" window for the case of no apodization. All intensities are normalized to one.

error, but of course also without increasing the physical resolution. ζ is called the *zero filling factor*; a value of $\zeta = 4$ has been used in all measurements.

6.3.2 Phase correction

After the difference interferogram has been prepared as described, it is Fourier transformed to the spectrum $\tilde{I}(\nu)$. This spectrum is generally complex because no sample of the interferogram coincides exactly with the position of zero path difference, causing an effective shift in τ and correspondingly a phase rising linearly with ν. As discussed before, the measurement range is never fully symmetric around the zero position, so any phase contributions of the one-sided part are not canceled like those of the double-sided part. Furthermore, the difference interferogram is always slightly asymmetric because of misalignments and measurement errors.

All of this renders a direct application of (6.1) impossible. Instead, the full complex spectrum $\tilde{I}(\nu)$ has to be phase-corrected before discarding the imaginary part:

$$I(\nu_k) = \Re\left[\tilde{I}(\nu_k)\exp(-\mathrm{i}\phi_{\mathrm{corr}}(\nu_k))\right]$$

To obtain the correction phase ϕ_{corr}, the double-sided part of the interferogram is apodized and Fourier transformed separately. $\phi_{\mathrm{corr}}(\nu)$ is the phase of this additional spectrum. Because it has a lower resolution than the full spectrum $\tilde{I}$, the phase is interpolated to the discrete frequency points ν_k.

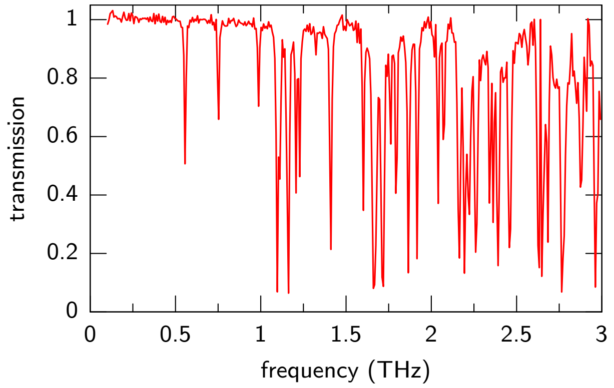

Figure 6.5: Transmission of humid air for an optical path length of 50 cm as calculated from [Jep04]. The relative humidity of the laboratory air is not specified, transmission values higher than one are caused by uncertainties of the measurement.

6.3.3 Transfer function

The spectrum we have obtained is now free from artifacts generated by the Fourier transform itself. Nevertheless, it still contains the accumulated influence of all components of the beamline. The simulated single-particle spectrum already takes into account the effect of the vacuum chamber. As discussed before, the metallic mirrors and wire grids are treated as ideal optical elements and thus any spectral effects caused by them are neglected.

Sources of spectral distortion

Four parts of the optical system remain to be quantified with respect to their spectral influence. The first is the quartz window of the bunch compressor that has already been discussed and whose transmission function can be taken from literature (Fig. 5.3).

The second important part is the gas filling of the beam line itself. Because the optical path length in the transfer line exceeds 11 meters, the measurement is extremely susceptible to absorption by humid air. In the measurement range up to 3 THz, the strong absorption caused by water vapor is critical, as seen by the plot of the measured transmission for an optical path length of 50 cm given in Fig. 6.5. The improvement achievable by nitrogen purging of the instrument has been studied and is summarized in section 7.5.2.

The third item is the sensitivity of the detectors, which must be considered as unknown from the outset, because the manufacturer of the DTGS detectors does not supply any information for the spectral range below 2 THz. As no calibrated far-infrared radiation source was available for measurements, a transfer function for the DTGS detectors is not constructed.

However, the influence of detector responsivity on the measured spectrum may be grave. For example it has been shown for other pyroelectric detectors based on thin $LiTaO_3$ crystals that a strong etalon effect causes periodic zeros in the measured far-infrared spectrum [Ric00]. Figure 6.6 illustrates that no such zeros are discernible in spectra measured with the DTGS detectors. The only points of near-zero intensity in the range up to about 1.5 THz can be attributed to water absorption. Above 1.5 THz, the intensity is so low that only noise remains.

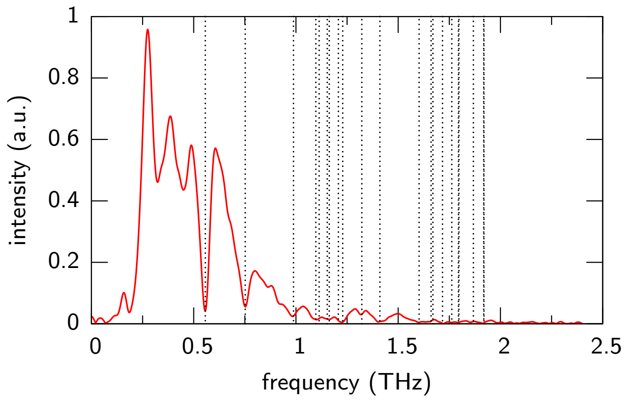

Figure 6.6: Spectrum measured at nearly maximum bunch compression without nitrogen flushing of the infrared transfer line. The vertical lines mark the most important absorption lines of water vapor up to 2 THz.

The fourth factor that may influence the measured spectrum are diffraction losses along the beam transfer line. For millimeter and longer wavelengths, geometric optics is a bad approximation. Hence, the whole system of mirrors and beam pipes including the interferometer components has to be simulated numerically to obtain a transfer function. The matter is presently under investigation, however, the preliminary results are inconclusive. Thus, diffraction effects are not included in the total transfer function.

Correction process

To obtain the transfer function needed to correct a measured spectrum, the single transmission data sets T_i – at the moment this only comprises the transmission T_{water} of humid air and t_{window} of the quartz window – are first interpolated to the frequency points of the spectrum and multiplied:

$$T_{\text{c}}(\nu_k) = \prod_i T_i(\nu_k) = T_{\text{water}}(\nu_k)\,T_{\text{window}}(\nu_k)$$

Afterwards, the combined transmission function has to be convolved with the instrumental lineshape (ILS) of the measurement to adjust it to the same spectral resolution. Because the scan range of the Martin-Puplett interferometer is usually quite small, the resolution of the measurements is considerably lower than that of the transmission function, and the ILS is given by the Fourier transform of the Blackmann-Harris apodization window (cf. Fig. 6.4).

Figure 6.7 shows the combined transfer function before and after the convolution step. As expected, the convolved function $T_{\text{conv}}(\nu_k)$ reveals much broader features than the original $T(\nu_k)$, which also means that the depth of narrow absorption lines is reduced. The spectrum can now be corrected by dividing it by the final transfer function:

$$I_{\text{corr}}(\nu_k) = I(\nu_k)/T_{\text{conv}}(\nu_k) \tag{6.2}$$

6.3.4 Error

Starting with the uncertainty of the difference interferogram $(\delta_n \pm s_{\delta_n})$, the error can be propagated through the calculation steps to obtain the uncertainty of the intensity values of the final spectrum. Recalling the basic definition of the uncorrected spectrum,

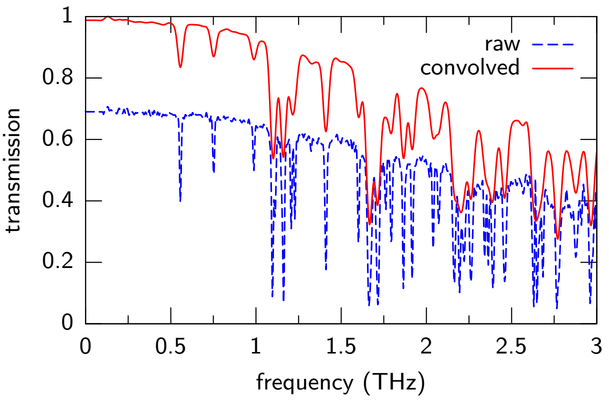

Figure 6.7: Full transfer function before and after convolution with the instrumental lineshape. The ILS used for this plot corresponds to an interferogram width of about 100 ps. Note that the convolved transfer function has been normalized to one to make the two curves more distinguishable.

$$I(\omega_k) = \frac{1}{N}\sum_{n=1}^{N} \delta_n \cos\omega_k\tau_n \ ,$$

the standard deviation $s_I(\omega_k)$ of the intensity values can be calculated using simple error propagation:

$$\begin{aligned} s_I(\omega_k) &= \frac{1}{N}\left[\sum_{n=1}^{N}\left(\frac{\partial I}{\partial \delta_n}\right)^2 s_{\delta_n}^2\right]^{1/2} \\ &= \frac{1}{N}\left[\sum_{n=1}^{N}\cos^2(\omega_k\tau_n)s_{\delta_n}^2\right]^{1/2} \end{aligned} \tag{6.3}$$

The size of the errors s_δ in the difference interferogram is mainly determined by the stability of various accelerator parameters between single macropulses. Thus, we may deem s_δ approximately independent of the time shift τ_n, and simplify (6.3) by replacing s_{δ_n} it with an average value $\bar{s}_\delta$. This leads to the result

$$s_I \approx \frac{\bar{s}_\delta}{N}\left[\sum_{n=1}^{N}\cos^2(\omega_k\tau_n)\right]^{1/2} \approx \frac{\bar{s}_\delta}{\sqrt{2N}} \ .$$

It should be noted that the apodization window $BH(\tau)$ and the ramp $R(\tau)$ covering the doublesided part of the interferogram have to be included in the calculation of the average error of the difference interferogram:

$$\bar{s}_\delta = \frac{1}{N}\sum_{n=1}^{N} s_{\delta_n}\cdot BH(\tau_n)\cdot R(\tau_n)$$

Finally, an error for the corrected spectrum needs to be calculated. The transfer functions for humid air and for the quartz window carry only comparatively small uncertainties, while strong effects on the spectrum are to be expected from diffraction losses and nonlinearities of the detector. Hence, an error of the transfer function cannot be reasonably estimated, and the uncertainty of the corrected spectrum is obtained by dividing by the transfer function:

$$s_{I_{\text{corr}}}(\nu_k) = s_I/T_{\text{conv}}(\nu_k)$$

This definition has the expected effect that the intensity error is bigger where the transfer function is lower, i.e. the error of the spectrum is amplified in the same way as the spectrum itself.

6.4 Form factors

The corrected spectrum now gives a good description of the coherent intensity distribution radiated by the electron bunch. Hence we can use the central formula for coherent radiation effects (2.4) to calculate the form factor, and by neglecting the small incoherent part we get

$$\left|F(\omega)\right| \propto \sqrt{\frac{I_{\mathrm{corr}}(\omega)}{I_1(\omega)}} \ .$$

The equation is given only as a proportionality because the normalization step in the calculation of the difference interferogram makes the amplitude of the measured spectrum arbitrary. It is obvious that a good knowledge of the single-particle spectrum I_1 is required to determine the form factor.

The calculations can not be expected to yield reasonable results in frequency ranges where the measured intensities are close to zero, because neither the division by a transfer function nor by the single-particle intensity are able to restore missing information. For the CSR measurements, this is found to be the case especially at frequencies below 275 GHz due to the cutoff effect of the vacuum chamber. It is hence necessary to find a way of reconstructing the form factor there.

Low-frequency Taylor asymptote

An approach to the problem of finding a suitable low-frequency extrapolation or "asymptote" has been discussed in [Lai97]. Beginning with a Taylor expansion of the longitudinal form factor, we can write

$$\begin{aligned} F(\omega) &= \int \frac{\rho(t)}{Q} \exp(-\mathrm{i}\omega t)\,\mathrm{d}t = \int \frac{\rho(t)}{Q} \sum_{k=0}^{\infty} \frac{(-\mathrm{i}\omega t)^k}{k!}\,\mathrm{d}t \\ &= \sum_{k=0}^{\infty} \left(\frac{(-\mathrm{i})^k}{k!}\omega^k \cdot \int \frac{\rho(t)}{Q} t^k \,\mathrm{d}t \right) = \sum_{k=0}^{\infty} \frac{(-\mathrm{i})^k}{k!}\omega^k \left\langle t^k \right\rangle \\ &= \left\langle t^0 \right\rangle - \mathrm{i}\omega \left\langle t^1 \right\rangle - \frac{1}{2}\omega^2 \left\langle t^2 \right\rangle + \frac{\mathrm{i}}{6}\omega^3 \left\langle t^3 \right\rangle + \dots \ , \end{aligned}$$

with $\left\langle t^k \right\rangle$ denoting the kth moment of the normalized charge distribution $\rho(t)/Q$, i.e. the average value of t^k, weighted by $\rho(t)/Q$. This of course means that the zeroth moment is unity, $\left\langle t^0 \right\rangle = 1$.

Up to second order in ω, the modulus of the form factor can then be expressed as

$$\begin{aligned} \left|F(\omega)\right| &\approx \sqrt{\left(\left\langle t^0 \right\rangle - \frac{1}{2}\omega^2 \left\langle t^2 \right\rangle\right)^2 + \left(\omega \left\langle t^1 \right\rangle\right)^2} \\ &\approx \sqrt{\left\langle t^0 \right\rangle^2 - \omega^2 \left\langle t^0 \right\rangle \left\langle t^2 \right\rangle + \omega^2 \left\langle t^1 \right\rangle^2} \ . \end{aligned}$$

This low-frequency behavior can be simulated by fitting a function of two parameters A and B,

$$F_{\mathrm{Taylor}}(\omega) = \sqrt{A + B\omega^2} \ ,$$

to a reasonable part of the form factor.

Low-frequency Gaussian asymptote

Sometimes better results are obtained by enhancing the form factor at low frequencies. This is accomplished by a Gaussian extrapolation of the form

$$F_{\mathrm{Gaussian}}(\omega) = A \exp\left(-\frac{\omega^2}{2B^2}\right) \ ,$$

which generally yields a steeper increase of the form factor towards $\omega = 0$ than the Taylor type.

High-frequency asymptote

The measured form factor covers the frequency range from zero to an upper frequency $\nu_{\max}$. To avoid a sharp drop to zero at that point, a high-frequency asymptote of the form

$$F_{\mathrm{hf}}(\omega) = A\omega^{-B} \tag{6.4}$$

is attached to the form factor. The exponent B is chosen by hand to approximately match the slope of $|F(\omega)|$; a value of 4 shows satisfactory results. It is usually sufficient to extend the asymptote to twice the frequency range covered by the measured form factor.

Normalization

The physical form factor is subject to the constraint that its zero-frequency component is unity, $F_{\mathrm{abs}}(0) = 1$. Hence, a normalization is necessary after attachment of the appropriate high- and low-frequency asymptotes to the measured form factor. We can write

$$F_{\mathrm{abs}}(\omega) = \frac{|F(\omega)|}{|F(0)|} \ .$$

6.5 Reconstruction of the bunch shape

Now that the absolute value of the form factor is established, the Kramers-Kronig relation (4.16) can be used to calculate the minimal phase $\tilde{\eta}_{\mathrm{r}}(\omega)$. Thus, the complex form factor is obtained:

$$F_{\mathrm{c}}(\omega) = F_{\mathrm{abs}}(\omega) \exp(\mathrm{i}\tilde{\eta}_{\mathrm{r}}(\omega))$$

All information necessary for the reconstruction of the bunch shape has been gathered. However, until now $F_{\mathrm{c}}(\omega)$ is only defined for positive frequencies. Knowing that the complex form factor is the Fourier transform of a real quantity, we can conclude that its imaginary part must be antisymmetric in ω, i.e. $F_{\mathrm{c}}(-\omega) = F_{\mathrm{c}}^*(\omega)$.

After this preparation, we can calculate the bunch shape with a final inverse Fourier transform,

$$\begin{aligned} \tilde{\rho}(t) &= \frac{1}{2\pi} \int_{-\infty}^{\infty} F_{\mathrm{c}}(\omega) \exp(\mathrm{i}\omega t)\,\mathrm{d}\omega \\ &= \frac{1}{2\pi} \int_{0}^{\infty} \left(F_{\mathrm{c}}(\omega) \exp(\mathrm{i}\omega t) + F_{\mathrm{c}}^*(\omega) \exp(-\mathrm{i}\omega t)\right) \mathrm{d}\omega \ . \end{aligned}$$

This way, we obtain a distribution $\tilde{\rho}(t)$ that is normalized to $\int \tilde{\rho}(t)\,\mathrm{d}t = 1$. We can find a discretization of the transform in the same way as we have for the spectrum in (6.1). If the complex form factor is constituted by K samples $F_{\mathrm{c}}(\omega_k)$ corresponding to the equidistant circular frequencies ω_k, with $\omega_0 = 0$ and thus $F_{\mathrm{c}}(\omega_0) = 1$, we get

$$\tilde{\rho}(t_n) = \frac{\Delta\omega}{2\pi} \left(1 + \sum_{k=1}^{K} \big(F_{\mathrm{c}}(\omega_k) \exp(\mathrm{i}\omega_k t) + F_{\mathrm{c}}^*(\omega_k) \exp(-\mathrm{i}\omega_k t)\big) \right) ,$$

with $\Delta\omega$ denoting the step width between the ω_k.

Following this definition, the reconstructed density distribution $\tilde{\rho}(t)$ carries the unit s^{-1}. It would be easy to obtain a current profile of the bunch by multiplying it with the charge, $J(t) = \tilde{\rho}(t)Q$. However, only an unknown fraction of the bunch contributes to the observed coherent radiation. Therefore the reconstructed bunch profiles are given in arbitrary units.

6.5.1 Effectivity of the minimal phase reconstruction

The influence of the asymptotic high- and low-frequency attachments on the reconstructed bunch shape can be examined for an exemplary asymmetric bunch. A simple parametrization is given by

$$\rho(t) = \begin{cases} \exp\left(\dfrac{-t^2}{2{\sigma_0}^2}\right) & \text{for } t < 0 \\ \displaystyle\sum_{n=0}^{N-1} A_n \exp\left(\dfrac{-t^2}{2{\sigma_n}^2}\right) & \text{for } t \geqslant 0 \end{cases} \tag{6.5}$$

with the constraints

$$0 \leqslant A_n \leqslant 1, \quad \sum_{n=0}^{N-1} A_n = 1 \ .$$

On the negative half of the time axis this is just a Gaussian of amplitude 1 and width σ_0, while an arbitrary number N of various Gaussians is added on the positive side in a way that the function has its only maximum at $t = 0$ with $\rho(t) = 1$.

Compared with a parametrization as proposed in [Gel03] for electron bunches having passed a magnetic chicane – a Gaussian peak and an attached exponential decay –, the multi-Gaussian (6.5) is easier to adapt to a desired bunch shape, and it is inherently continuously differentiable.

Influence of the low-frequency asymptote

As an example, the parameter set

$$\sigma_0 = 150\,\text{fs}, \qquad A_0 = 0.3$$
$$\sigma_1 = 600\,\text{fs}, \qquad A_0 = 0.7$$

has been chosen. As depicted in Fig. 6.8, it yields a roughly triangular bunch extending over about 1.5 ps. The form factor of this charge distribution is calculated and attached with the two described types of low-frequency asymptotes (Taylor/Gaussian) at 275 GHz, which is just above the observed onset of the cutoff imposed by the the BC2 vacuum chamber.

Not surprisingly, the Gaussian asymptote reproduces the real form factor much better than the Taylor type. However, the resulting reconstructed bunch shapes are barely distinguishable, with the Gaussian asymptote giving a distribution that is only marginally broader than the one calculated with a low-frequency Taylor extrapolation. In both cases, the agreement with the original bunch shape is quite good except for a small detour below zero in front of the ascending slope of the bunch. As it is also reproduced by reconstruction of the original form factor, this undershoot must be considered an artifact produced by the Kramers-Kronig analysis.

Influence of the high-frequency asymptote

Figure 6.9 compares the reconstruction results for various high-frequency extrapolations. The form factor of the bunch shape specified above is truncated at a frequency of 2 THz, and three exponential high-frequency asymptotes following (6.4) with parameters of $B = 3, 4, 5$ are attached. One curve also represents the continuation with a low positive value[3] above the truncation point. It is obvious that the latter gives the worst result, with a substantial oscillation being visible in the reconstructed charge distribution. This effect is typical for the Fourier transform of any sharply truncated function (cf. section 6.3.1), but also the minimal phase obtained by Kramers-Kronig analysis shows resonance-like behavior around the steep slope of the form factor, as seen in Fig. 6.10.

The other reconstructions fit well to the original bunch shape. In fact, they reproduce the rising edge even better than the reconstructions based on the original high-frequency part of the form factor – i.e. they do not create the small undershoot seen in Fig. 6.8. The reason for this behavior is unclear, but the plot of the minimal phases for the various exponential asymptotes on the right side of Fig. 6.10 shows that the phase of the original form factor is considerably higher than the minimal phases calculated for the others. However, as the difference is mainly an unimportant linear slope corresponding to a translation of the bunch, it can be summarized that the bunch shape reconstruction by Kramers-Kronig analysis is fairly independent of the specific choice of asymptotic extrapolations.

This holds as long as the original form factor is well-behaved in the sense of not including zeros and not showing "exotic" behavior outside the range that is accessible to the measurement. If, for example, a bunch has most of its charge concentrated in a very long tail, the form factor is dominated by a narrow structure at low frequencies. If this structure is suppressed in the emitted spectrum by a low-frequency cutoff, a reasonable reconstruction of the tail is not possible. The maximum length of any feature of the bunch that can be reconstructed amounts to about half the cutoff wavelength. For the CSR measurement at bunch compressor BC2, this is

$$l_\text{max} \approx \frac{1}{2}(275\,\text{GHz})^{-1} \approx 1.8\,\text{ps} \quad \text{or} \quad 550\,\mu\text{m}.$$

On the other hand, the ability to resolve short structures of the charge distribution is limited by the maximum measurable frequency. If we take the strong absorption band of the quartz window (cf. Fig. 5.3) as the limit, we obtain

$$l_\text{min} \approx \frac{1}{2}(3.6\,\text{THz})^{-1} \approx 140\,\text{fs} \quad \text{or} \quad 42\,\mu\text{m}.$$

---

[3] As equation (4.16) for the minimal phase contains the logarithm of the form factor, it must be assured that $|F(\omega)| > 0$.

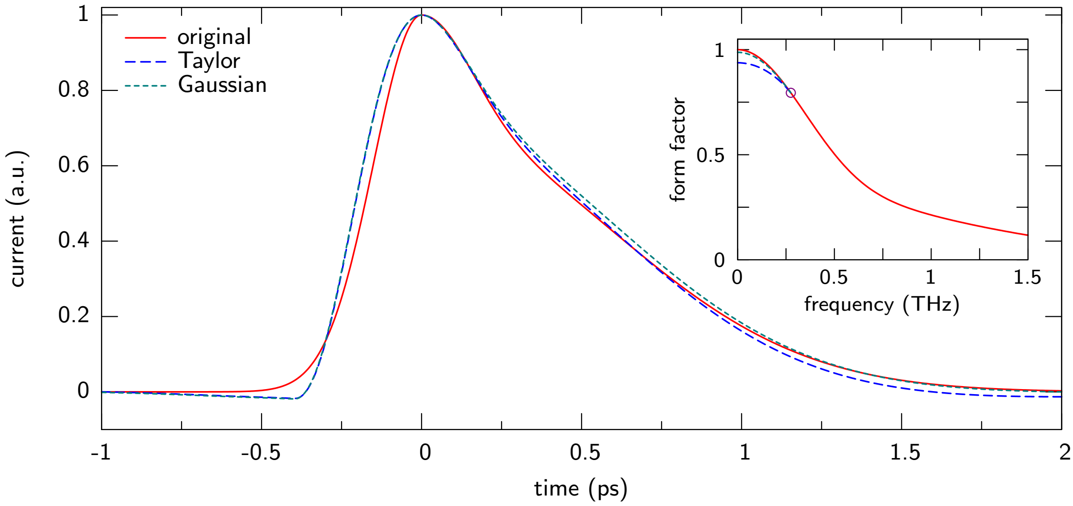

Figure 6.8: Influence of the low-frequency asymptote on the reconstructed bunch shape. The small plot shows the form factor of an exemplary bunch shape with two types of low-frequency asymptotes attached at 275 GHz. The main plot compares the original bunch shape with the reconstructions from the respective form factors.

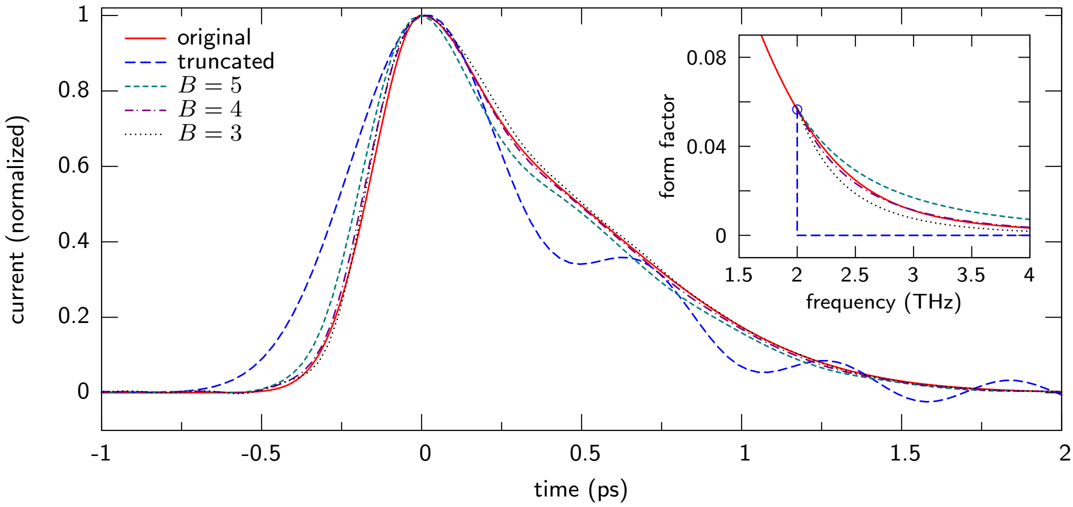

Figure 6.9: Influence of the high-frequency asymptote on the reconstructed bunch shape. The compared high-frequency continuations are a simple truncation to near-zero and three exponential asymptotes based on (6.4) for different values of the parameter B.

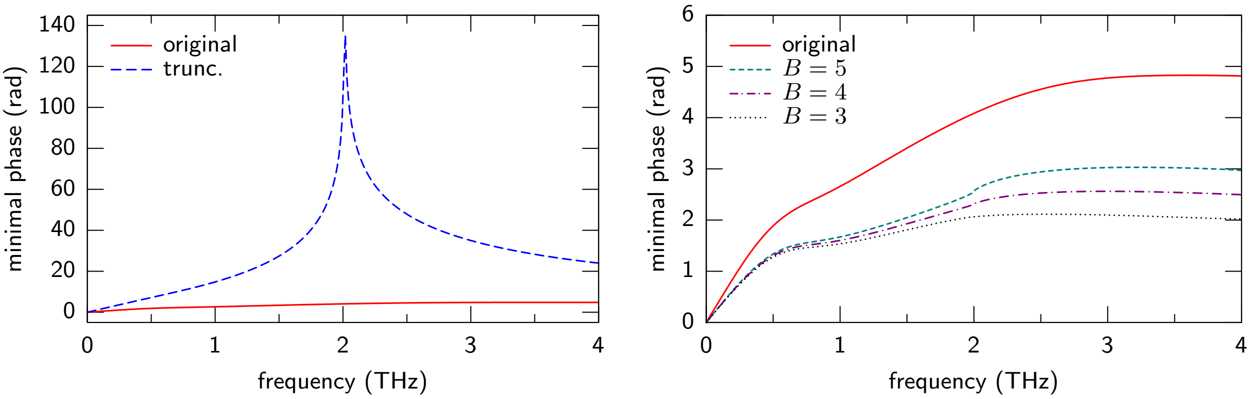

Figure 6.10: Minimal phases for various high-frequency extrapolations of the form factor. The "original" curve shows the phase of the exemplary form factor following the bunch shape given by (6.5). *Left:* If the form factor is truncated and continued with a small constant above 2 THz, the minimal phase shows resonance-like behavior around the truncation frequency. *Right:* High-frequency asymptotes following (6.4) for three values of B are attached to the form factor. The minimal phases are lower than the original phase.

7 Measurements

7.1 Pyroelectric detectors as bunch compression monitors

The interferometric measurement of bunch lengths is quite time-consuming. To obtain a typical interferogram of 512 points with an averaging over 5 samples at a linac repetition rate of 2 Hz, the scan takes at least 21 minutes, not including the time needed to drive the roof mirror into its measuring positions. However, it is not always necessary to measure the coherent spectrum in detail. Important characteristics like the degree of bunch compression can already be determined from the total intensity of the generated radiation.

In this context it is useful to recall the shape of a partially coherent spectrum as shown in Fig. 2.1. If the bunch length is decreased, the width of the form factor in the frequency domain grows. If this is done for a fixed set of other parameters like bending radius, beam energy, charge, the incoherent spectrum stays constant while the coherence regime extends to higher frequencies, thus increasing the integrated radiation power. This effect is commonly used to find the RF phase of the accelerating module that yields maximum compression of the beam.

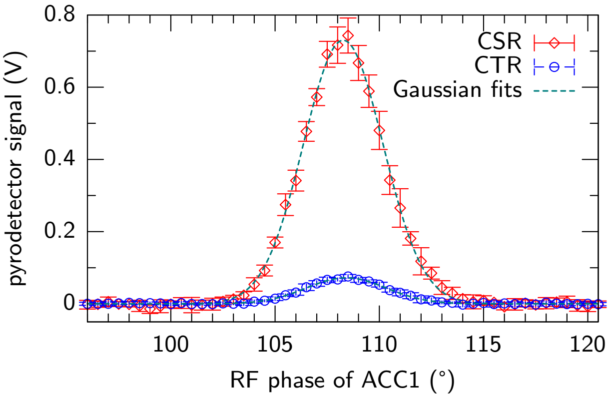

Figure 7.1: Signal amplitudes of pyroelectric detectors as a function of the RF phase of acceleration module ACC1. The measured radiation sources are synchrotron radiation from the last dipole of BC2 (CSR) and transition radiation from a screen downstream of BC2 (CTR). The choice of a Gaussian fit function is purely empirical.

Figure 7.1 shows the result of a scan of the phase of ACC1, for a machine setting in which the on-crest phase of the module had previously been determined to be about 120° by observation of the beam image on an OTR screen in the dispersive section of bunch compressor BC2. During the scan, two different radiation sources have been observed with pyroelectric detectors, transition radiation from a screen nine meters downstream of BC2, and synchrotron radiation from the last dipole of the same bunch compressor (the latter actually measured with one detector of the interferometer). For each phase setpoint, the signal has been averaged over eight successive pulses.

Stepping downwards from higher module phases, the energy slope induced along the bunch grows, and so does the compression caused by the magnetic chicane. At some point the electron packet has reached a state where it produces the most intense coherent radiation; this setting is considered as the phase of maximum compression. If the phase is further decreased, overcompression takes place, and the radiation power diminishes.

Although the absolute amplitude of the voltages cannot be compared, the minimum of the curves yields the same phase of maximum compression for both radiation sources within an accuracy of 0.1°. This emphasizes that the principle of coherent radiation diagnostics is independent of the particular physical radiation process. Because especially pyroelectric detectors are easy to set up and provide a fast qualitative measure of the degree of bunch compression, they have become a standard tool in accelerator diagnostics.

7.1.1 Phase stability

In most of the interferograms that have been recorded, a strong drift of the total radiation intensity over the duration of the measurement has been observed. To investigate the stability of the RF system, a number of consecutive phase scans of module ACC1 have been performed with the CSR detectors. Figure 7.2 shows the measured phase of maximum compression as a function of time. A variation of about 1.5° over a period of 35 minutes is discernible. The general slope towards lower phases is an artifact resulting from a continuous increase of the bunch charge that has been carried out in parallel to the scans. Because the shape of the peaks obtained by the phase scans becomes asymmetric for higher charge, the used Gaussian fit tends to underestimate the position of the minimum.

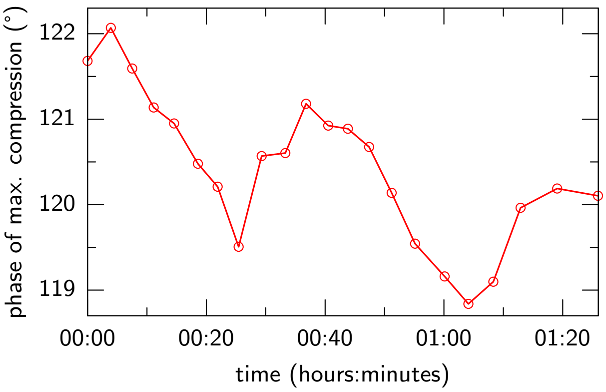

Figure 7.2: Stability of the nominal RF phase of ACC1 that results in maximum compression. A periodicity of about 35 minutes is discernible. The general slope towards lower phases is an artifact from a continuous increase of the bunch charge over the duration of the measurement.

From the phase scan shown in Fig. 7.1 it becomes clear that a fluctuation of 1.5° has a dramatic effect on the coherent radiation intensity, especially if the accelerator is set up for intermediate compression states on the steep signal slope. In this examplary measurement, the detector signal drops by a factor of 2.7 between 110° and 111.5°. At the prevalent pulse repetition rate of 2 Hz, interferometer measurements take at least 30 minutes to achieve sufficient frequency resolution and range, and often longer if special parameter sets are chosen. This means that the interferogram is obtained for a bunch shape that is smeared out because the module phase always covers its complete drift range during the scan. Efforts are made to improve the stability of the RF system.

7.1.2 Charge dependence of the radiation intensity

It has already been stated that the incoherent radiation intensity produced by a relativistic bunch of electrons can be neglected whenever a significant part of the radiation is emitted coherently. The validity of this approximation is confirmed by the fact that the pyroelectric detector signal has vanishing amplitude outside the narrow compression region indicated in Fig. 7.1, regardless of the choice of radiation source (CSR, CTR), bunch charge (up to 3 nC), and number of bunches per macropulse (up to 10). Using (2.4) we may thus write

$$\begin{aligned} P &= \int_0^\infty \frac{\mathrm{d}P_1}{\mathrm{d}\omega} \left(N + N(N-1)\,|F(\omega)|^2\right) \mathrm{d}\omega \\ &\approx \int_0^\infty \frac{\mathrm{d}P_1}{\mathrm{d}\omega} N^2\,|F(\omega)|^2\,\mathrm{d}\omega \end{aligned} \tag{7.1}$$

for the total radiated power, with $\mathrm{d}P_1/\mathrm{d}\omega$ denoting the single-particle spectrum, and N the number of particles. The form factor does not explicitly depend on N, but only on the normalized charge distribution $\rho(t)/Q$. Hence, we expect a quadratic dependence of the radiation power on the number of particles, $P \propto N^2$, if the bunch shape itself is independent of N.

To check the behavior of the form factor in this context, the radiation power generated by the electron bunch has been measured for different bunch charges $Q = Ne_0$. For the measurement depicted in Fig. 7.3, the current of the flashlamp amplifier of the photoinjector laser has been varied in 30 steps to cover a charge range of 0.3 nC to 3.2 nC. For each step, 20 successive readings from one of the interferometer detectors and from a bunch compression monitor (BCM) have been averaged. The BCM is a pyroelectric detector recording the CTR intensity from a transition radiator that is located about 9 m downstream of bunch compressor BC2. The whole procedure has been repeated for different settings of the phase of acceleration module ACC1.

It can be seen that almost all of the measured curves deviate from the ideal $P \propto N^2$ behavior. An especially remarkable fact is that the radiation intensity registered by the interferometer detector does not increase monotoniset ytics 0,0.5,1.5 cally towards high bunch charge. Instead, the curves show a bend at some point and the coherent radiation power begins to decrease. These bends occur at lower charge if the module phase is nearer to the maximum compression phase of 108.3°. The effect is not observed by the BCM at a position further downstream.

A possible explanation for the different behavior is found by considering the radiation source and the cutoff imposed by the surroundings of the beam. While the narrow BC2 vacuum chamber prevents the propagation of light with frequencies below 275 GHz, the transition radiator is placed in a more spacious part of the vacuum tube. Hence, the cutoff frequency for the BCM is lower, interferometer measurements at similar vacuum ports indicate a value of about 50 GHz. This makes an important difference if the coherent radiation power is concentrated mainly in the range of low frequencies, i.e. for bunches with distinct tail sections. A similar effect might be caused by losses in the long radiation transfer line of the interferometer, which is more susceptible to diffraction effects than the BCM that is placed at a distance of less than a meter from the transition radiator. The influence of both the low-frequency cutoff and of diffraction makes the assumption $I \propto P$ invalid, the detector signal is no longer proportional to the radiated power.

It is also possible that the bunch compressor geometry (Fig. A.4) affects the measurement. The interferometer transfer line is designed to collect synchrotron light from the last dipole of BC2. Dispersion is created between the first two dipoles of the bunch compressor, and in the beginning of the field region of the last dipole, the orbit is still dispersive. Hence, the CSR emitted there comes from a bunch that is not fully compressed. The second, possibly more important point is that the vacuum window is placed just in the line of sight of both of the last dipole magnets. Hence it does not only transmit synchrotron radiation from dipole 4 as intended, but also from dipole 3, where the orbit is highly dispersive.

To visualize the deviation of the measurements from the ideal case of a form factor that is independent of the number of particles, the detector signals have been normalized by Q^2. By using $Q = Ne_0$, we can conclude from (7.1) that

$$\frac{P}{Q^2} \propto \int_0^\infty \frac{\mathrm{d}P_1}{\mathrm{d}\omega}\,|F(\omega)|^2\,\mathrm{d}\omega\ ,$$

so we may take this quantity as a relative measure of the bunch length in a way that a bigger absolute value $|P/Q^2|$ is a sign of a bigger integral $\int |F(\omega)|\,\mathrm{d}\omega$, which can only be caused by a bunch that is shorter in the time domain. It should be noted that the quantity that is actually measurable, $|I/Q^2|$, can only approximate $|P/Q^2|$ within the limitations discussed above.

The result of this charge normalization is shown in Fig. 7.4. We see that the description $P \propto Q^2$ fits best for module phases that induce a comparatively small energy slope along the bunch – namely the settings of 112.4° and 114.4°. Especially for the BCM, I/Q^2 is almost constant. However, at the "strongly compressing" phases 108.4° and 110.4°, the radiation power grows almost linearly with charge, which means that the relative bunch length increases for a higher number of particles.

This result is expected and mainly attributable to space charge forces in the gun and the following part of the accelerator where the electron beam has not yet been brought to ultrarelativistic energy. The more charge is extracted from the photocathode, the bigger the energy spread of the bunches, and the more effective we find the compression in the magnetic chicane.

7.2 Polarization of the radiation incident on the interferometer

To verify the calculations from section 5.2.1, the polarization of the incident radiation is measured by rotating the polarizer grid. The moveable roof mirror is in a fixed, far off-centric position so that the polarizations become mixed in the interferometer, and thus each of the detector signals

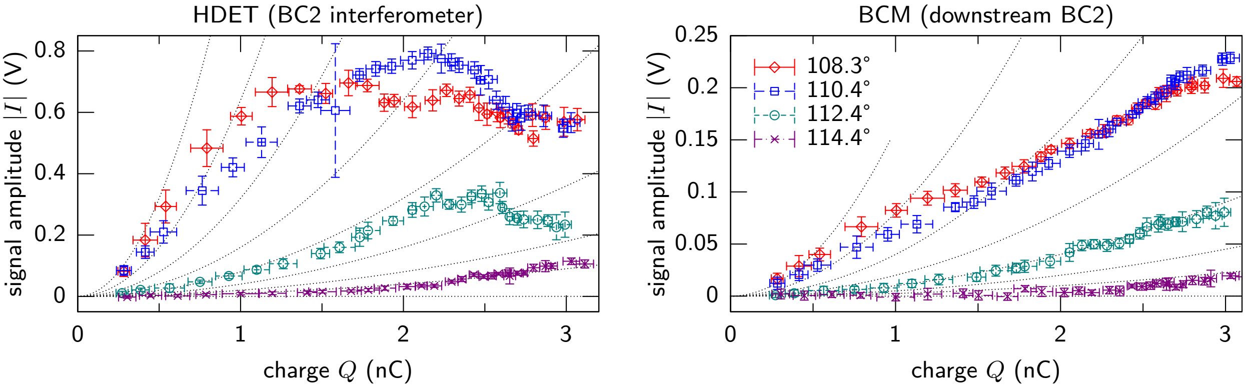

Figure 7.3: Pyroelectric detector signal amplitudes as a function of the bunch charge for different ACC1 phases. The intensities have been measured with one of the DTGS detectors in the interferometer *(left)*, and with a pyrodetector used as BCM downstream of BC2 *(right)*. Maximum compression is reached at 108.3°, on-crest acceleration takes place at about 120°. The dotted lines indicate quadratic dependencies.

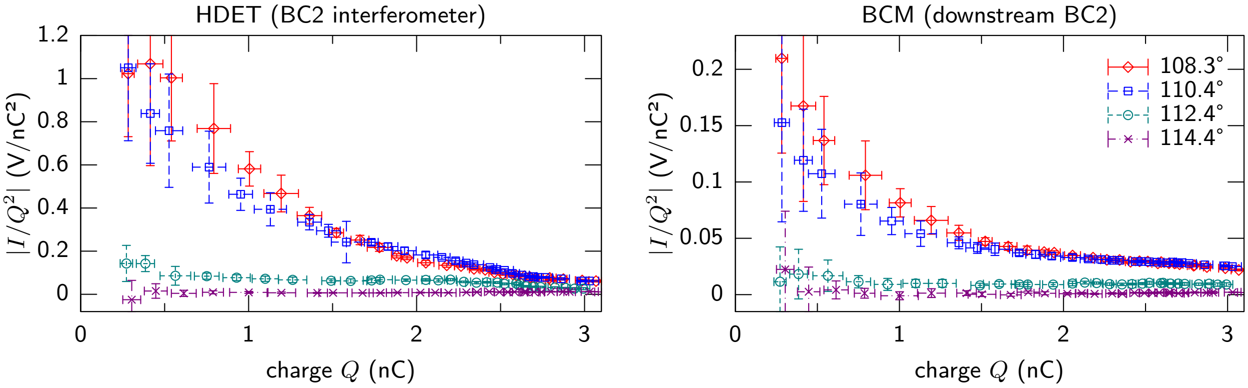

Figure 7.4: Detector signals normalized to the square of the charge. $|I/Q^2|$ has been introduced as a qualitative measure of the degree of bunch compression. It is discernible that the compression is more effective for lower charge.

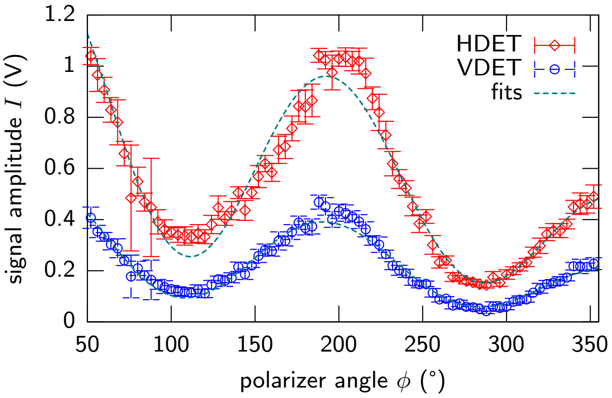

Figure 7.5: Signal amplitudes of the interferometer detectors as a function of the polarizer angle. An angle of zero corresponds to horizontally aligned wires.

is a measure for the remaining total intensity behind the polarizer grid. For each angle ϕ, the detector signals for 8 successive macropulses are averaged. As $\phi = 0$ corresponds to vertically aligned wires, a dependence of $I \propto \cos^2(\phi)$ is expected for the case of complete horizontal polarization of the incident light.

The measured intensities, depicted in Fig. 7.5, clearly show sinusoidal behavior, but there are several deviations from the expected curve. First, an overall slope of the signals is discernible, which can be explained by the phase drift of the acceleration module. The next observation is that the intensity does not reach zero. As we have seen that the imperfections of the wire grids are negligible, this is a clear sign for incomplete polarization of the incident radiation. Hence, the vertical offset of the curves can be used to determine the degree of polarization. It is also discernible that the points of extremal signal amplitude do not coincide with angles that are a multiple of 90°, which means the plane of prevalent polarization in front of the polarizer is not horizontal, but tilted by an angle ϕ_0.

We can now construct a fit function to quantify both ϕ_0 and the ratio of the incident radiation intensities for vertical and horizontal polarization, $p = I_\mathrm{v}/I_\mathrm{h}$. The influence of the drift can be modeled roughly as a linear dependence of the intensity on the polarizer angle, $I_\mathrm{h} = I_0 + I'\phi$. If, furthermore, a correction factor ξ for the angle is introduced, we obtain the function

$$\begin{aligned} I(\phi) &= I_\mathrm{h}\cos^2\left[\xi(\phi+\phi_0)\right] + I_\mathrm{v}\sin^2\left[\xi(\phi+\phi_0)\right] \\ &= (I_0 + I'\phi)\Big(\cos^2\left[\xi(\phi+\phi_0)\right] + p\sin^2\left[\xi(\phi+\phi_0)\right]\Big)\,. \end{aligned} \tag{7.2}$$

Note that with the convention chosen here, the "horizontal" and "vertical" planes corresponding to I_h, I_v actually follow the tilt angle ϕ_0. In other words, I_h, I_v are the respective intensities of the horizontal and vertical polarization component at the vacuum window of the bunch compressor, and not those in front of the polarizer grid.

The parameter values found by a nonlinear least-squares fit of (7.2) to the data are displayed in Tab. 7.1. Although the agreement of the fit curves with the data is not particularly good, the tilt angle of the polarization plane against the horizontal can be determined to $(21 \pm 1)°$. This is in agreement with the value of 18° expected from the nominal bending angle of the bunch compressor as discussed in section 5.2.1. From the values of p, it can easily be calculated that the vertical polarization comprises a fraction of $(17.0 \pm 0.5)\,\%$ of the radiation power.[1] This is an important result as it can be used to validate the simulated single-particle spectrum; corresponding investigations are planned.

	detector VDET	detector HDET
I_0 (V)	0.590 ± 0.012	1.497 ± 0.020
I' (V/°)	-0.001033 ± 0.000046	-0.002750 ± 0.000080
p	0.1963 ± 0.0089	0.2141 ± 0.0055
ξ	1.0255 ± 0.0057	1.0287 ± 0.0045
ϕ_0 (°)	-19.9 ± 1.1	-22.91 ± 0.84

Table 7.1: Fit parameters from (7.2) for the polarization scan from Fig. 7.5

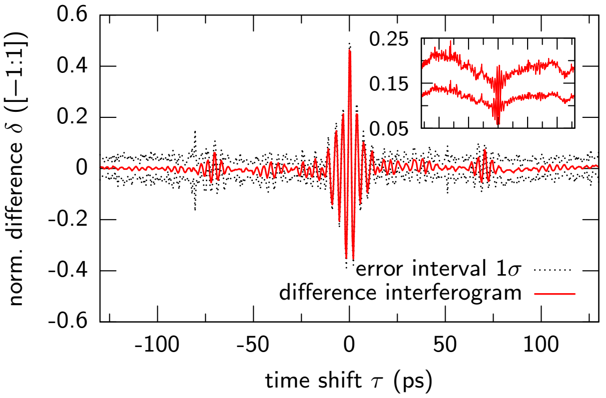

Figure 7.6: Daughter interferograms appear in high-resolution interferometer scans because of double-reflection inside the quartz window. The minor plot shows the raw signal amplitudes in volts on the same time axis as the difference interferogram.

Finally, the parameter ξ indicates a deviation of about 3% between the period length of the measured signal and the angular scale of the polarizer. This might be caused by the bad quality of the fit or by a small error in the calibration of the step motor that rotates the grid.

7.3 Multiple reflections inside the quartz window

When the range of an interferometer scan is chosen sufficiently large, replicas of the central interferogram with smaller amplitude become visible on both sides of the center burst (Fig. 7.6). These so-called "daughter interferograms" are caused by multiple reflections of the radiation inside the quartz window. As illustrated in Fig. 7.7, a part of the beam I_3 does not leave the window towards the transfer line, but is reflected back (I_4). After another reflection at the boundary to the vacuum chamber (I_5), a beam of the reduced intensity I_2 leaves the window in the same direction as the primary beam I_1. Due to the additional optical path in the window material, the second beam is delayed with respect to the first one, and both will interfere when the moveable roof mirror has reached a corresponding distance to its central position.

In principle, higher orders of reflection will lead to the same effect in even further outward positions. However,

---

[1] Following the remarks made before, this is to be understood as the vertical polarization at the vacuum port, not at the interferometer.

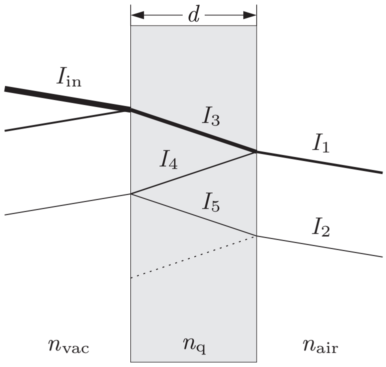

Figure 7.7: Multiple reflections inside the quartz window produce delayed replicas of the initial radiation pulse. n denotes the index of refraction of the corresponding material.

as the amplitude of the interferograms decreases with the number of reflections involved and the scan range of the interferometer is physically limited, only the first daughter interferogram is examined here.

7.3.1 Refractive index of the quartz window

From the measurement shown in Fig. 7.6, it is possible to determine the additional time shift $\Delta\tau$ of the second beam, i.e. the amount of time it takes the reflected beam to traverse the quartz window twice. If we assume perpendicular incidence onto the window, the total optical path length for the rays I_4, I_5 is simply $2n_{\text{q}}d$, with the designations from Fig. 7.7.

Crystalline quartz is birefringent and uniaxial, i.e. incident light is split into an ordinary wave, linearly polarized perpendicular to the plane determined by the direction of propagation and the optical axis of the crystal, and an extraordinary wave, polarized parallel to that plane [Alo96]. The single crystal used in the window is *z-cut* – its optical axis is perpendicular to the surface –, and hence the refractive index for ordinary rays may be taken as n_{q} for all polarizations. Thus we may write

$$\Delta\tau = 2\frac{n_{\text{q}}d}{c} \ .$$

The minima of the daughter interferograms are found at the positions

$$\begin{aligned} \tau_1 &= -\,(70.5 \pm 0.3 \pm 0.7)\ \text{ps} \\ \tau_2 &= +\,(70.5 \pm 0.3 \pm 0.7)\ \text{ps} \ , \end{aligned}$$

where the given uncertainty comprises one half of the step width of the interferogram and a possible systematical error of 1% of the time scale itself.[2]

From the mean time shift $\Delta\tau = (70.5 \pm 0.9)$ ps and the vacuum window thickness[3] $d = (4.80 \pm 0.02)$ mm, it is now possible to calculate the refractive index of the window material:

$$n_{\text{q}} = \frac{c\Delta\tau}{2d} = 2.20 \pm 0.03$$

Comparable measurements of the refractive index of crystalline quartz are found in [Loe73]. From the values specified for room temperature, $\tilde{n}_{\text{q}}(900\,\text{GHz}) = 2.113 \pm 0.001$ and $\tilde{n}_{\text{q}}(0) = 2.112 \pm 0.001$, an average refractive index of $\tilde{n}_{\text{q}} = 2.112 \pm 0.002$ can be estimated for the observed CSR spectrum. Although the literature value is not consistent with the experimental one in the range of two standard deviations, a coarse agreement can be stated. However, it is possible that the thickness of the quartz window deviates more than expected from the nominal value.

7.3.2 Amplitude of the daughter interferogram

Knowing the refractive index of the window, it is also possible to calculate the reflection and transmission coefficients at the interfaces vacuum–quartz and quartz–air. From Fresnel's formulas for perpendicular incidence of light onto a boundary plane between media with the refractive indices n and n', it is known that the electric field amplitudes of the refracted (transmitted) and reflected beam can be calculated as [Jac98]

$$E_{\text{t}} = \left|\frac{2n}{n'+n}\right| E_{\text{in}} \tag{7.3}$$

$$E_{\text{r}} = \left|\frac{n'-n}{n'+n}\right| E_{\text{in}} \ , \tag{7.4}$$

with E_{in} denoting the amplitude of the electric field incident from the side with the refractive index n.

As we are primarily interested in intensitites and not electric fields, we need to calculate the absolute value of the Poynting vector,

$$I = |\boldsymbol{I}| = |\boldsymbol{E} \times \boldsymbol{H}| = EH \ ,$$

and with $H = E \cdot (n/\mu_{\text{r}}) \cdot \sqrt{\epsilon_0/\mu_0}$, we obtain

$$I = E^2 n \sqrt{\frac{\epsilon_0}{\mu_0}} \ .$$

The relative susceptibility μ_{r} has been set to unity here with regard to the three media vacuum, quartz, and air. The important part of the intensity equation is indeed the occurrence of the refractive index of the corresponding medium. This being established, equations (7.3) and (7.4) can be rephrased for the calculation of intensities:

$$I_{\text{t}} = \frac{n'}{n}\left(\frac{2n}{n'+n}\right)^2 I_{\text{in}} \tag{7.5}$$

$$I_{\text{r}} = \left(\frac{n'-n}{n'+n}\right)^2 I_{\text{in}} \tag{7.6}$$

Using the refractive indices $n_{\text{vac}} = n_{\text{air}} = 1$, $n_{\text{q}} = 2.2$, and following the designations of Fig. 7.7, the resulting relative intensities are

$$\begin{aligned} I_3 &= \frac{n_{\text{q}}}{n_{\text{vac}}}\left(\frac{2n_{\text{vac}}}{n_{\text{vac}}+n_{\text{q}}}\right)^2 I_{\text{in}} = 0.872\, I_{\text{in}} \\ I_1 &= \frac{n_{\text{air}}}{n_{\text{q}}}\left(\frac{2n_{\text{q}}}{n_{\text{q}}+n_{\text{air}}}\right)^2 I_3 = 0.761\, I_{\text{in}} \\ I_4 &= \left(\frac{n_{\text{q}}-n_{\text{air}}}{n_{\text{q}}+n_{\text{air}}}\right)^2 I_3 = 0.111\, I_{\text{in}} \\ I_5 &= \left(\frac{n_{\text{vac}}-n_{\text{q}}}{n_{\text{vac}}+n_{\text{q}}}\right)^2 I_4 = 0.014\, I_{\text{in}} \\ I_2 &= \frac{n_{\text{air}}}{n_{\text{q}}}\left(\frac{2n_{\text{q}}}{n_{\text{q}}+n_{\text{air}}}\right)^2 I_5 = 0.012\, I_{\text{in}} \ . \end{aligned}$$

We see that the primary beam I_1 comprises about three quarters of the incident radiation intensity. The secondary

---

[2] The position scale of the moveable roof mirror has been measured with an uncertainty of 1%. According to the definition $\tau = 2\Delta x/c$, this is also the relative error of the time scale.

[3] As no specifications for the vacuum window are available, the absolute uncertainty of the thickness has been estimated to ±20 µm.

interferogram	abs. amplitude	rel. amplitude
main	0.464 ± 0.027	1.000 ± 0.059
left daughter	0.062 ± 0.038	0.133 ± 0.082
right daughter	0.074 ± 0.017	0.159 ± 0.037

Table 7.2: Absolute and relative amplitudes of the difference interferograms from Fig. 7.6. The absolute amplitude is the maximum value of the difference interferogram, the relative one is normalized by the amplitude of the main interferogram.

beam propagating towards the interferometer, I_2, carries only about $^1/_{60}$ of the power of the primary one.

To compare these results with the amplitudes found in the measured interferogram, the minima of the main difference interferogram and of its two daughters have been compiled in Tab. 7.2; to obtain relative amplitudes, the minimum values and their experimental uncertainties have also been normalized to the amplitude of the main interferogram.

The problem at hand is similar to a misalignment of the interferometer as discussed in section 3.4 in the sense that the two interfering beams have different intensities. Thus it is possible to calculate a "misalignment" parameter

$$\xi = \sqrt{\frac{I_2}{I_1}} \approx 0.13$$

and to use equation (3.6) to calculate the expected relative amplitude of the daughter interferogram. This way, a value of 4.1% is obtained, which is far below the measured mean relative amplitude of 14.6%.

If the reversed way is taken, a difference interferogram amplitude of 0.146 translates into a parameter of $\xi = 0.29$, which means the double-reflected beam should have 8.5% of the intensity of the primary beam. This is inconsistent with the calculated ratio I_2/I_1.

There may be several reasons for the observed deviation. The raw signal amplitudes displayed in Fig. 7.6 show strong intensity drifts. While the positions of maximum intensity approximately coincide with those of the daughter interferograms, the center burst is clearly located in an intensity minimum. Although this could change the observed signal-to-noise ratio, due to the normalization process it cannot affect the amplitude of the difference interferogram.

It is more likely that an overall misalignment of the interferometer – which is apparent from the low amplitude of the difference interferogram – causes a distortion of the measurement. Still, it is not clear why only the primary interferogram would be affected by this.

7.4 Alignment studies

It has already been stated that misalignments of the Martin-Puplett interferometer reduce the amplitude of the difference interferogram and decrease the signal-to-noise ratio. The alignment procedure for a FIR instrument is slightly more complex than for interferometers working in the optical regime.

The main difficulty is that a laser beam cannot be used because the wire grids do not act as beam splitters for optical frequencies. It would be necessary to remove the polarizer and to replace the beam divider and the analyzer grid by beam-splitting foils, which would require that the mounting supports for the wire grids and for the foils ensure an identical alignment. The positioning of the laser itself introduces an additional uncertainty. These problems can be overcome by developing a procedure for the beam-based alignment of the interferometer, i.e. by using the CSR from the bunch compressor for alignment studies.

7.4.1 Transfer line

Before the interferometer itself can be adjusted, it has to be made sure that the synchrotron radiation is properly transported through the beam transfer line (Fig. 5.4). The first alignment can be done with a laser that is set up beside the bunch compressor and targeted at the first parabolic mirror. Afterwards, CSR is used for the fine tuning.

In a first step, a single pyroelectric detector or a camera are mounted in front of the polarizer grid. They are directed towards the incident radiation along the optical axis PG—BDG—MRM of the interferometer. The angles of the transfer line mirrors are now successively varied and optimized for the maximum detector signal or the brightest spot.

The inspection of visible synchrotron light with a camera has some advantages over the use of a far-infrared detector. Because the electron beam describes an arc in the bunch compressor, the radiation is not merely emitted in a cone, but covers a larger angular range in the plane of deflection. This horizontal plane is also the plane of polarization examined in section 5.2.1.

Figure 7.8 shows three images of visible synchrotron light entering the interferometer. The plane of maximum extent of the beam is found to have an angle of 19.6° against the horizontal, which is in good agreement with the calculated value of 18°. The pictures represent three different states of rotation of the paraboloid PM1. This mirror – although sufficient for far-infrared radiation – has a bad optical quality, with visible flutes on the surface. These lines act like a grating for visible light, producing interference patterns in the reflected beam. This effect is actually useful for alignment purposes because the central intensity maximum is clearly separated from outer maxima of higher order, and can thus be identified much easier.

7.4.2 Roof mirror tilt

In the interferometer itself, the only three adjustable components are the two roof mirrors and the paraboloid PM2. A short overview on how to recognize typical misalignments of the roof mirrors is presented in the following.

The only externally accessible means of adjustment of the roof mirrors is a micrometer screw that can be used to tilt the whole mirror upwards or downwards (Fig. A.3, top right), i.e. to change the inclination of the ridge line against the vertical axis. The point of zero excursion of this screw has been chosen to coincide with a horizontally leveled top surface of the mirror. Negative excursions lead to a downward deflection of the reflected beam, positive ones to an upward deflection. The sign convention is opposite to the one used for the position of the moveable roof mirror (Fig. 7.9).

To study the influence of the tilt alignment, a number of difference interferograms have been taken at maximum compression of the electron beam for various values of the excursion χ of the moveable roof mirror. The fixed roof mirror has remained leveled, i.e. at an excursion of zero. Both the scan range and the number of points have been reduced, so that the measurements could be done in quick

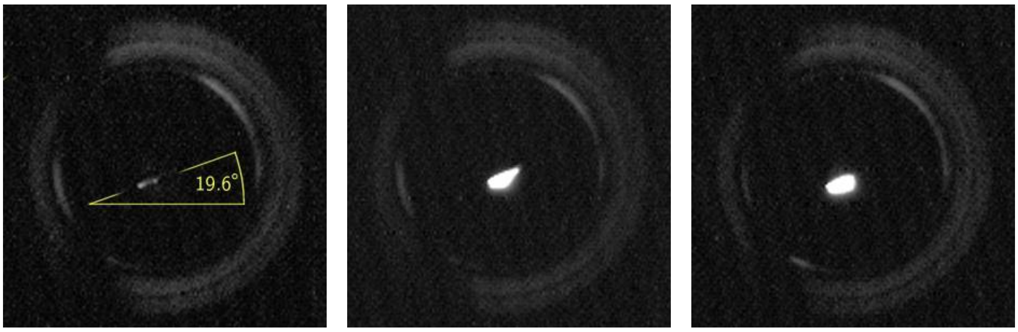

Figure 7.8: Images of visible synchrotron light entering the interferometer. The pictures represent three different rotation states of the parabolic mirror PM1. *Left:* Bad alignment, only a sidelobe of the interference pattern is visible. The plane of maximum extent of the beam is tilted by about 20° against the horizontal. *Middle:* Central intensity maximum with an intensity minimum on the right side. *Right:* Good alignment.

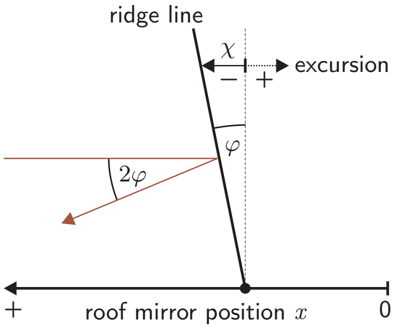

Figure 7.9: Sign conventions for the roof mirror tilt. The excursion of the alignment screw is negative if the mirror is tilted downwards.

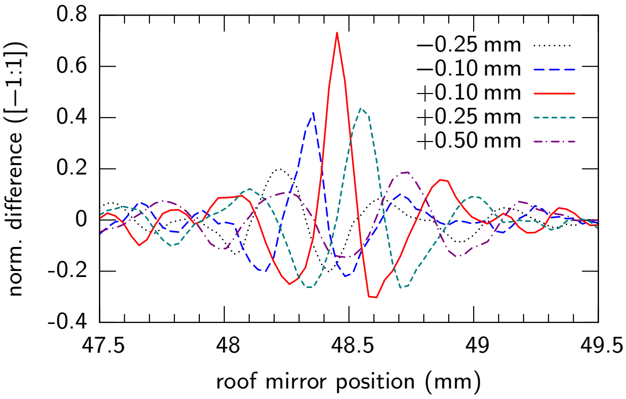

Figure 7.10: Difference interferograms for various tilt states of the moveable roof mirror. The given distance is the excursion of the alignment screw from the central position that corresponds to a horizontally leveled top surface of the mirror. Negative values indicate a tilt downwards, positive values upwards.

succession. Thus all interferograms have been taken within less than an hour, and except for the discussed drifts the comparability of the data is ensured.

A selection of the various difference interferograms is shown in Fig. 7.10. Three properties of the curves are of special interest:

Center burst position

It is noticeable that the position of the center burst changes with the variation of the excursion χ. The reason is that the turning point of the roof mirror is located near its base. Hence, if the adjustment screw is being set to a negative excursion, the upper part of the mirror actually moves towards the incident beam, or away from it for a positive excursion.

Assuming that the beam extends over the whole cross-section of the mirror, the shift of the center burst could be obtained by dividing the beam into vertical slices and averaging the displacements experienced by each of them – however, as the vertical positions of the alignment screw and of the turning point are nearly symmetric around the center of the mirror, the average shift can be approximated as $\chi/2$, which is confirmed by the measurements.

Amplitude

The amplitude of the center burst is the most obvious parameter of a difference interferogram. It depends strongly on the roof mirror tilt. There are two reasons for this: Firstly, if the incoming beam is reflected at the moveable roof mirror under an angle, it acquires a vertical offset relative to the beam reflected at the fixed roof mirror. The size of this offset at the analyzer grid can be estimated with a simple calculation.

The height difference between the alignment screw and the turning point of the mirror is $h = 85\,\text{mm}$, so for the outmost excursion of $\chi = 0.5\,\text{mm}$ we find a tilt angle of

$$\varphi = \arctan(\chi/h) \approx 0.34^\circ\ .$$

A horizontally incident beam is hence deflected by an angle of $2\varphi \approx 0.7^\circ$, and as the optical path length l from the roof mirrors to the parabolic mirror is about 31 cm, the vertical offset accumulated there is found to be $l\tan(2\varphi) \approx 4\,\text{mm}$. Depending on the total size of the radiation spot for a specific wavelength, this offset leads to a reduction of the area of overlap between the two beams, and hence to a decrease of modulation in the interferogram.

The second reason for the diminished amplitude is the reduction of spatial coherence between the beams. After passing the transfer line, the incident radiation constitutes a plane wave in good approximation. While an ideal interferometer would divide this wave front into two waves that are parallel in front of the final parabolic mirror, a tilt of one roof mirror leads to an inclination of one of the wave fronts against the other. This means that the phase relation between the electric fields of both beams is not fixed anymore, but becomes a function of position within the interference region.

The strong dependence of the difference interferogram amplitude on the roof mirror tilt makes it the main parameter for an optimization of the instrument. Additional information can, however, be gained from the asymmetry of the interferogram.

Asymmetry

A close look at Fig. 7.10 reveals that most of the difference interferograms are slightly asymmetric. In a well-aligned instrument, the beam propagates exactly horizontally after reflection at the roof mirrors; otherwise, a vertical offset between the beams at the final parabolic mirror reduces the amplitude of the difference interferogram. If the optical path length is now reduced by a movement of the roof mirror, the vertical offset is reduced, and the modulation of the interferogram is increased. This is in fact observed in the measurements, where nearly all interferograms show a larger amplitude on their left side.

Alignment procedure

From the observed effects, an alignment procedure for the tilts of the two roof mirrors has been developed. The maximum amplitude of the interferogram can be reached for different tilts of the moveable (MRM) and the fixed roof mirror (FRM) as observed in the measurement because the particular positions of zero excursion are not known. A vertical tilt of the central beam divider grid can also introduce different angular errors for the two partial beams.

Additionally, the incident beam might be inclined by an angle ψ relative to the horizontal plane. In this case, the dependence of the vertical beamspot position at the parabolic mirror can only be removed by an equal tilt of the MRM, so setting $\varphi = \psi$ yields the minimum asymmetry.

Summing up, there are two parts to the alignment of the roof mirror tilts: Both must have an equal offset angle ψ to compensate for non-horizontal incidence of the beam, and a certain difference angle $\Delta\varphi$ to compensate for angular errors of the beam divider and of the roof mirrors themselves:

$$\begin{aligned}\varphi_{\mathrm{MRM}} &= \psi \\ \varphi_{\mathrm{FRM}} &= \psi + \Delta\varphi\end{aligned}$$

Taking this into acount, the alignment procedure can be formulated as follows:

1. Align the last mirror of the transfer line to ensure horizontal incidence to the interferometer. This can be done on the basis of visible synchrotron light with a leveled setup of a camera and a horizontal slit screen.
2. Level both roof mirrors, $\varphi_{\mathrm{MRM}} = \varphi_{\mathrm{FRM}} = 0$.
3. Take a series of interferograms, varying the tilt of the MRM around the starting position.
4. Select the interferogram (a) with the biggest amplitude and note the corresponding difference between the excursions of FRM and MRM, $\Delta\varphi = \varphi_{\mathrm{FRM}}(a) - \varphi_{\mathrm{MRM}}(a)$.
5. *If* one of the interferograms (s) is significantly more symmetric than the one with biggest amplitude, note the corresponding excursion of the MRM, $\psi = \varphi_{\mathrm{MRM}}(s)$, set the excursion of the FRM to the sum of this value and the difference from last step, $\varphi_{\mathrm{FRM}} = \psi + \Delta\varphi$, and continue with step 3.
6. Set the MRM to the excursion that it had in the interferogram (a) with maximum amplitude, which should now also be quite symmetric: $\varphi_{\mathrm{MRM}} = \varphi_{\mathrm{MRM}}(a)$.
7. Move the MRM into its exact center burst position.
8. Minimize the signal of the vertical detector by cautiously varying the tilt of the FRM. If necessary, repeat step 7.

Step 1 and 2 only establish a starting point for the procedure, and may hence be omitted if the transfer line is known to be pre-aligned well. The last two steps make use of the fact that incident horizontally polarized light is restored to its initial polarization state after recombination of the partial beams in the interferometer if the path difference is zero. In an ideal instrument, the signal from the vertical detector could thus be reduced to zero in the center burst of the interferogram.

7.5 Transfer function measurements

For a reconstruction of the bunch form factor, the transfer function of the optical system must be known. Some measurements aiming at an improved understanding of the observed spectral behavior are presented in the following sections.

7.5.1 Diffraction losses in the beam transfer line

In order to obtain information about the spectral influence of diffraction losses along the beam transport line, a simple blackbody radiator consisting of a heating plate and a chopper has been set up between the BC2 vacuum chamber window and the first parabolic mirror PM1. Although the (short-wavelength) infrared part of the emitted radiation was easily detectable with a pyroelectric detector at the end of the transfer line, the intensity behind the interferometer was too small to be measured, and therefore no spectrum could be recorded. Even with a cryogenic bolometer of much higher sensitivity, no signal could be established.

Similar measurements with the same bolometer can be found in [Men05]. In that experiment, a small signal could be established at the end of the interferometer, and a quite noisy spectrum was measured. In contrast to the recent measurement, the “blackbody” source was mounted directly in front of the interferometer.

The preliminary conclusion is that the intensity loss for far-infrared radiation due to transfer line effects was grave for the given setup of the transfer line during the measurement. However, the transport efficiency could later be improved by a CSR-based alignment of the transfer mirrors. Further investigations are needed.

7.5.2 Absorption in humid air

As mentioned before, the absorption caused by water vapor has a critical influence on the interferometric measurements which can be reduced by purging the instrument and the beam transfer line with dry nitrogen. Figure 7.11 shows that the relative humidity of the gas filling can be reduced

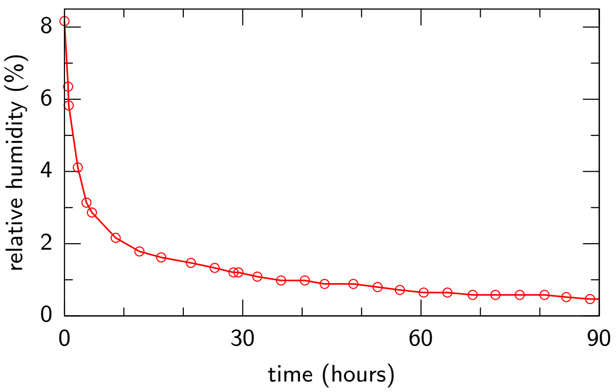

Figure 7.11: Relative atmospheric humidity inside the TOSYLAB beam transfer line during nitrogen purging with a flow of 1 l/s [Gri05a]

to about 0.5% if the maximum possible nitrogen flow of 1 l/s is sustained. However, this is a slow process, and it takes at least two days to make it effective.

Basic considerations

Quantifying the influence of water absorption on the basis of measured spectra is a rather unprecise procedure because it involves several estimates. As a lot of time is needed for a good nitrogen purging of the instrument, no two measurements comparing a dry nitrogen atmosphere with the normal atmosphere under equal external conditions could be taken. For the spectra that can be compared here, it must be expected that several characteristics of the accelerator have changed in the time between the measurements.

During the interferometer runs, the humidity was not determined. Considering that the measurements under nitrogen atmosphere have been taken with a reduced gas flow of about 0.5 l/s and that the instrument had to be opened sporadically for adjustments, the relative humidity can only be roughly estimated as $(1.5 \pm 1.0)\%$. For the relative humidity of the laboratory air, a value of $(50 \pm 10)\%$ is assumed. The ratio of the water concentrations in dry nitrogen and normal laboratory atmosphere is then approximately

$$\frac{C_{\text{humid}}}{C_{\text{dry}}} \approx \frac{50 \pm 10}{1.5 \pm 1.0} \approx 33 \pm 23 \ . \tag{7.7}$$

The reference absorption data for humid air from [Jep04] (cf. Fig. 6.5) are given in the form of absorption coefficients $\alpha_{\text{ref}}(\omega)$. Knowing from *Beer's law* that the absorption coefficient is proportional to the concentration C of the absorber,

$$\alpha(\omega) = C\kappa(\omega) \ ,$$

with the factor $\kappa(\omega)$ being a material constant independent of the concentration, we can calculate the transmission over an optical path of length l by

$$T(\omega) = \exp(-\alpha(\omega)l) = \exp(-\kappa(\omega)Cl) \ . \tag{7.8}$$

As the humidity C_{ref} of the laboratory air is not specified for the reference data set, it cannot be used to determine the transmission for a given water concentration. However, we can define an effective optical path length l_{eff} as the distance a wave would have to travel in air of the reference water concentration to obtain a given transmission T:

$$T_{\text{ref}}(\omega) = \exp(\kappa(\omega)C_{\text{ref}}l_{\text{eff}}) = \exp(\kappa(\omega)Cl) = T(\omega)$$
$$\Rightarrow \quad l_{\text{eff}} = \frac{Cl}{C_{\text{ref}}}$$

Hence, the effective optical path length is proportional to the product of the actual path length l and the actual concentration C.

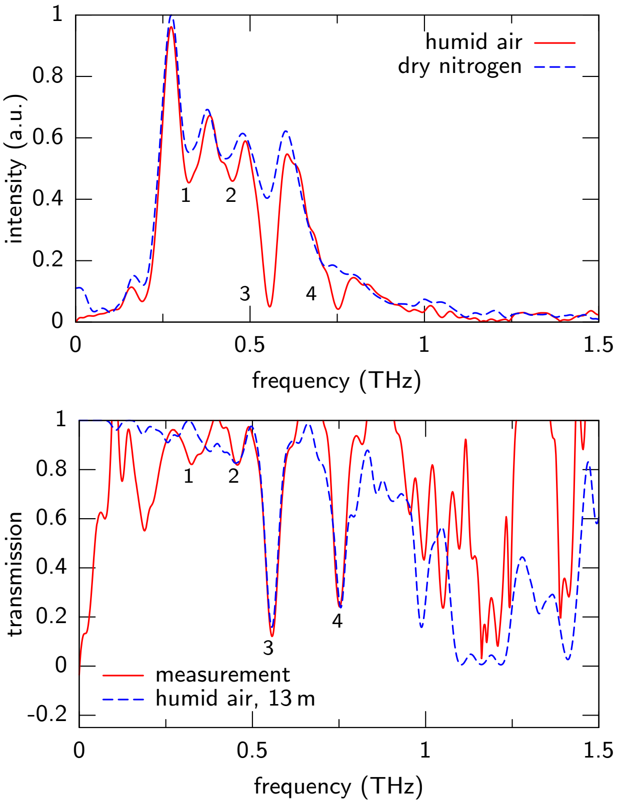

Figure 7.12: *Top:* Comparison of spectra taken with and without nitrogen purging of the interferometer. *Bottom:* Transmission of humid air in the beam transfer line, calculated as the ratio of the two measured spectra. For comparison, the reference transmission for an optical path length of 13 m is shown.

Quantifying the influence of water absorption

To obtain a transmission spectrum, two CSR spectra taken under nearly equal external conditions are compared, one taken after three days of nitrogen flushing, the other two weeks after disabling it. The amplitudes have been adjusted manually to attain a good agreement of the intensity values. On the left side of Fig. 7.12, four major minima are discernible in both spectra in the frequency range from 250 to 900 GHz. Outside this region, the low intensities prevent a detailed analysis. The labeled minima are less pronounced in the spectrum taken with nitrogen purging.

The relative transmission can now be determined by dividing the intensities of the two spectra:

$$T(\omega) = \frac{I_{\text{humid}}(\omega)}{I_{\text{dry}}(\omega)}$$

Now a transmission spectrum is calculated from the reference data using (7.8), with the path length being adjusted to fit the curve to the measured $T(\omega)$ in the regions of the

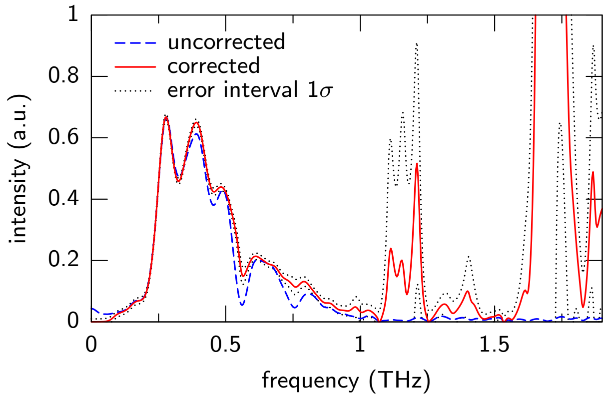

Figure 7.13: A spectrum recorded under humid atmosphere is corrected with the full transfer function. Where the transfer function is near zero as in some regions above 1 THz, the correction process fails.

four labeled intensity minima. The value found for this effective optical path length[4] is $l_{\mathrm{humid-dry}} = (13 \pm 2)\,\mathrm{m}$. Because only two pairs of well-comparable measurements could be found, the reproducibility of this result could only be checked in one other case, where an effective path length of about 13 m also gave the best agreement with the measured transmission; the uncertainty had to be estimated.

The reference transmission spectrum is compared with the measured one on the right side of Fig. 7.12. For the main absorption lines 2, 3, and 4, the agreement between the reference curve and the measurement is good. The remaining dips are only partially caused by water vapor. At the position of minimum 1, the reference data contain no indication of water absorption. Thus, a more thorough investigation of the observed structures is necessary.

If we assume that the two compared spectra differ only in the respective transmission imposed by the water vapor concentrations C_{dry} and C_{humid}, we can write the measured transmission as

$$T(\omega) = \frac{T_{\mathrm{humid}}}{T_{\mathrm{dry}}} = \exp(l\kappa(\omega) \cdot (C_{\mathrm{humid}} - C_{\mathrm{dry}})) \ ,$$

and hence the effective optical path length as

$$l_{\mathrm{humid-dry}} = \frac{C_{\mathrm{humid}} - C_{\mathrm{dry}}}{C_{\mathrm{ref}}} l \ , \tag{7.9}$$

with l denoting the real path length of about 12 m given by the transfer line and interferometer setup. By inserting the concentration ratio (7.7) into (7.9), we find the effective path length for humid and for dry atmosphere,

$$\begin{aligned} l_{\mathrm{dry}} &= \tfrac{1}{32} l_{\mathrm{humid-dry}} &= (0.40 \pm 0.28)\ \mathrm{m} \\ l_{\mathrm{humid}} &= \tfrac{33}{32} l_{\mathrm{humid-dry}} &= (13.40 \pm 2.1)\ \mathrm{m}\ . \end{aligned}$$

These values are used to calculate the transfer function from the reference data for humid air in order to correct measured spectra.

However, it can be seen from Fig. 7.12 that the transmission for humid air drops to almost zero in some regions above 1 THz. Hence, the measured intensities in these regions come from noise, and application of the transfer function leads to a strong amplification of these values and of their uncertainties as shown in Fig. 7.13.

nr.	wavelength (µm)	water line pos. (µm)
1a	927.1 ± 6.1	922.0
1b	856.5 ± 7.0	–
2a	715.9 ± 7.2	–
2b	661.7 ± 9.3	669.2
3	540.5 ± 1.7	538.3
5	482.7 ± 2.3	483.0
6	448.5 ± 4.1	–
4a	423.8 ± 0.9	–
4b	398.9 ± 2.0	398.6

Table 7.3: Positions of reproducible minima in the measured spectra. Where applicable, the central wavelength of the closest major water absorption line is given.

The figure compares a spectrum recorded under humid atmosphere with another one that has been corrected with the full transfer function, including vacuum window effects and water absorption. The described artifacts are visible in the right part of the corrected curve, effectively rendering the measurement useless for the affected frequencies. As there are only small spectral regions without strong water absorption at higher frequencies, it can be summarized that the interferometer has to be purged with nitrogen if a spectral range of more than 1 THz is to be covered.

At lower frequencies, the absorption lines are clearly reduced by application of the transfer function. However, some structures remain that have to be examined in more detail.

7.5.3 Observed spectral structures

Figure 7.14 shows a part of two measured spectra on a wavelength scale. One has been taken with a nitrogen-purged interferometer, the other in the normal humid atmosphere, with different accelerator settings. Nine structures are visible in both spectra at wavelengths above 390 µm. The positions of these minima are reproducible in all measured spectra, regardless of other external parameters like the acceleration phase.

To obtain the positions of the nine minima, four spectra have been chosen under the criterion of good discernability of the structures. The spectra represent various accelerator parameters, and two have been measured under nitrogen atmosphere, two in humid air. The averaged positions of the minima are given in Tab. 7.3 together with the central wavelengths of close major water absorption lines as found in [Pic98].

Five of the observed structures can be explained by water absorption. It appears that the absorption around 922 µm is not included in the reference transmission data because of too coarse sampling. The aforementioned structures labeled as 1, 2, and 4 in Fig. 7.12 are each found to be composed of two sub-minima, of which only one in each case can be attributed to a water line.

The origin of minima 1b, 2a, 6, and 4a is unknown. They are possibly caused by a frequency dependence of the detector or by diffraction losses. Simulations also indicate that interference effects between the synchrotron radiation from the third and fourth dipole of the bunch compressor can cause oscillations in the single-particle spectrum [Gri05]. As the positions of the minima are not equidistant, there is no indication of an etalon effect in the pyroelectric crystal as observed with other detectors (cf. section 6.3.3).

---

[4] The measured $T(\omega)$ represents the transmission for humid air of the concentration $C_{\mathrm{humid}} - C_{\mathrm{dry}}$, hence the index "humid−dry".

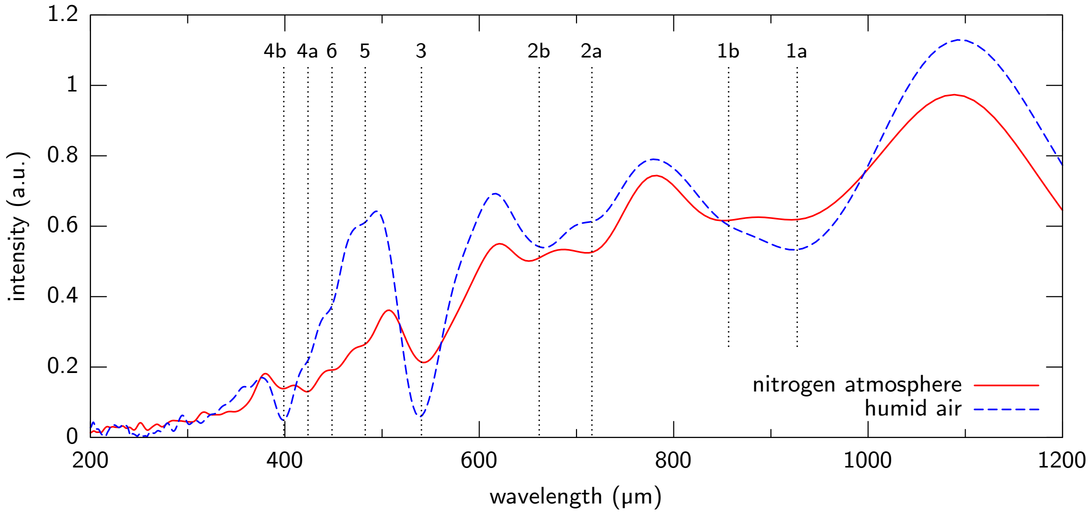

Figure 7.14: CSR spectra for nitrogen atmosphere and humid air on a wavelength scale. A number of structures are reproduced in all spectra that have a sufficient resolution, regardless of external parameters. This plot shows the position of the minima in two exemplary spectra, the intensity scaling is arbitrary.

7.6 Bunch shape reconstruction from a selected measurement

The process of reconstructing the bunch shape from the difference interferogram has been discussed in chapter 6. It is now applied to a selected measurement to obtain a first value for the bunch length. Some difficulties arising with "real" experimental data are also pointed out.

The measurement labeled D0 has been selected under the criteria of good suppression of water absorption by nitrogen flushing, and of both a reasonably high spectral resolution and spectral range. The most important accelerator and scan parameters are found in Tab. A.1 and A.2. The interferogram was recorded while the VUV-FEL produced laser pulses, so the measurement represents a typical setting for the FEL mode of the machine. As the SASE process in the undulator proved to be very sensitive to small variations of the RF phase of acceleration module ACC1, it was necessary to continuously adjust this parameter in small steps in order to compensate for drifts. This way, the phase was kept at approximately 6° above the maximum compression setting, which indicates a relatively weak compression of the bunch in the magnetic chicane BC2.

Signal amplitudes

The raw signal amplitudes in Fig. 7.15 show the fast (shot-to-shot) fluctuations of the CSR intensity as well as the slower drift that has been counteracted manually. The signal amplitude of the vertical detector is considerably smaller than the horizontal one because the former cannot be properly centered below the analyzer grid due to mechanical limitations. However, the amplitude correction step described in section 6.2 is able to overcome this problem, so that the computation of the difference interferogram is possible.

Difference interferogram

From the plot found in Fig. 7.16, we see that the interferogram is slightly asymmetric, with a more distinct modulation towards positive time shifts. This is an indication for non-perpendicular incidence of the radiation to the moveable roof mirror, however, the amplitude of nearly 0.8 shows that the alignment of the instrument is sufficient for further evaluation of the data. The full width at half maximum[5] (FWHM) of the center burst is about 0.51 ps.

Spectrum

The spectrum derived from the difference interferogram is depicted in Fig. 7.17. The measurement was made after several days of nitrogen purging with maximum possible flow, and no influence of water absorption is discernible. Therefore, only the transmission of the quartz window has been included in the transfer function. The given error range clearly shows that the measured intensities mainly constitute noise above 2 THz. The transmission of crystalline quartz drops to nearly zero around 3.85 THz (Fig. 5.3), which creates an artefact in the corrected spectrum. Therefore, the spectrum is truncated at 3.7 THz.

Form factor

At the high-frequency end, an exponential asymptote of the form $A\omega^{-4}$ (cf. (6.4)) is appended to the form factor, while the two discussed types of low-frequency asymptotes – Taylor-type and Gaussian – are fitted to the falling slope between 275 and 325 GHz. The Gaussian curve is steeper, and hence normalizing the zero-frequency value to unity yields an overall higher form factor for the Taylor-type asymptote.

Normally, the simulated single-particle spectrum (cf. Fig. 2.3) is used to calculate the form factor from the spectrum. For comparison, the form factor resulting from use of the single-particle synchrotron radiation spectrum (2.5) is also shown in Fig. 7.18. It can be seen that the former gives a smoother slope at low frequencies.

---

[5] The width is measured at half the amplitude of the maximum, i.e. relative to zero.

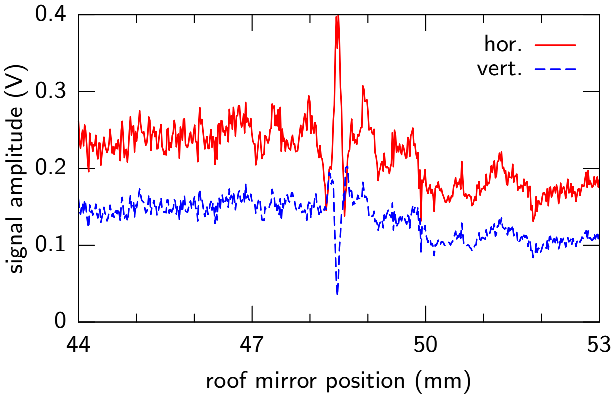

Figure 7.15: Raw signal amplitudes of measurement D0. Fast fluctuations of the radiation intensity are visible.

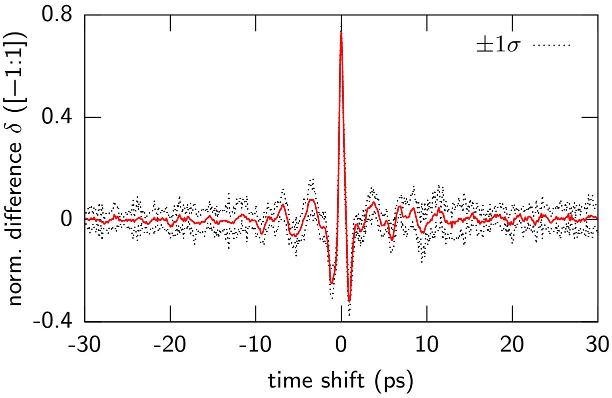

Figure 7.16: Difference interferogram of measurement D0, FWHM 0.51 ps.

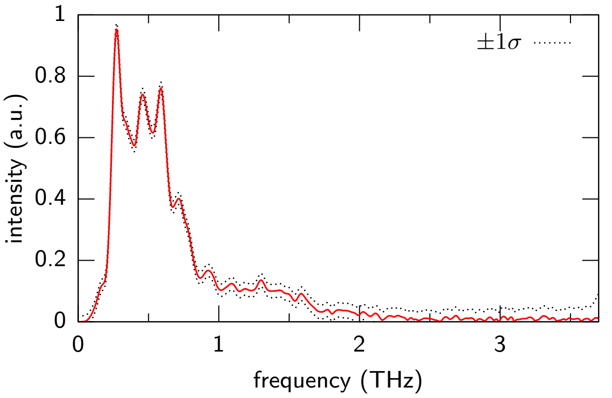

Figure 7.17: Spectrum of measurement D0, corrected with the transfer function of the quartz window.

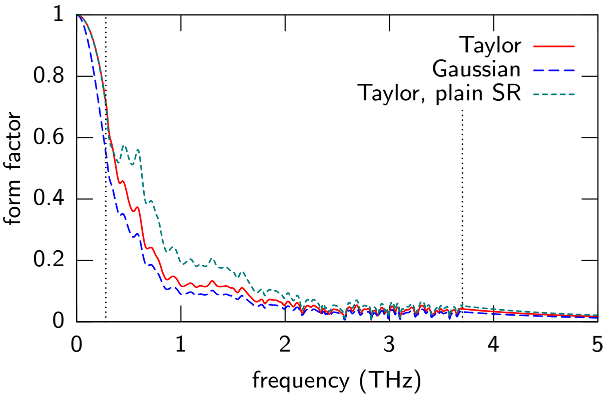

Figure 7.18: Form factor of measurement D0, for various low-frequency asymptotes and single-particle spectra. The low-frequency asymptotes are attached at 275 GHz, the high-frequency asymptotes at 3.7 THz. In the calculation of the first two form factors, the simulated single-particle spectrum from section 2.2.2 was used, and formula (2.5) describing plain synchrotron radiation for the last one.

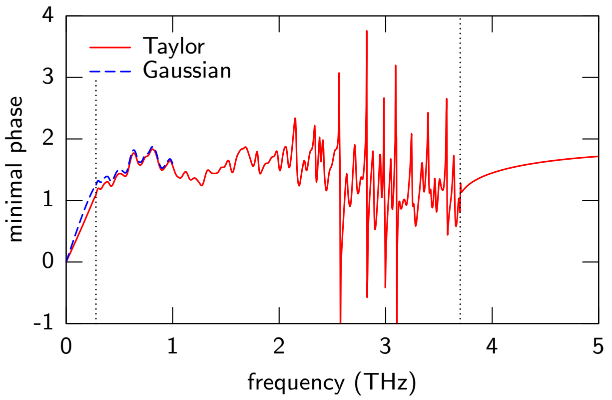

Figure 7.19: Minimal phase of measurement D0. Above 2 THz, where the spectrum is dominated by noise, the minimal phase becomes erratic.

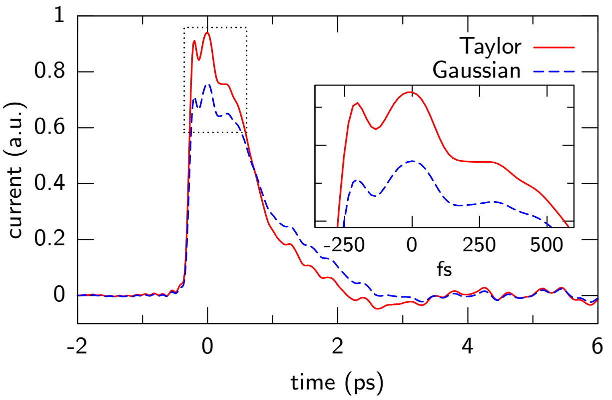

Figure 7.20: Reconstructed bunch shape of measurement D0, FWHM 0.98 ps (Taylor) / 1.11 ps (Gaussian), RMS width 0.63 ps (Taylor) / 0.50 ps (Gaussian).

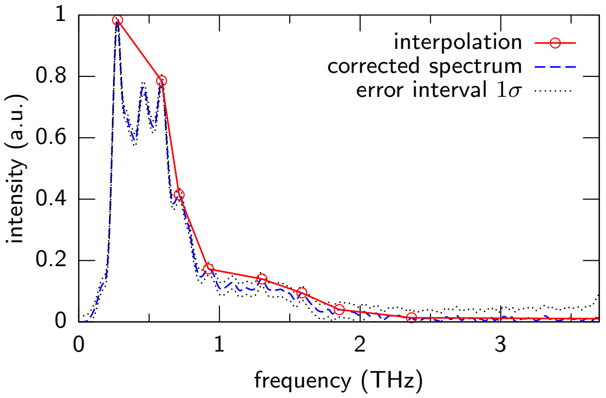

Figure 7.21: Linear interpolation of the spectrum from measurement D0.

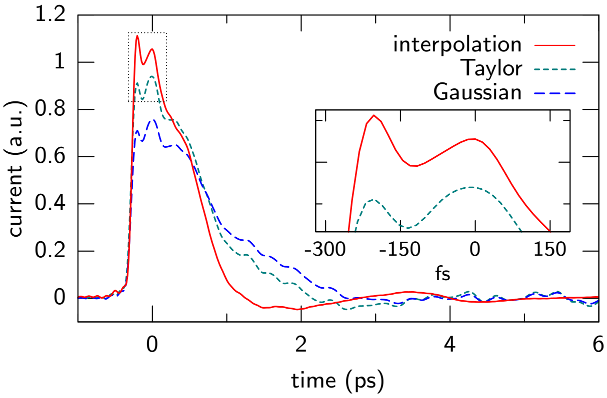

Figure 7.22: Bunch shape reconstructed from the interpolated spectrum of measurement D0, compared with the two reconstructions from the original spectrum. Width of the reconstruction from the interpolated spectrum: 0.82 ps (FWHM) / 0.32 ps (RMS).

Minimal phase

The minimal phases found by Kramers-Kronig analysis are depicted in Fig. 7.19. They differ only slightly at low frequencies. Above 2 THz, where the spectrum is dominated by noise, the minimal phase becomes erratic. However, this is not relevant because the modulus of the form factor is small there.

Bunch shape

Knowledge of the moduli of the form factors and of the minimal phases finally allows the calculation of the bunch shapes, which are shown in Fig. 7.20. The curves have been normalized to an equal integral. They are clearly asymmetric, with a full width at half maximum of about 1 ps. Both the Gaussian and the Taylor-type low-frequency extrapolation yield the same steeply rising front of the bunch, but differ slightly in the length of the tail.

The widths of the distributions are given in the caption of the figure. It should be noted that in the calculation of the root-mean-square (RMS) width,

$$w_{\mathrm{RMS}} = \frac{\int \tilde{\rho}(t)(t-\bar{t})^2\,\mathrm{d}t}{\int \tilde{\rho}(t)\,\mathrm{d}t} \quad , \quad \text{with } \bar{t} = \frac{\int \tilde{\rho}(t) t\,\mathrm{d}t}{\int \tilde{\rho}(t)\,\mathrm{d}t} \quad ,$$

only current values $\tilde{\rho}(t)$ above five percent of the maximum of the respective curve are included to eliminate the influence of trailing over-/undershoots.

On the top of the bunch distribution, two small spikes are discernible. The bigger one has a width of roughly 160 fs, the smaller one of about 60 fs. Considering the maximum frequency of 3.7 THz, the smallest structure length that can be reliably reproduced is about half a wavelength, $0.5/(3.7\,\mathrm{THz}) \approx 140\,\mathrm{fs}$. Thus, the spikes are clearly produced by the upper end of the measured spectrum, and as the measurement is dominated by noise in that range, they should not be interpreted as real features of the current distribution unreservedly.

7.6.1 Linear interpolation of the spectrum

Although the nitrogen purging of the interferometer is quite effective in reducing absorption by water vapor, the measured spectrum still shows numerous unexplained minima.

It has been tried to remove these structures by linear interpolation between selected local maxima of the measured intensity, as depicted in Fig. 7.21. The resulting spectrum is strictly monotonic with the exception of the low-frequency cutoff region below 275 GHz, and its slope just above this frequency is considerably smaller than that of the narrow peak in the original measurement. In turn, the small slope leads to a reduction of the amplitude of the low-frequency asymptotes that are fitted to this spectral range. This effect is strong enough to make the Gaussian- and Taylor-type extrapolation virtually indistinguishable, and consequently they result in the same bunch shape, which is compared with the two reconstructions from the original, non-interpolated spectrum on the right side of the same figure.

As expected, the obtained current profile (Fig. 7.22) is smoother than the original profiles. However, the general bunch shape is quite similar, with the most important difference that the tail of the distribution is almost completely suppressed, resulting in a smaller width of 0.82 ps (FWHM) or 0.32 ps (RMS). As a rule, a higher slope in the fit range for the low-frequency asymptote makes the reconstructed bunch broader and increases the dependence on the particular type (Gaussian or Taylor). The uncertainty about long features of the current distribution is a general limitation of the interferometric method, and can only be partly overcome by measuring coherent radiation from a different part of the vacuum chamber with a lower cutoff frequency.

The leading spike at the front end of the bunch is found to be more distinct than in the original curves. This is clearly a consequence of the almost constant, if small, artificial intensity contributions at high frequencies, which replace the noise seen in the measured spectra.

7.7 Various degrees of bunch compression

The degree of compression in the magnetic chicane is mainly determined by the RF phase in the acceleration module. A phase scan like the one depicted in Fig. 7.1 shows that only a narrow range of at most ±6° around the phase of maximum compression is accessible for radiation measurements with pyroelectric detectors. The range becomes even narrower if the accelerator is operated with only one bunch per macropulse (i.e. in “single-bunch mode”), as the radiation intensity scales linearly with the number of bunches.

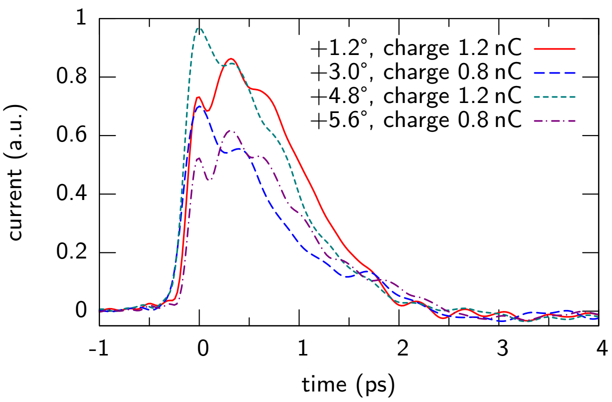

Figure 7.25: Measurements D1–D4, reconstructed bunch shapes.

7.7.1 Measurements with unstabilized phase

The measurements D1–D4, taken under nitrogen atmosphere, represent four settings of the phase of ACC1. Because the interferograms were recorded on two consecutive days, some parameters of the accelerator are not the same for all of them (cf. Tab. A.1). Most importantly, the charge varied from 0.8 to 1.1 nC. However, considering the charge dependence in Fig. 7.3, a qualitative comparison of the measurements is possible. The phase drift in ACC1 was not compensated.

Figure 7.23 shows that the difference interferograms are quite similar. There is a slight change in the width of the center burst, however it is neither correlated with the phase nor with the bunch charge. Only a small variation is discernible in the oscillatory behavior outside the center burst.

The resulting spectra – depicted in Fig. 7.24 – have been corrected with the full transfer function including quartz window effects and residual water absorption. For the main plot, the curves have been normalized to an equal integral. Although changes in the spectra are visible, they do not follow a recognizable pattern. The spectrum with the highest degree of compression (+1.2°) has the smallest fraction of intensity at high frequencies while the +3.0° curve has the highest one, with a significant contribution between 1.5 and 2 THz.

The spectra are easier to distinguish if they are scaled corresponding to the measured intensity. For this purpose, an average over the sum of the signal amplitudes is calculated for each measurement. The values thus obtained are a measure for the mean total intensity incident on both detectors during an interferometer scan. To make the results comparable between different measurements, they are divided by the number of bunches per macropulse, yielding the mean signals per bunch specified in Fig. 7.24. The normalized intensities are now multiplied with these numbers, giving the spectra shown in the minor plot of the same figure.

As expected, the intensity grows with higher bunch compression. However, this increase is not accompanied by a shift to the high frequency range as would be the case if the coherently radiating part of the bunch became shorter. Instead, the spectral distribution stays roughly constant.

From this observation, it is not surprising that also the reconstructed bunch shapes show little dependence on the phase, as seen in Fig. 7.25. The bunch lengths are compared with the ones obtained for the previously examined measurement in Tab. A.3, allowing the conclusion that the coherently radiating part of the bunch is always roughly one picosecond long, provided both the single-particle spectrum and the transfer function are approximately correct.

7.7.2 Measurements with stabilized phase

As mentioned before, it has been observed that the slow drift of the RF phase in ACC1 needs to be compensated to sustain the FEL process. In order to keep the compression in BC2 constant, a feedback software has been developed to adjust the phase setpoint of the module. It monitors the intensity of coherent diffraction radiation generated by the electron beam passing a slit screen a few meters downstream of the bunch compressor. If the measured intensity is higher than a preselected target value, the phase setpoint is increased, or decreased if the intensity is lower. This way, the CSR intensity observed with the detectors in the interferometer is stabilized, too.

The four interferograms H1–H4 have been recorded with different target intensities of the feedback (cf. Tab. A.1). By comparison with a preceding phase scan, it is possible to estimate the corresponding phases relative to the point of maximum compression. Due to time constraints, it has not been possible to perform nitrogen purging before the measurements.

The obtained spectra are displayed in Fig. 7.26. In the major plot, showing the curves normalized to an equal integral, they are barely distinguishable, with the exception of the +3° spectrum, which has a slightly higher contribution of low frequencies than the others. However, for this phase the intensity measured at the diffraction radiator was already so low that the feedback was barely able to stabilize the compression. As technical problems prevented to increase the number of bunches per macropulse, it was not possible to investigate the behavior at lower degrees of compression.

The measurements confirm the preceding analysis that the shape of the spectrum is barely changed by variations of the RF phase within a narrow range around the point of maximum compression. As shown in the minor plot, if the compression is increased, all frequencies of the spectrum are equally amplified. This is an indication that the shape of the "active" part of the bunch – i.e. the part that contributes to the observed coherent radiation – is invariant under variations of the phase in the compression region. The increase in intensity is caused by an increased population of this active part by the electrons of the bunch.

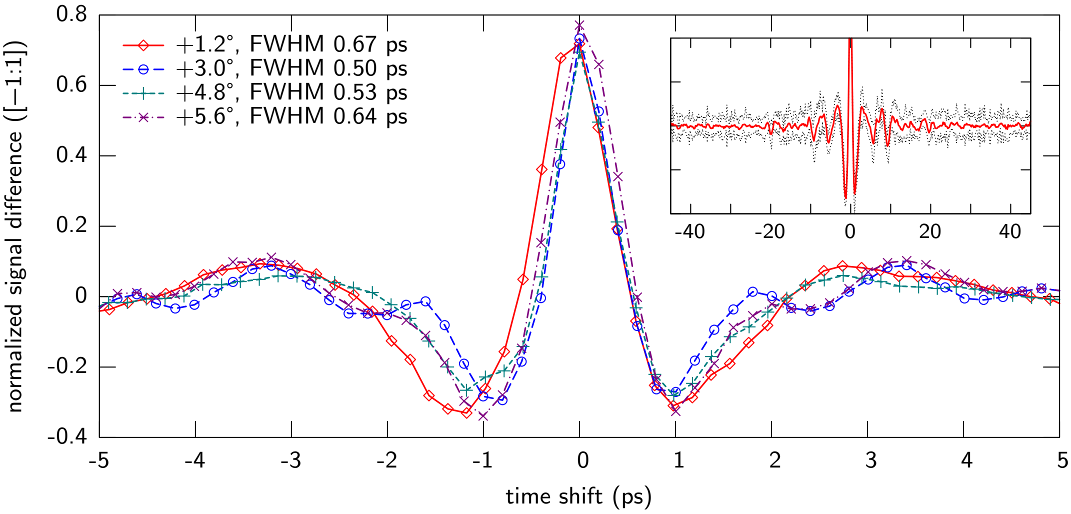

Figure 7.23: Measurements D1–D4, difference interferograms. The phases are relative to the respective points of maximum compression as found by phase scans of the acceleration module ACC1. The minor plot shows the full interferogram with statistical error for a phase of +1.2°.

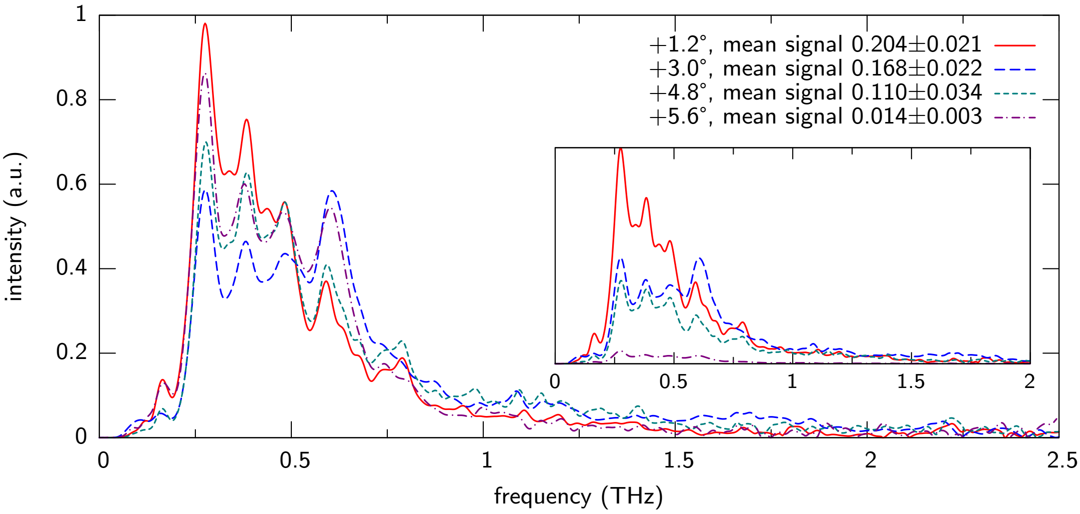

Figure 7.24: Measurements D1–D4, *Major plot:* Spectra after correction with the full transfer function, normalized to an equal integral. *Minor plot:* The same spectra, normalized to the mean signal amplitude per bunch.

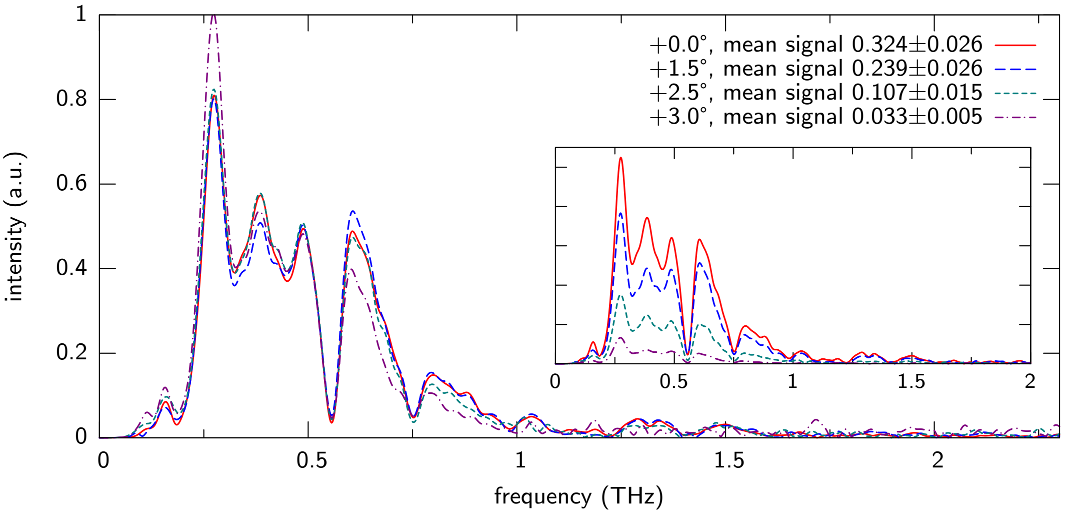

Figure 7.26: Measurements H1–H4, spectra. *Major plot:* Normalized to an equal integral. *Minor plot:* Normalized to the mean detector signal per bunch.

8 Conclusion

A high peak current of the electron bunches is a very important parameter for a high-gain free electron laser. To generate high local charge densities in the first place, a laser driven photo cathode is used, and a rapid acceleration to relativistic energies in an RF cavity helps to minimize the growth of the energy spread by space charge effects. Afterwards, the current is increased by a longitudinal compression of the bunches in two magnetic chicanes.

Monitoring the coherent radiation intensity emitted by the electron bunches with pyroelectric detectors has proven to be an excellent tool to determine a qualitative degree of compression. With this method, it has been possible to show that the RF phase of the first acceleration module of the VUV-FEL – the basic parameter controlling the compression of the beam – performs periodic drifts over a range of about 1.5°. It has also been observed that the SASE process is very sensitive to variations of this phase, and that hence a regulation of the degree of compression is necessary to sustain the generation of laser pulses. A feedback software has been developed that is able to stabilize the phase with sufficient accuracy.

While the integrated intensity of coherent radiation is only a qualitative measure for the compression achieved in the magnetic chicanes, an analysis of its spectrum allows to reconstruct the longitudinal charge profile of the electron bunches. It has been shown that a Martin-Puplett interferometer is well suited to determine the far-infrared spectrum of a strongly fluctuating radiation source because of its intensity-normalizing working principle. Detailed procedures for alignment of the instrument as well as for data recording, and for the complex evaluation and reconstruction process have been established.

Using coherent synchrotron radiation for the interferometry – which is generated in a bunch compressor anyway – has the advantage of facilitating parasitic measurements without disrupting the operation of the accelerator. However, it introduces the problem of a single-particle spectrum that is not well known, as it includes radiation contributions from more than one magnet, and edge effects from the finite extent of the dipole fields. The narrow vacuum chamber imposes a low-frequency cutoff at 275 GHz that prevents features of the bunch longer than about 2 ps to be reconstructed.

Within these constraints, the bunch shape after compression in the magnetic chicane BC2 has been determined. Within the measurement uncertainties, it is found to be independent of the phase setting of the preceding acceleration module ACC1. The longitudinal profile is strongly asymmetric with a steep rise at the head of the bunch. The full width at half maximum amounts to about 1 ps, and only minor structures with an extent below 400 fs are discernible.

As the measured spectra show no significant intensity above 2 THz, there is no evidence for the existence of a narrow spike comprising a material fraction of the bunch charge. However, some effects are not understood well, and the possibility that the high-frequency range is suppressed – e.g. by diffraction losses – cannot be excluded.

Outlook

At present, a number of unknown quantities enter into the process of bunch shape reconstruction. To improve the accuracy of the method, several points need further investigation:

- The diffraction losses along the beam transfer line should be measured to obtain a reliable transfer function. For this purpose, a far-infrared source with a known spectrum, possibly a blackbody radiator, is needed.

- The spectral responsivity of the detectors for far-infrared radiation needs to be determined.

- The computed incoherent spectrum at the vacuum port of the bunch compressor should be verified experimentally. While the low radiation intensity makes this virtually impossible with the current parameters of the accelerator, the planned operation with 1000 or more bunches per macropulse might facilitate an interferometric measurement.

The planned installation of a *third-harmonic cavity* will help to reduce the energy spread of the beam before it passes the magnetic chicane; it is expected that this will lead to a shortening of the compressed bunch, and hence more intensity at high frequencies should be measurable with the interferometer.

If some of the above points can be clarified and the results can be successfully cross-checked with other methods, the bunch length measurement by interferometry will be a reliable tool for accelerator diagnostics at the VUV-FEL and the XFEL. However, the length of reconstructable bunch features will always be limited upwards by the low-frequency cutoff of the beam surroundings, and downwards by the optical components.

A Appendices

A.1 Tables

Token	Relative phase (°)	Phase of max. compr. (°)	Phase at scan start (°)	Energy (MeV)	Charge (nC)	Bunches
D0	∼ 6	(SASE operation)		125	1.16 ± 0.04	10
D1	1.1	119.4	120.5	125	1.16 ± 0.07	1
D2	3.0	106.8	109.8	127	0.80 ± 0.05	2
D3	4.8	119.2	124.0	125	1.16 ± 0.07	1
D4	5.6	106.4	112.0	127	0.81 ± 0.04	5
H1	∼ 0.0	(stabilized to 80 mV)		127	0.96 ± 0.03	1
H2	∼ 1.5	(stabilized to 60 mV)		127	0.92 ± 0.05	1
H3	∼ 2.5	(stabilized to 40 mV)		127	0.96 ± 0.03	1
H4	∼ 3.0	(stabilized to 30 mV)		127	0.96 ± 0.03	2

Table A.1: Main accelerator parameters for the examined measurements. The Dn interferogram scans were recorded in dry nitrogen atmosphere, the Hn scans in humid air. The *phase of maximum compression* of ACC1 is found by a scan as described in section 7.1, and it is the point of reference for the *relative phase*. During *SASE operation*, the phase was adjusted manually to compensate for drifts, for *stabilized* measurements this was done automatically by a feedback loop monitoring the CTR signal from a transition radiator downstream of BC2.

Token	Roof mirror start pos. (mm)	Roof mirror end pos. (mm)	Points	Measurements per point	Max. freq. (THz)
D0	44.0	53.0	512	4	4.3
D1	41.0	56.0	512	5	2.6
D2	43.0	54.0	367	3	2.5
D3	41.0	56.0	511	5	2.6
D4	43.0	54.0	366	3	2.5
H1	40.5	56.5	512	3	2.4
H2	40.5	56.5	512	3	2.4
H3	40.5	56.5	512	3	2.4
H4	40.5	56.5	512	3	2.4

Table A.2: Scan parameters for the examined measurements. The specified maximum frequency is the highest frequency that can be obtained from a measurement with the given scan range and number of points.

Token	relative phase (°)	Low-freq. asymptote	Width (ps) FWHM	RMS	Remarks
D0	6.0	Taylor	0.98	0.50	
	6.0	Gaussian	1.11	0.63	
D0′	6.0	Taylor	0.82	0.32	linear interpolation,
	6.0	Gaussian	0.82	0.32	see Fig. 7.21
D1	1.2	Taylor	1.23	0.48	
D2	3.0	Taylor	0.92	0.55	
D3	4.8	Taylor	1.08	0.48	
D4	5.6	Taylor	1.17	0.55	

Table A.3: Bunch lengths for measurements D0–D4; the specified phase is relative to the point of maximum compression at the start of the scan.

A.2 Technical drawings

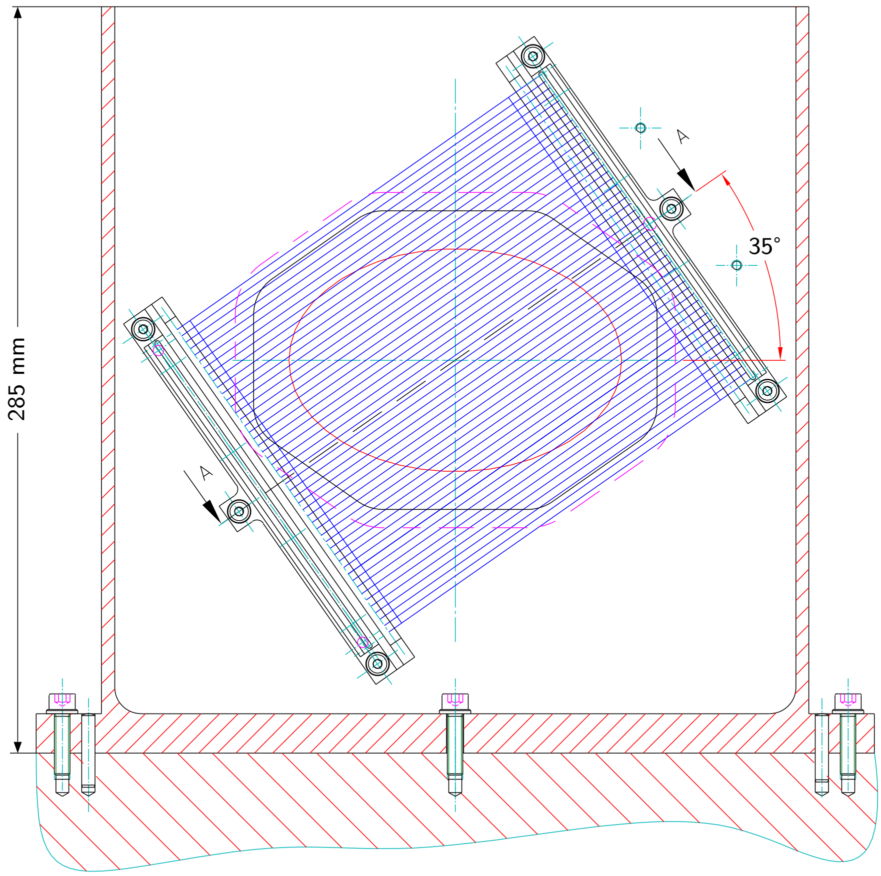

Figure A.1: Beam divider BDG of the Martin-Puplett interferometer, wires not to scale (drawing by R. Siedling)

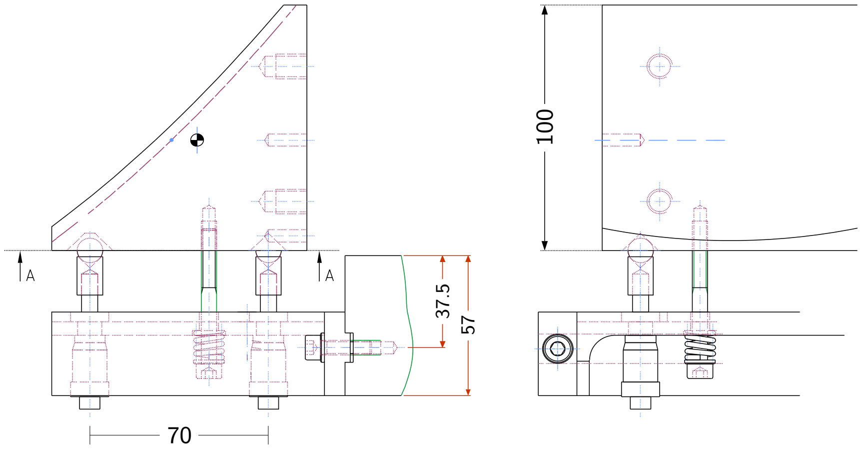

Figure A.2: Parabolic mirror PM2 of the Martin-Puplett interferometer, all measures in millimeters (drawing by R. Siedling, modified)

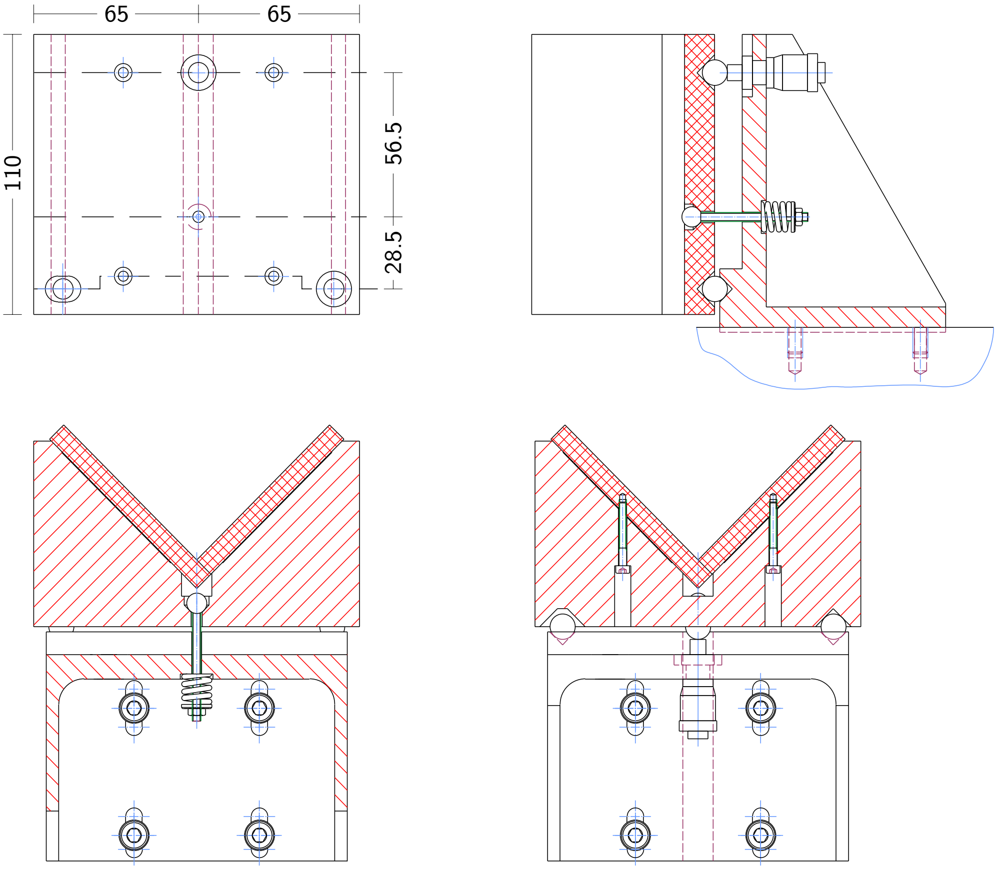

Figure A.3: Roof mirror FRM/MRM of the Martin-Puplett interferometer, all measures in millimeters. The fixed and the moveable roof mirror are identical in construction. (drawing by R. Siedling, modified)

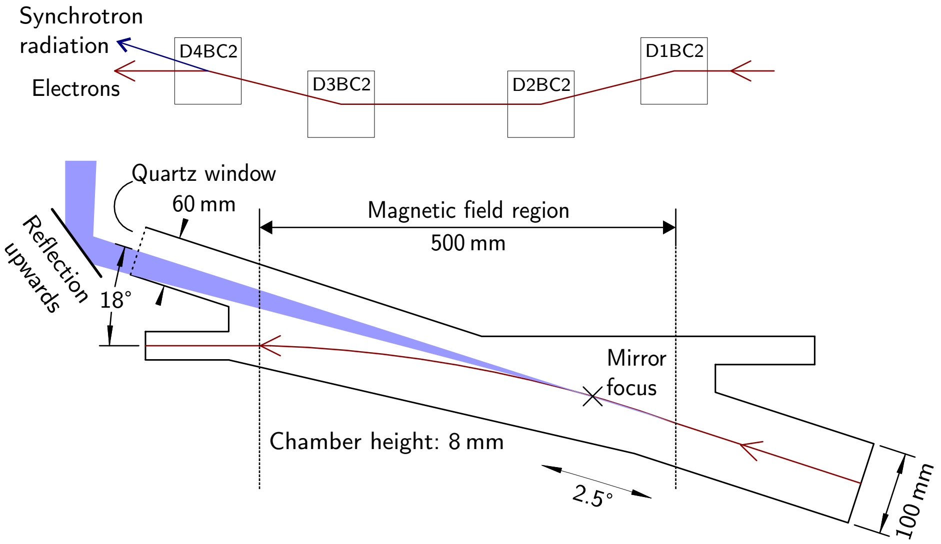

Figure A.4: Schematic of the BC2 vacuum chamber. The vacuum window covers about 2.5° of the bending arc. (drawing by O. Grimm, modified)

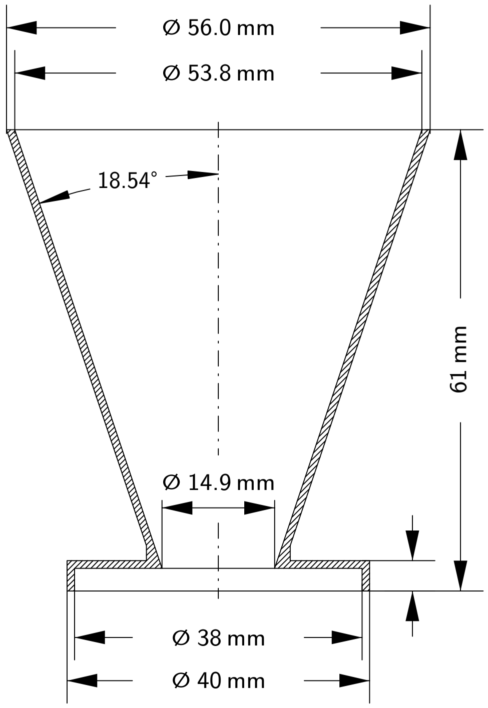

Figure A.5: DTGS detector cone

A.3 Abbreviations

ACC*n*	acceleration module *n* of the VUV-FEL
AG	analyzer wire grid of the Martin-Puplett interferometer
BC*n*	bunch compressor *n* of the VUV-FEL (counting starts with 2 for historical reasons)
BCM	bunch compression monitor
BDG	beam divider wire grid of the Martin-Puplett interferometer
CDR	coherent diffraction radiation
CSR	coherent synchrotron radiation
CTR	coherent transition radiation
DESY	Deutsches Elektronen-Synchrotron
DFT	discrete Fourier transform
DLaTGS	deuterated triglycine sulphate, doped with L-α-alanine
DTGS	deuterated triclycine sulphate (this includes DLaTGS)
EFL	effective focal length
FEL	free electron laser
FFT	fast Fourier transform
FIR	far-infrared
FRM	fixed roof mirror
FWHM	full width at half maximum
HDET	detector for horizontally polarized radiation in the Martin-Puplett interferometer
ILS	instrumental lineshape
IR	infrared
LINAC	linear accelerator
M*n*	flat mirror *n* of the radiation transfer line
MRM	moveable roof mirror
OTR	optical transition radiation
PG	polarizer wire grid of the Martin-Puplett interferometer
PM*n*	off-axis parabolic mirror *n* of the radiation transfer line
RF	radio frequency
RMS	root-mean-square
SASE	self-amplified spontaneous emission
SR	synchrotron radiation
TESLA	TeV Energy Superconducting Linear Accelerator
TOSYLAB	Terahertz and Optical Synchrotron Radiation Laboratory
TTF	TESLA Test Facility
UV	ultraviolet
VDET	detector for vertically polarized radiation in the Martin-Puplett interferometer
VUV	vacuum-ultraviolet
VUV-FEL	Vacuum-Ultraviolet Free Electron Laser
XFEL	(European) X-ray Free Electron Laser

References

[Alo96] M. Alonso and E. J. Finn. *Physics*. Addison Wesley Longman, 1996.

[And00] J. Andruszkow, B. Aune, V. Ayvazyan, et al. *First observation of self-amplified spontaneous emission in a free-electron laser at 109 nm wavelength*. *Phys. Rev. Lett.*, 85(18):3825–3829, October 2000.

[Bon84] R. Bonifacio, C. Pellegrini, and L. M. Narducci. *Collective instabilities and high-gain regime free electron laser*. *Opt. Commun.*, 50(6):373–378, July 1984.

[Bro96] I. N. Bronstein and K. A. Semendjajew. *Taschenbuch der Mathematik*. Teubner, 1996.

[Cha80] W. G. Chambers, C. L. Mok, and T. J. Parker. *Theory of the scattering of electromagnetic waves by a regular grid of parallel cylindrical wires with circular cross section*. *J. Phys. A: Math. Gen.*, 13(4):1433–1441, April 1980.

[Edw95] D. A. Edwards (editor). *TESLA Test Facility linac design report*. March 1995. DESY report TESLA-FEL 95-03.

[Eli76] L. R. Elias, W. M. Fairbank, J. M. J. Madey, et al. *Observation of stimulated emission of radiation by relativistic electrons in a spatially periodic transverse magnetic field*. *Phys. Rev. Lett.*, 36(13):717–720, March 1976.

[Gei99a] M. Geitz. *Investigation of the transverse and longitudinal beam parameters at the TESLA Test Facility linac*. Ph.D. thesis, University of Hamburg, November 1999. DESY report DESY-THESIS-1999-033.

[Gei99] M. Geitz, B. Leißner, C. Berger, et al. *Bunch length measurements using a Martin Puplett interferometer at the Tesla Test Facility linac*. In: *Proceedings of the 1999 Particle Accelerator Conference*. New York, 1999.

[Gel03] G. Geloni, E. L. Saldin, E. A. Schneidmiller, et al. *A method for ultrashort electron pulse-shape measurement using coherent synchrotron radiation*. *DESY report*, 03-031:ISSN 0418-9833, March 2003.

[Gri05a] O. Grimm. *Relative humidity in the TOSYLAB beam transfer line*. Personal communication.

[Gri05] O. Grimm. *Simulated single-particle synchrotron radiation spectrum for the bunch compressor BC2*. Personal communication.

[Gro84] J. Gronholz and W. Herres. *Understanding FT-IR data processing*. *I & C Reprint*, 1(84), 3(85), 1984–1985. Dr. Alfred Huethig Publishers (reprint available from Bruker Analytische Messtechnik GmbH, Karlsruhe, Germany).

[Han97] K. Hanke. *Measurement of picosecond electron bunches in a linear accelerator*. Ph.D. thesis, University of Hamburg, November 1997. DESY report TESLA 97-19.

[Hof98] A. Hofmann. *Characteristics of synchrotron radiation*. In: S. Turner (editor), *CAS - CERN Accelerator School: Synchrotron radiation and free electron lasers*, volume CERN 98-04. Grenoble, France, April 1998.

[Hon04] K. Honkavaara. *Commissioning of the TTF linac injector at the DESY VUV-FEL*. Presentation given at the FEL Conference 2004, Trieste, Italy, August 2004.

[Jac98] J. D. Jackson. *Classical electrodynamics*. John Wiley & Sons, Inc., third edition, 1998.

[Jep04] P. U. Jepsen. *Measured absorption coefficients of humid air for wavelengths from 100 μm to 3 mm*, 2004. University of Freiburg, personal communication.

[Kit96] C. Kittel. *Introduction to solid state physics*. Wiley, 7th edition, 1996.

[Kon81] A. M. Kondratenko and E. L. Saldin. *Generation of coherent radiation by a beam of relativistic electrons in an undulator*. *Zhurnal Tekhnicheskoi Fiziki*, 51:1633–1642, August 1981.

[Kra97] G. A. Krafft. *Diagnostics for ultrashort bunches*. In: *Proceedings of the 3rd European Workshop on Diagnostics and Beam Instrumentation*, pp. 48–52. Frascati, Italy, 1997.

[Lai94] R. Lai and A. J. Sievers. *Examination of the phase problem associated with the determination of the longitudinal shape of a charged particle bunch from its coherent far IR spectrum*. *Phys. Rev. E*, 50:3342, 1994.

[Lai96] R. Lai and A. J. Sievers. *Micro bunches workshop*, volume 376, p. 312. AIP press, Woodbury, 1996.

[Lai97] R. Lai and A. J. Sievers. *On using the coherent far IR radiation produced by a charged-particle bunch to determine its shape: I Analysis*. *Nucl. Instr. and Meth.*, A 397:221–231, April 1997.

[Lam78] D. K. Lambert and P. L. Richards. *Martin-Puplett interferometer: an analysis*. *Appl. Opt.*, 17(10):1595–1602, May 1978.

[Lei98] B. Leißner. *Strahluntersuchungen am TESLA Linearbeschleuniger*. Diploma thesis, Rheinisch-Westfälische Technische Hochschule Aachen, Germany, November 1998.

[Les90] J. C. G. Lesurf. *Millimetre-wave optics, devices and systems*. Adam Hilger, January 1990.

[Loe73] E. V. Loewenstein, D. R. Smith, and R. L. Morgan. *Optical constants of far infrared materials, 2: Crystalline solids*. *Appl. Opt.*, 12(2):398–406, February 1973.

[Lud03] F. Ludwig. *Nonlinear dynamics and far-infrared broadband spectroscopy of* $YBa_2Cu_3O_7$ *Josephson junctions for the TESLA Test Facility linac*. Ph.D. thesis, University of Hamburg, August 2003. DESY report DESY-THESIS-2003-024.

[Mad71] J. M. J. Madey. *Stimulated emission of bremsstrahlung in a periodic magnetic field*. *J. Appl. Phys.*, 42(5):1906–1913, April 1971.

[Men05] J. Menzel. *THz-Spektroskopie zur Bunchlängenmessung an der TESLA-Testanlage TTF*. Ph.D. thesis, Universität Hamburg, 2005.

[Mil00] S. V. Milton, E. Gluskin, S. G. Biedron, et al. *Observation of self-amplified spontaneous emission and exponential growth at 530 nm*. *Phys. Rev. Lett.*, 85(5):988–991, July 2000.

[Nev36] R. Nevanlinna. *Eindeutige analytische Funktionen*. Verlag Julius Springer, Berlin, 1936.

[Ori04] Oriel Instruments. *Introduction to FT-IR spectroscopy*. Oriel Instruments, 150 Long Beach Blvd., Stratford, CT 06615, USA, 2004.

[Pal97] E. D. Palik (editor). *Handbook of optical constants of solids*. Academic Press, January 1997.

[Pic98] H. M. Pickett, R. L. Poynter, E. A. Cohen, et al. *Submillimeter, millimeter, and microwave spectral line catalog*. *J. Quant. Spectrosc. & Rad. Transfer*, 60:883–890, 1998. Online catalog available at NASA Jet Propulsion Laboratory, http://spec.jpl.nasa.gov/.

[Ric00] K. N. Ricci. *Longitudinal electron bunch measurements at the Stanford superconducting accelerator*. Ph.D. thesis, Stanford university, May 2000.

[Sho43] J. A. Shohat and J. D. Tamarkin. *Problem of moments*. *Mathematical Surveys*, 1:23, 1943. American Mathematical Society, New York.

[Spa79] M. Sparks and E. Loh. *Temperature dependence of absorptance in laser damage of metallic mirrors, parts I and II*. *J. Opt. Soc. Am.*, 69:847–868, 1979.

[Ste04a] B. Steffen, S. Casalbuoni, P. Schmüser, et al. *Bunch length measurements at the SLS linac using electro optical sampling*. In: *Proceedings of the 2004 FEL Conference*, pp. 392–394. 2004.

[Ste04] F. Stephan. *Recent results and perspectives of the low emittance photo injector at PITZ*. Presentation given at the FEL Conference 2004, Trieste, Italy, August 2004.

[Stu04] F. Stulle. *A bunch compressor for small emittances and high peak currents at the VUV Free-Electron Laser*. Ph.D. thesis, University of Hamburg, October 2004. DESY report DESY-THESIS-2004-041.

[TTF02] The TESLA Test Facility FEL team. *SASE FEL at the TESLA facility, phase 2*. June 2002. DESY report TESLA-FEL 2002-01.

[Tol56] J. S. Toll. *Causality and the dispersion relation: Logical foundations*. *Phys. Rev.*, 104(6):1760–1770, December 1956.

[Wei04] H. Weise. *The TESLA XFEL project*. In: *Proceedings of EPAC 2004, Lucerne, Switzerland*, pp. 11–15. 2004.

[Wie03] H. Wiedemann. *Particle Accelerator Physics II, Nonlinear and higher-order beam dynamics*. Springer, second edition, 2003.

[Woo72] F. Wooten. *Optical properties of solids*. Academic Press, New York, 1972.

Acknowledgements

> Es ist ein lobenswerter Brauch:
> Wer Gutes bekommt, der bedankt sich auch.
>
> *(Wilhelm Busch)*

First of all, I would like to thank Prof. Dr. Jörg Roßbach and Prof. Dr. Peter Schmüser for introducing me to the field of accelerator physics and giving me the opportunity to prepare my thesis at DESY. I also appreciate the helpful criticism and support they provided me with.

I am grateful to Dr. Oliver Grimm, who was always there to help me with my experimental and theoretical work while leaving me the free space to pursue my own ideas.

Special thanks go to Dr. Jan Menzel for sharing his experience with terahertz spectroscopy, and for finding the time for fruitful discussions although he was occupied with his own Ph. D. thesis.

I have to apologize to Hossein Delsim-Hashemi, who spent a lot of time working on optics simulations of the transfer line and of the interferometer. In the end, the results he provided me with have not been included in this thesis at all. Also Dr. Sara Casalbuoni deserves thanks for optics simulations, and no less for enduring the crazy night-shifts in which we made the first measurements.

Otto Peters and Matthias Böttcher not only lent a helping hand when there was something to build, but were always a source of good advice. Thank you.

Furthermore, I am indebted to Dr. Nicoleta Baboi, Bolko Beutner, Andy Bolzmann and Florian Löhl for letting me keep them from work with endless but productive discussions on various physical and non-physical topics. Special thanks also go to Kaj Merten Berggreen for proofreading this thesis from the point of view of someone who is not from the field.

Finally, I thank all the operators of the VUV-FEL for the chance to learn from them and for their patience when I interrupted their schedule with my measurements. Although it is sometimes tiresome, to work with you is always enjoyable.